JOURNAL OF PETROLOGY | VOLUME 55 | NUMBER 10 | PAGES 1965–2002 | 2014 | doi:10.1093/petrology/egu047

# Accessory Mineral Behaviour in Granulite Migmatites: a Case Study from the Kerala Khondalite Belt, India

**SIMON L. HARLEY[1]* AND V. NANDAKUMAR[2]**

[1]SCHOOL OF GEOSCIENCES, UNIVERSITY OF EDINBURGH, KING'S BUILDINGS, WEST MAINS ROAD, EDINBURGH EH9 3JW, UK

[2]CENTRE FOR EARTH SCIENCE STUDIES, TRIVANDRUM, KERALA, INDIA

**RECEIVED AUGUST 31, 2013; ACCEPTED AUGUST 13, 2014**

*Zircon, monazite, garnet and feldspar trace element microanalysis, zircon and monazite U–Pb isotopic ages and monazite Th–U–Pb chemical dating, determined* in situ *from a leucogranitic vein in migmatitic gneiss at Kulappara in the Kerala Khondalite Belt (Trivandrum Block), India, demonstrate accessory mineral crystallization from an evolving melt-bearing system from* c. *545 to 535 Ma at temperatures of greater than 780°C. Marked changes in zircon chemistry to lower Th/U and $Yb_n/Gd_n$ occurred during its growth in the evolving melt, correlated with a dramatic change in microtexture from initial 'hopper'-like feathered-core and outer planar sector domains to darker planar zones and elliptical to lobate infilling and replacement zircon. Initially high Th/U, high heavy rare earth element (HREE) zircon crystallized rapidly from melt from 544 ± 9 Ma under open-system conditions in which the host-rock mineralogy had no chemical impact. This zircon precipitated prior to crystallization of significant garnet, trapping melt as inclusions that later crystallized to cryptogranite within zircon cores. Further zircon crystallization ensued under localized closed-system conditions leading to the establishment of zircon–garnet REE equilibrium at least on local (i.e. millimetre to centimetre) scales, consistent with melt entrapment, at 542 ± 6 Ma. Monazite crystallized in this fractionated melt by 535 ± 6 Ma. These results demonstrate that zircon can be a sensitive indicator of changing conditions and scales of melt transfer and interaction in high-temperature migmatites, recording in this instance a transition from melt-dominated open-system behaviour to closed-system crystallization and mineral–melt interaction at* T > *780°C in the deep crust of a hot orogenic belt.*

KEY WORDS: *zircon; U–Pb dating; U–Th–Pb; trace element; metamorphism; gneiss; garnet; granulite; monazite; migmatite*

## INTRODUCTION

The detailed processes involved in high-temperature (HT) metamorphism, in particular those involving melt production, retention and loss, are in many cases only weakly constrained by the isotopic information obtained from granulite-facies migmatites (Brown, 2004). The question of how migmatitic granulites reflect the conditions and dynamics of melt generation, migration, entrapment and crystallization remains a key issue for both the calculation of phase diagrams for HT metamorphic rocks (e.g. White & Powell, 2002; Kelsey & Powell, 2011) and the rheological behaviour of hot orogenic belts (Beaumont *et al.*, 2001, 2006; Jamieson *et al.*, 2004; Clark *et al.*, 2011).

Models of HT metamorphism in orogenic belts either implicitly or explicitly require that the middle to deep crust remains at $T > 700°C$ and even >800°C for timescales of the order of 5 to >80 Myr, depending on the tectonic scenario adopted and modelled (Jamieson *et al.*, 2010; Jamieson & Beaumont, 2011). Common to these models, and required by metamorphic phase equilibrium, is the production, presence and potential migration of melt in rocks with varying degrees of fertility (Sawyer, 1994, 1999, 2001; Brown, 2004; Vanderhaeghe, 2009). The limited availability of water means that most melting is

*Corresponding author. E-mail: simon.harley@ed.ac.uk

likely to occur through multivariant 'dehydration-melting' reactions involving the breakdown of hydrous minerals in the absence of excess volatiles (Thompson, 1982; Clemens & Vielzeuf, 1987; Waters, 1988; Stevens & Clemens, 1993; White *et al.*, 2001). Additional melting may be promoted by hybridization; for example, by interaction between somewhat fertile rocks and invasive melts sourced from elsewhere in the deep crust. In the simplest situation a pelite or semipelite undergoing HT metamorphism on a clockwise $P$–$T$ path would undergo biotite-controlled partial melting at high $P$ and then be in the melt-present $P$–$T$ field for millions to tens of millions of years. Crystallization of the melt, if it remains with its source rock, will occur either on encountering a cordierite-bearing field or on intersecting an appropriate $H_2O$ wt % isopleth. In reality, melts produced early in such a $P$–$T$ history have the potential to migrate, pool or pond, coalesce and interact with other lithologies (e.g. less fertile ones)—leading to complex chronologies of melt formation, injection and crystallization throughout the $P$–$T$ path, as documented in detailed studies of migmatite terranes (Fitzsimons, 1996; Kriegsmann, 2001; Sawyer, 2001; Cenki *et al.*, 2002; White & Powell, 2002). In these dynamic cases the crystallization of melts may be delayed to occur on the low-$P$ cooling segment of the $P$–$T$ history, but different melt batches may conceivably undergo crystallization at various points on the $P$–$T$ path, leading to cross-cutting and multi-generation leucosomes.

In this study we present new zircon and monazite microtexture, age and trace element data, integrated with whole-rock and major phase trace element chemistry, that constrain the behaviour of zircon (and monazite) during melt crystallization and entrapment as a local anatectic system evolved from being melt-dominated to host- or wall-rock-controlled at 545–535 Ma. We provide detailed textural and mineral REE evidence that zircons within a discordant leucogranitic vein initially grew as hollow grains during open-system melt crystallization, and were later infilled and overgrown during continued crystallization consequent on leucosome entrapment, monazite crystallization and wall-rock interaction. Finally, we show that these accessory minerals underwent later *in situ* recrystallization accompanied by equilibration with host-rock minerals, in particular garnet, some 20–30 Myr after their precipitation from anatectic melts.

## GEOLOGICAL CONTEXT: THE KERALA KHONDALITE BELT

The Kerala Khondalite Belt (KKB, Fig. 1), also referred to as the Trivandrum Block (e.g. Santosh, 1996; Collins *et al.*, 2014), is an elongate, NW–SE-trending basement complex that forms part of the Southern Granulite Terrane of India. The Southern Granulite Terrane of India refers to an amalgam of several basement blocks typified by regionally metamorphosed granulite-facies rocks, many of which have been produced during late Neoproterozoic to Cambrian orogenesis associated with the amalgamation of continental fragments to form Gondwana (e.g. Braun *et al.*, 1998; Braun & Kriegsman, 2003; Santosh *et al.*, 2003, 2005a, 2006*a*, 2006*b*, 2009; Cenki & Kriegsman, 2005; Collins *et al.*, 2007, 2014).

The Trivandrum Block is bounded to its NE and separated from the Southern Madurai Block by the Achankovil Shear Zone (AKSZ), and bounded to the SW by the Nagercoil Block. The Southern Madurai Block (SMB) is composed of dominantly metasedimentary gneisses with Meso- to Neoproterozoic detrital zircon ages and zircon Hf initial ratios (Collins *et al.*, 2007, 2014; Plasva *et al.*, 2012, in preparation), and has recently been interpreted as including a late Neoproterozoic sedimentary basin progressively filled by more juvenile sources towards its southwestern margin (Tomson *et al.*, 2006; Plasva *et al.*, 2012; Collins *et al.*, 2014). Although 900–700 Ma magmatic and metamorphic mineral ages have been reported from the SMB (e.g. Braun & Appel, 2006; Teale *et al.*, 2011; Plasva *et al.*, 2012), its 7–11 kbar granulite-facies HT–UHT metamorphism is generally considered to have occurred from *c.* 550 to 515 Ma (Collins *et al.*, 2007, 2014).

Immediately to the NE of the Trivandrum Block, the Achankovil Shear Zone (also known as the Achankovil Zone) is a belt composed of Neoproterozoic metasediments (Collins *et al.*, 2007), 550 ± 25 Ma alkali granites (Santosh *et al.*, 2005*b*) and 550–525 Ma charnockites (Ghosh *et al.*, 2004; Sato *et al.*, 2011). The AKSZ metasediments preserve Mesoproterozoic Sm–Nd model ages (1·4–1·3 Ga: Bartlett *et al.*, 1998; Cenki *et al.*, 2004) that distinguish them from the metasediments in the Trivandrum Block, which generally have Archaean to Palaeoproterozoic model ages (Cenki *et al.*, 2004; Shabeer *et al.*, 2005). Detrital zircon age spectra for AKSZ metasediments (2·2–0·65 Ga) are similar to those obtained from parts of the SMB, consistent with the ACSZ being part of a SW-younging SMB (Tomson *et al.*, 2006; Plavsa *et al.*, 2012; Collins *et al.*, 2014). Whereas Santosh *et al.* (2009) have interpreted the ACSZ as representing a terrane suture between the SMB and the Trivandrum Block, Collins *et al.* (2014) argued that the available age data allow the possibility of it being a juvenile Neoproterozoic rift-related basin formed on an already stabilized continent that included the Southern Madurai, Trivandrum and Nagercoil Blocks as well as formerly adjacent parts of southern Africa, Madagascar, Antarctica and Sri Lanka. Zircon and monazite age data have been interpreted to indicate that the ACSZ experienced its principal high-grade tectonism, including UHT metamorphism, at 515 ± 16 Ma based on the data of Santosh *et al.* (2003, 2005*b*), Shabeer *et al.* (2005) and Collins *et al.* (2007, 2014).

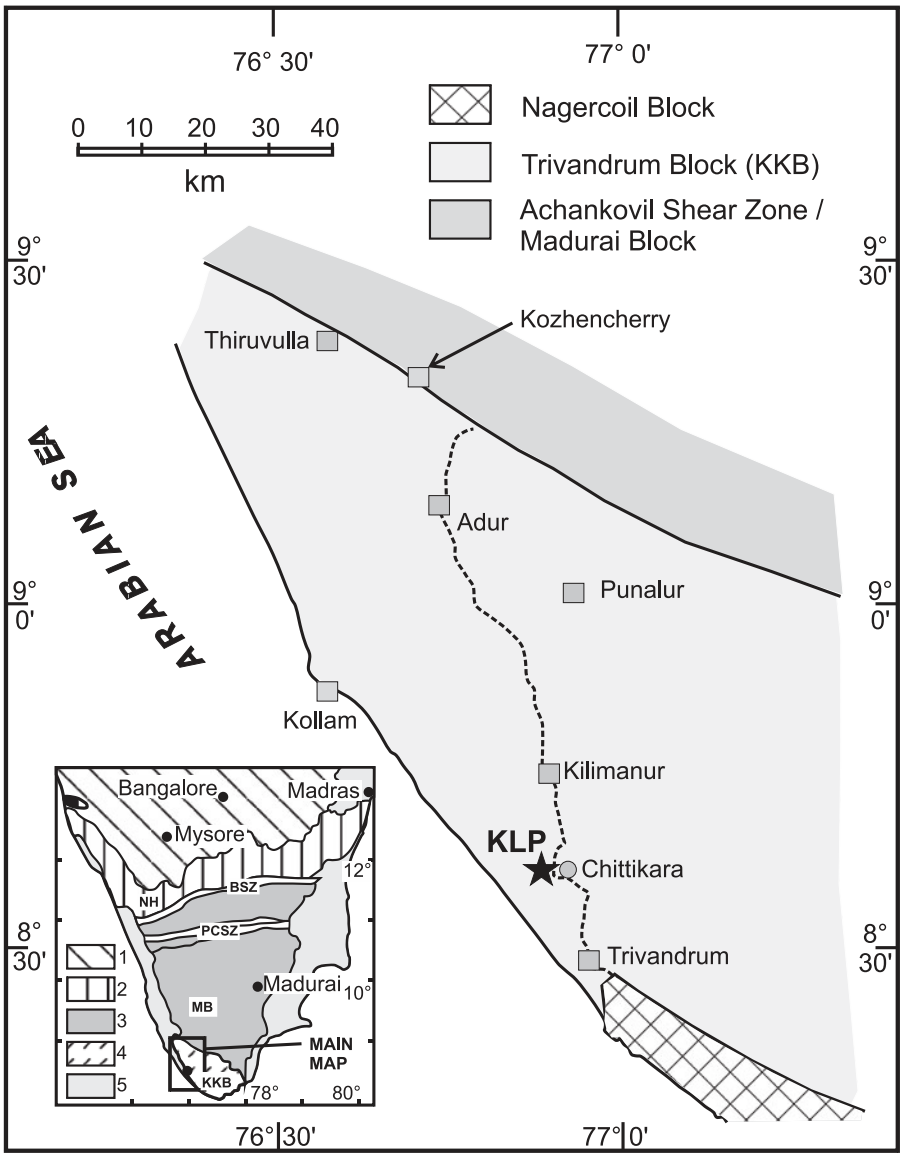


**Fig. 1.** Simplified geological map of the Kerala Khondalite Belt (KKB), southern India, showing locations of sites referred to in this paper, including the Kulappara site (KLP) that is the focus of the detailed study. Inset shows the location of the KKB in relation to other domains of south India. Abbreviations in inset map: BSZ, Bhavani Shear Zone; NH, Nilgiri Hills; PCSZ, Palghat–Cauvery Shear Zone. Key to shaded areas: 1, Archaean Dharwar Craton north of orthopyroxene-in isograd; 2, Archaean charnockite massifs; 3, Madurai Block and other dominantly Proterozoic crust; 4, Kerala Khondalite Belt; 5, recent sediments.

The Nagercoil Block, located to the SW of the Trivandrum Block, preserves massif-type charnockites with emplacement ages of 2 Ga and model ages ranging from Archaean to Palaeoproterozoic, similar to the protoliths of charnockites from within the Trivandrum Block itself (Cenki *et al.*, 2004; Ghosh *et al.*, 2004; Kröner *et al.*, 2012; Tomson *et al.*, 2013). Whereas Santosh *et al.* (2009) have suggested that the Nagercoil charnockites were intruded as high-*T*, dry magmas, Rajesh *et al.* (2011) have reinterpreted them as granitic rocks transformed into garnet–orthopyroxene charnockites during Neoproterozoic–Cambrian granulite metamorphism, possibly at *c.* 515 Ma (Collins *et al.*, 2007). The protolith, model age and metamorphic age record of the Nagercoil Block suggests that it is essentially contiguous with the Trivandrum Block.

The Trivandrum Block (KKB) itself is composed dominantly of granulite-facies supracrustal rocks including migmatitic garnet–biotite–quartz–feldspar gneisses and garnet–cordierite–sillimanite gneisses (khondalites), as well as charnockites and localized mafic granulites. The metasediments preserve Archaean to Palaeoproterozoic model ages

and Neoarchaean to Palaeoproterozoic detrital zircon ages (Cenki *et al.*, 2004; Collins *et al.*, 2007) implying deposition of their sedimentary precursors after *c.* 1·9 Ga. Kröner *et al.* (2012) have identified 1·8 Ga intrusive rocks, now preserved as charnockite, implying deposition of at least some of the KKB metasediment precursors by that time.

The final granulite-facies metamorphism and migmatization in the Trivandrum Block is latest Neoproterozoic to Cambrian in age. Zircon ages obtained from migmatites and leucogranites are generally in the range 550–530 Ma (Shabeer *et al.*, 2005), similar to monazite chemical ages that are considered to date the HT–UHT metamorphism (Santosh *et al.*, 2003, 2005a, 2006a, 2006b). Local charnockitization promoted by $CO_2$ infiltration occurred at *c.* 520 Ma (Santosh *et al.*, 2006a), and Rb–Sr mica (Choudhary *et al.*, 1992; Cenki *et al.*, 2004) cooling ages indicate cooling to $T < 500^{\circ}C$ by 510 Ma. This tectonothermal evolution may be more complicated, however, as Braun and co-workers (Braun *et al.*, 1998; Braun & Bröcker, 2004; Cenki *et al.*, 2004; Braun, 2006) have presented evidence for metamorphic zircon ages ranging from 570 to 520 Ma, and from this concluded that HT metamorphism lasted for 50 Myr. In contrast, Collins *et al.* (2007) have shown that a significant proportion of metamorphic U–Pb zircon ages in both the Trivandrum Block and adjacent AKSZ are in the range 513 ± 6 Ma, and interpreted this as the age of the main granulite metamorphism shared by each block.

The $P$–$T$ conditions of the Neoproterozoic–Cambrian HT–UHT metamorphism and migmatization in the KKB or Trivandrum Block have been estimated as 6–8 kbar and 880–930°C (Nandakumar & Harley, 2000; Braun & Bröcker, 2004), with 'clockwise' $P$–$T$ paths that traverse to lower $P$ with post-peak cooling to 700°C at 4–5 kbar. Based on the occurrence of spinel + quartz and other mineral assemblages Morimoto *et al.* (2004) and Tadokoro *et al.* (2008) inferred UHT temperatures of >950°C and pressures of up to 12 kbar for the KKB.

Consistent with these HT–UHT metamorphic conditions, the KKB or Trivandrum Block gneisses exhibit extensive migmatization. Leucosomes occur as decimetre to several metre wide sheets, as lenses, and as local pools and patches of decimetre to millimetre scale. Larger leucosome sheets are sub-concordant with gneissic fabrics on length scales of metres to tens of metres, as seen in quarries, but in detail show local discordances and rafting of gneissic material. In many quarries, including that reported here (Kulappara, KLP), the minimum proportion of leucosome is >30% by volume. Cesare *et al.* (2009) have reported the preservation of nanogranite and crytpogranite inclusions in garnets within the migmatitic pelites, directly demonstrating the presence of melt at peak and near-peak $P$–$T$ conditions in the KKB or Trivandrum Block.

In this study we examine the age and event information obtainable from an *in situ* microanalytical study of one sample of a discordant leucogranitic sheet traversing migmatitic pelitic gneisses from a single locality, Kulappara, situated in the centre of the Trivandrum Block. From this integrated study we deduce a history of melt presence and accessory phase crystallization at >780°C, from *c.* 545 to 535 Ma, in the central Trivandrum Block, and consider its implications for melt transfer, retention and host-rock interaction in the light of trace element evidence for mineral–melt interactions.

## METHODS

Major and selected trace elements were determined by X-ray fluorescence (XRF) at the Centre for Earth Science Studies (CESS), Trivandrum, using a Bruker S4 Pioneer sequential wavelength-dispersive X-ray spectrometer. Trace element and rare earth element (REE) whole-rock analyses were determined at the National Geophysical Research Institute (NGRI), Hyderabad, India, using a Perkin Elmer inductively coupled plasma mass spectrometry (ICP-MS) system–Elan DRC II instrument and three granite standards for quality control (USGS standards G-1 and G-2; Japanese standard granite JG-2).

### EMPA monazite trace element and Th–U–Pb chemical dating

Electron microprobe (EMPA) REE, Ca, Si, P and Th–U–Pb analysis of monazites was carried out using a five-spectrometer Cameca SX-100 electron microprobe at the University of Edinburgh, employing the REE, Th, U and Pb analytical procedures of D. A. Steele (Kelsey *et al.*, 2003; Berry *et al.*, 2008). An age of 506 ± 5·8 Ma (2σ standard error of the mean, MSWD = 0·35; 50 analyses) was obtained for the Moacyr monazite standard over the analytical session, in agreement with the accepted $^{207}Pb/^{235}U$ isotope dilution thermal ionization mass spectrometry (ID-TIMS) age of 504·3 ± 0·2 Ma obtained by Gasquet *et al.* (2010) from fragments of the same Moacyr monazite grain, as provided to S.L.H. by J.-M. Montel. Full details of the EMPA analysis procedures, and secondary ion mass spectrometry (SIMS) procedures summarized below, are provided in Supplementary Data Electronic Appendix 1 (supplementary data are available for downloading at http://www.petrology.oxfordjournals.org).

### SIMS trace element microanalysis protocol

REE and other selected trace elements within zircons, and also garnets, were determined using the EMMAC CAMECA ims-4f ion microprobe at the University of Edinburgh. Analytical conditions and correction procedures follow those of Harley & Kelly (2007), modified from Hinton & Upton (1991). Trace element abundances were calculated relative to Si (determined by electron microprobe analysis) and calibrated against the NIST-610 glass standard, with ion yields corrected by reference to the

zircon standard SL1. Corrections for isobaric interferences on heavy REE (HREE) arising from light REE (LREE) oxide species were carried out using in-house software developed by R. W. Hinton.

### SIMS U–Pb microanalysis procedures

U–Pb dating of zircons and monazites was carried out *in situ* in thin section at the Edinburgh Ion Microprobe Facility (EIMF), using the CAMECA ims-1270 ion microprobe. The thin section and inserted standards were imaged in detail using transmitted and reflected light microscopes, and the XL30 scanning electron microscope (SEM). Zircon cathodoluminesence (CL) images were collected at 15 kV and monazite backscattered electron (BSE) images at 20 kV.

Analytical procedures for zircon were similar to those described by Schuhmacher *et al.* (1994) and Whitehouse *et al.* (1997), analogous to those used by Kelly *et al.* (2008). Correction for *in situ* common Pb was made using the measured $^{204}$Pb counts above background at mass 204, and applying the present-day common Pb composition. Correction of Pb/U ratios for instrument drift with time was made using the relationship between ln(Pb/U) and ln($UO_2$/UO) (e.g. Schuhmacher *et al.*, 1994; Whitehouse *et al.*, 1997; Kelly *et al.*, 2008).

Elemental concentrations and Th/U ratios in unknown zircons were calculated by reference to measurements of Th/U and $^{208}$Pb/$^{206}$Pb on the Geostandards 91500 zircon (Wiedenbeck *et al.*, 1995: $^{206}$Pb/$^{238}$U age of 1062·4 ± 10·3 Ma; assumed $^{206}$Pb/$^{238}$U ratio = 0·17917; U = 81·2 ppm). Zircon U/Pb ratios were calibrated against measurements of the Plesovice zircon standard [Sláma *et al.*, 2008: $^{206}$Pb/$^{238}$U age 337·1 ± 6·0 Ma (1σ); assumed $^{206}$Pb/$^{238}$U ratio = 0·05369]. Fourteen analyses of the Plesovice standard in this study yielded an average $^{206}$Pb/$^{238}$U ratio of 0·5369 ± 0·0003 corresponding to a $^{206}$Pb/$^{238}$U age of 337·1 ± 1·8 Ma (2σ; MSWD = 0·45).

Monazite U–Th–Pb SIMS analysis followed similar procedures to that of zircon, with the exceptions that Th and $ThO_2$ were analysed in the monazites whereas HfO and $Zr_2O_2$ were determined in zircons. Common lead corrections were based on counts at mass 204 corrected for interferences and assuming modern lead. Correction of Pb/U ratios for instrument drift with time during monazite analysis was made using the relationship between ln(Pb/$UO_2$) and ln(UO/$UO_2$). The effect of U–Th fractionation in melting (Schärer, 1984) and consequent production of excess $^{206}$Pb from the decay of $^{230}$Th incorporated into high-Th monazite is accounted for explicitly in this study using a fractionation factor $f$ [(Th/U)monazite/(Th/U)melt] of 30 applied to the monazite standard and unknowns. This results in a 0·6% correction to the $^{207}$Pb/$^{206}$Pb ratios, which is propagated into the final $^{206}$Pb/$^{238}$U ratios used in age calculations. Analyses were referenced against the Moacyr standard (Itambe region, Brazil; provided directly by J.-M. Montel), for which four analyses bracketing the unknowns gave an average corrected $^{206}$Pb/$^{238}$U ratio of 0·0815 ± 0·0018 corresponding to a $^{206}$Pb/$^{238}$U age of 505 ± 5 Ma (2σ; MSWD = 1·6), consistent with the ID-TIMS $^{207}$Pb/$^{235}$U age of 504·3 ± 0·2 Ma reported by Gasquet *et al.* (2010) for the same standard material. The average $^{208}$Pb/$^{232}$Th ratio for the same analyses was 0·638 ± 0·016, corresponding to a $^{208}$Pb/$^{232}$Th age of 505 ± 11 Ma (2σ; MSWD = 0·17).

Both zircon and monazite data were reduced online using in-house data reduction spreadsheets developed by R. W. Hinton, and subsequently processed for age statistics and fits using ISOPLOT/EX v3 (Ludwig, 2003). Uncertainties on ages quoted in the text and in tables for single analyses (ratios and ages) are at the 1σ level. All uncertainties in calculated group ages are reported at 95% confidence limits. Inverse (Tera–Wasserburg) concordia diagrams were calculated with $^{206}$Pb/$^{238}$U and $^{207}$Pb/$^{235}$U ratios corrected for the minor common Pb present as calculated from measured $^{204}$Pb. Calculations of grouped U–Pb age data for specific zircon and monazite textural types were made using $^{206}$Pb/$^{238}$U ratios.

## MINERALOGY AND PETROGRAPHY OF KULAPPARA GNEISSES

The dominant rock types in the central Trivandrum Block are quartzofeldspathic garnet–biotite gneisses, garnet–cordierite–sillimanite–ilmenite-bearing migmatitic pelites with or without spinel, and minor orthopyroxene-bearing garnet–cordierite–ilmenite–(magnetite)–spinel aluminous magnesian gneiss. At Kulappara quarry (Fig. 1) the typical garnet-bearing migmatitic pelite is exposed. A strong near-vertical fabric is defined by gneissic layering comprising Grt + Sil + Crd + Ilm mesosomes (Fig. 2a; sample KLP2) and concordant to sub-concordant leucosome veins and lenses (sample KLP1), as well as 5–20 cm wide garnet-bearing leucogranite sheets (Fig. 2b). Leucogranite also occurs as rare thin (2–5 cm width) discordant dykes or veins that cut the principal layering over lateral distances of at least 3 m (Fig. 2a; sample KLP3) and are therefore younger in relative age than the local layered migmatite (Fig. 2c).

The migmatitic pelites at Kulappara contain varying proportions of Grt + Crd + Sill + Bt + Kfs + Qtz + Pl + Fe–Ti oxides ± green spinel (rare, and generally associated with ilmenite and sillimanite) with accessory zircon, monazite and apatite. They are characterized by alternating garnet–sillimanite–cordierite (+ Fe–Ti oxide) and quartzofeldspathic layers (e.g. KLP1) 2–5 mm in width. Garnet occurs in both layer types, and as coarse (5–30 mm diameter) porphyroblasts and cumuloblastic aggregates enclosing or associated with quartz–plagioclase–perthite grains

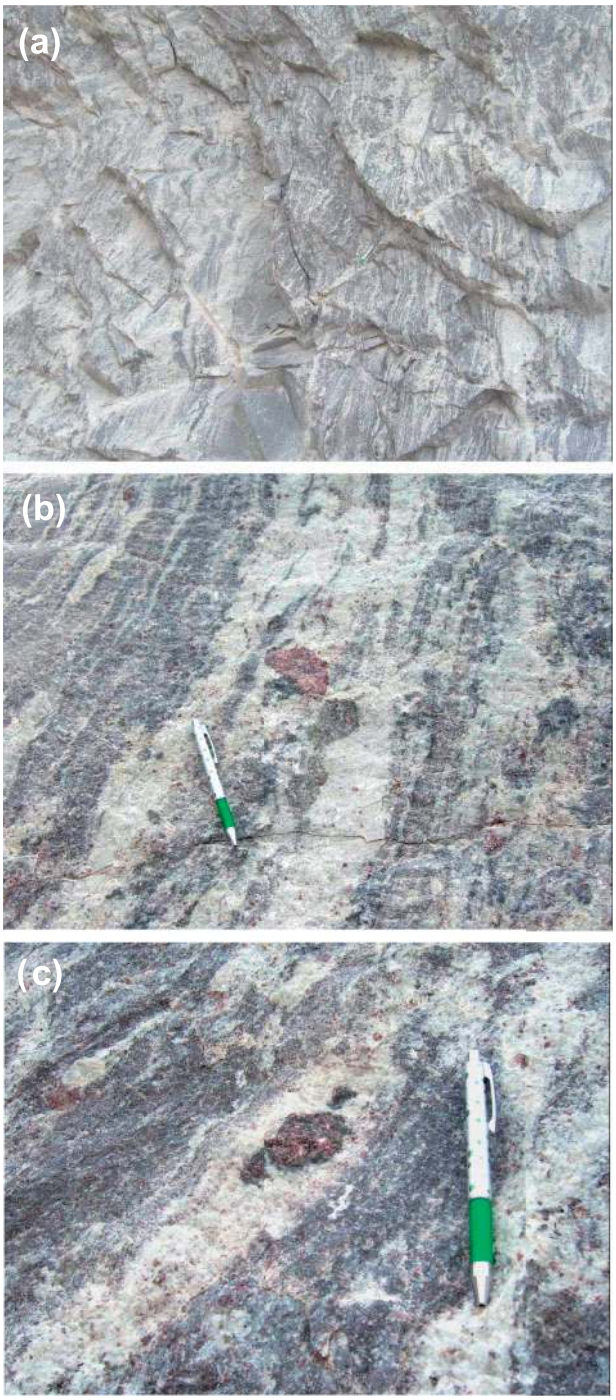


**Fig. 2.** (a) Kulappara Quarry, showing near-vertical fabric defined by gneissic layering comprising Grt + Sil + Crd + Ilm mesosomes, 1–2 cm width concordant to sub-concordant leucosome veins and lenses, and 5–20 cm width garnet-bearing leucogranite sheets. The shallowly dipping cross-cutting leucocratic vein (marked by the pen) should be noted. This vein and its margin form the sample KLP3. (b) Migmatitic cordierite-bearing pelite showing leucosomes occurring as pockets, patches and layer-parallel sheets that coalesce along their length over scales of 5–20 cm. Schlieren and patches rich in Grt + Sil or Grt + Crd + Sil alternate with leucocratic domains. Coarse subhedral porphyroblasts and cumuloblasts of garnet, partially pseudomorphed by cordierite, occur within and adjacent to the leucosomes. The broader leucosome in the centre of the field of view is along strike from the sample site for KLP1. (c) Close-up view of the Kulappara migmatitic gneiss. A large garnet cumulophyric domain is located within the leucosome; the adjacent mesosome is rich in Grt + Sil + Crd.

that locally preserve interstitial–subhedral textures characteristic of melt crystallization.

Sample KLP3, which incorporates the diffuse boundary between a leucogranite vein and its wall-rock, was selected for detailed petrography and microanalysis (Fig. 3). Image analysis of the whole KLP3 section including leucocratic and mesocratic horizons gives an overall estimate of 8 modal % garnet. The mesocratic part of KLP3 (30% of the thin section) consists of garnet (>30 modal %) + plagioclase (30 modal %) + perthitic K-feldspar (25 modal %) + ilmenite + minor biotite and sillimanite, with grain sizes in the range 300 μm to 2 mm. Garnet ($Pyp_{29–33}Alm_{69–65}Grs_2Sps_{0·5}$) forms subhedral to lobate–anhedral grains and grain clusters, and contains inclusions of fine sillimanite, rounded quartz, rare rounded brown biotite, and subhedral monazite (200–500 μm) (Fig. 3a). Subhedral zircon (200–300 μm) may be present towards and on the rims of garnets that face into or lie partially within an adjacent leucocratic layer (Fig. 3b).

The leucocratic domain in KLP3 contains garnet (<5 modal %) as isolated porphyroblasts similar in dimensions and inclusion assemblage to those in the melanocratic domain. Quartz, perthitic alkali feldspar and plagioclase form subhedral interlocking grains with lobate and sutured boundaries, or form interstitial textures with quartz present between the feldspar subhedra (Fig. 3c). Ilmenite is present, along with relatively abundant (>5%) monazite and zircon, in clusters (Fig. 3d). Whereas both monazite and zircon are strikingly abundant in the leucosome they are scarce within the local melanocratic domain. The detailed textural associations of zircon and monazite in KLP3 are described in subsequent sections.

## KULAPPARA (KLP) LITHOLOGY AND BULK-ROCK CHEMISTRY

Three samples representative of the Kulappara lithologies have been analysed for their bulk-rock major and trace element compositions. KLP1 is from a well-segregated garnet-bearing concordant leucosome, KLP2 is from a Grt + Sil + Crd mesosome, and KLP3 is from a thin discordant leucogranitic vein (Fig. 2c). Analyses are presented in Tables 1 and 2.

Major element compositions are illustrated in Fig. 4. The leucogranite vein KLP3 and leucosome KLP1 both plot as near-minimum melt compositions in terms of Qz–Ab–Or normative components, close to the

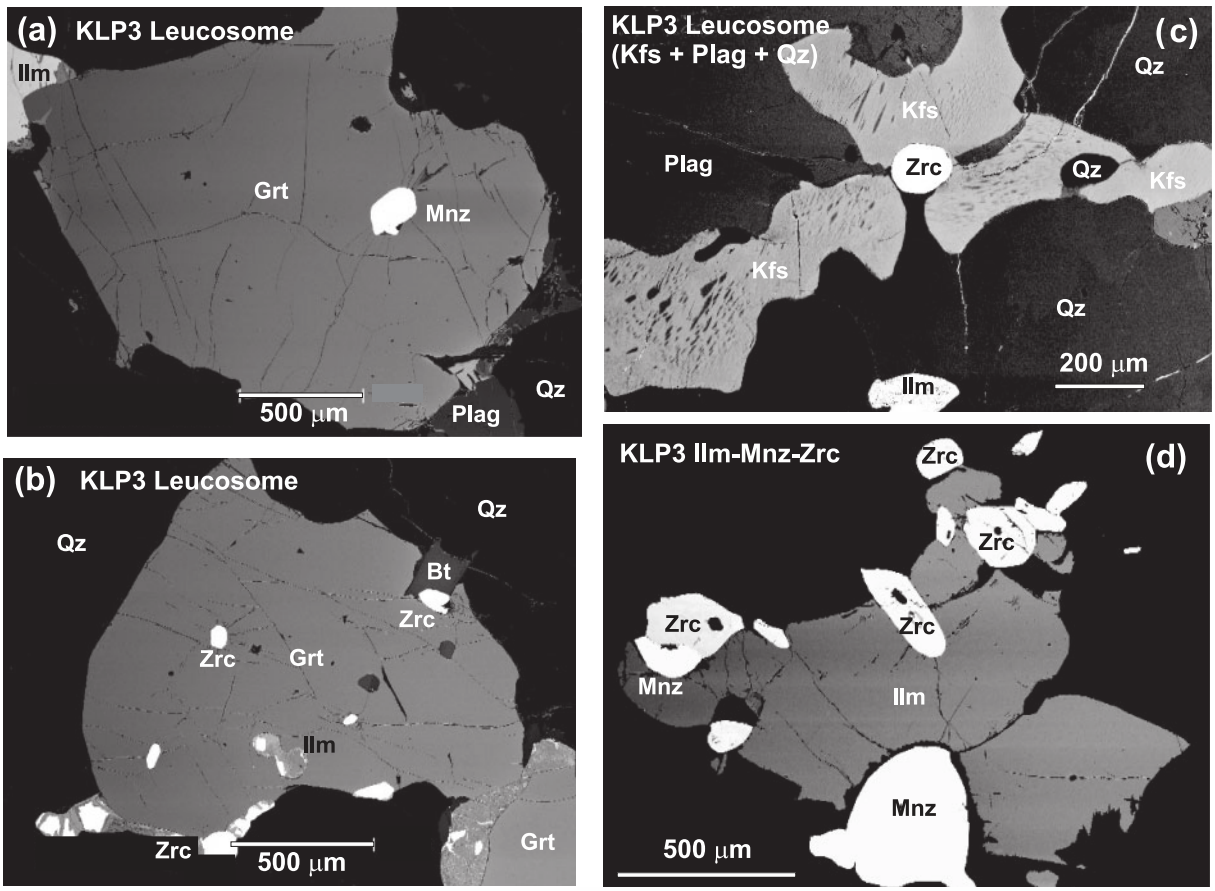


**Fig. 3.** Back-scattered electron (BSE) images of typical mineral textures in the garnet–ilmenite-rich domain of leucogranite KLP3. Scales shown by horizontal bars. (a) Subhedral garnet (Grt) containing an inclusion of monazite (Mnz), with Ilmenite (Ilm) restricted to the exterior of the garnet. The monazite in this garnet (Mnz2) preserves oscillatory euhedral growth zoning and records a chemical Th–U–Pb age of *c.* 535 Ma (see Fig. 7). (b) Subhedral garnet (Grt) containing inclusions of zircon (Zrc), and partially enclosing zircon on its margin (Z4a). Garnet also contains inclusions of quartz (Qz) and alkali feldspar (Kfs). Biotite (Bt) occurs on Grt, and ilmenite (Ilm) is always located exterior to or on garnet. (c) Typical leucosome texture involving Qz, plagioclase (Plag) and perthitic K-feldspar (Kfs), featuring re-entrant boundaries between Qz and Kfs, filaments of Qz between Kfs grains, rounded Qz within and on Kfs, and zircon located at multi-grain boundaries that are not triple points. These textures are interpreted as modified melt textures. (d) Typical grain cluster texture involving zircon (Zrc), monazite (Mnz) and ilmenite (Ilm). Zircon occurs as separate euhedral and multi-grain clusters, partially enclosed along with monazite by later ilmenite. The zircon on the left side of the field of view (Z5) forms a lobate boundary with monazite and both grains are then enclosed by Ilm. This supports the late-stage crystallization of ilmenite in this bulk composition, after zircon and monazite formation.

experimentally determined wet granite minimum in haplogranitic systems (Johannes & Holtz, 1996; Patiño-Douce & Beard, 1995) (Fig. 4a). Projection of the normative bulk-rock compositions from Qz + Plag + Or onto the AFM plane (Fig. 4b) shows that the three rocks broadly lie on a sillimanite + garnet control trend between peraluminous leucogranite (KLP1: ASI >1·2, A/AFM = 66) and a slightly more magnesian garnet-rich mesosome (KLP2: ASI >1·7, A/AFM = 37), which has a higher combined AFM component relative to the felsic components. KLP3 lies between these in terms of its AFM components.

Trace elements follow the AFM trend. Rb, Ba, Sr and Pb are high in the leucogranite vein KLP3 and leucosome KLP1 but lower in the mesosome KLP2. Those trace elements compatible in garnet or ilmenite (V, Cr, Mn, Nb) are highest in KLP2. REE and Y abundances are correlated with ASI, total Fe + Mg, and normative garnet. Leucosome KLP1 has lower REE than the other samples, with LREE less than 60 times chondrite, a positive Eu anomaly and flat to slightly U-shaped HREE at 2–4 times chondrite (Fig. 5). Mesosome KLP2 has high relative LREE (280–100 times chondrite) and is enriched in HREE relative to both the concordant leucosome and discordant leucogranite vein (Fig. 5). The leucogranite vein KLP3 has the highest LREE and preserves a sloping REE pattern from La to Ho, and then flat HREE at 5–7 times chondrite (Fig. 5).

The whole-rock Zr contents have been used to calculate zirconium saturation temperatures (Watson & Harrison, 1983). Leucogranitic vein KLP3 (44 ppm Zr) yields a saturation $T$ of 700°C and leucosome KLP1 (62 ppm Zr)

*Table 1: Kulappara major element compositions*

| Sample: | KLP1 | KLP2 | KLP3 |
|---|---|---|---|
| $SiO_2$ | 74·93 | 66·20 | 73·30 |
| $TiO_2$ | 0·03 | 0·67 | 0·37 |
| $Al_2O_3$ | 14·73 | 16·03 | 14·01 |
| $Fe_2O_3$ | 1·19 | 6·58 | 2·29 |
| MnO | 0·02 | 0·09 | 0·03 |
| MgO | 0·17 | 1·69 | 0·48 |
| CaO | 0·67 | 1·16 | 1·21 |
| $Na_2O$ | 2·67 | 2·33 | 2·73 |
| $K_2O$ | 5·53 | 3·25 | 4·72 |
| $P_2O_5$ | 0·14 | 0·07 | 0·10 |
| Sum | 100·05 | 98·07 | 99·22 |
| *Normative components* | | | |
| Apat | 0·07 | 0·04 | 0·05 |
| Ilm | 0·04 | 1·0 | 0·5 |
| Opx | 2·2 | 13·4 | 4·2 |
| An | 1·0 | 2·2 | 2·2 |
| Ab | 9·9 | 8·6 | 10·3 |
| Or | 13·2 | 7·8 | 11·5 |
| Qz | 69·6 | 59·4 | 68·3 |
| Crn | 4·0 | 7·7 | 2·9 |
| *wt % components Qz:Ab:Or* | | | |
| Qz | 40·0 | 44·6 | 41·1 |
| Ab | 24·9 | 28·3 | 27·0 |
| Or | 35·1 | 27·0 | 31·9 |
| *wt % components Qz:Plag:Or* | | | |
| Qz | 39·0 | 41·5 | 38·7 |
| Plag | 26·8 | 33·4 | 31·3 |
| Or | 34·2 | 25·1 | 30·0 |
| molec. ASI | 1·28 | 1·71 | 1·20 |
| $X_{Mg}$ | 22·1 | 33·7 | 29·5 |
| A/AFM | 0·63 | 0·39 | 0·36 |

ASI, Aluminium Saturation Index = molecular $Al_2O_3/(Na_2O + K_2O + CaO)$

*Table 2: Kulappara trace elements and REE*

| Sample: | KLP1 | KLP2 | KLP3 |
|---|---|---|---|
| *Trace elements (ppm)* | | | |
| Sc | 3·1 | 5·5 | 3·3 |
| V | 3·8 | 12·8 | 5·8 |
| Cr | 12·8 | 13·2 | 13·0 |
| Co | 1·6 | 16·5 | 4·0 |
| Ni | 0·9 | 6·6 | 1·4 |
| Cu | 0·4 | 1·3 | 0·5 |
| Zn | 12·2 | 32·0 | 12·6 |
| Ga | 14·4 | 18·1 | 18·0 |
| Rb | 215·8 | 158·4 | 196·5 |
| Sr | 156 | 130·3 | 205·3 |
| Y | 5·6 | 41·2 | 13·4 |
| Zr | 62·5 | 119·9 | 44·2 |
| Nb | 0·4 | 15·7 | 7·7 |
| Ta | 0·05 | 0·8 | 0·4 |
| Cs | 0·7 | 0·3 | 0·3 |
| Ba | 807 | 588 | 1084 |
| Hf | 2·0 | 3·6 | 1·3 |
| Pb | 15·9 | 9·4 | 14·5 |
| Th | 5·4 | 10·0 | 31·7 |
| U | 1·1 | 2·7 | 1·6 |
| Th/U | 4·9 | 3·7 | 19·7 |
| Rb/Sr | 1·4 | 1·2 | 1·0 |
| Ba/Rb | 3·7 | 3·7 | 5·5 |
| Ba/Sr | 5·2 | 4·5 | 5·3 |
| Sr/Y | 27·8 | 3·2 | 15·3 |
| Zr/Y | 11·1 | 2·9 | 3·3 |
| Zr/Nb | 168·4 | 7·6 | 5·8 |
| Nb/Ta | 7·6 | 18·9 | 17·5 |
| *Rare earth elements (ppm)* | | | |
| La | 10·9 | 64·1 | 91·9 |
| Ce | 20·6 | 121·7 | 176·6 |
| Pr | 2·1 | 12·4 | 18·0 |
| Nd | 7·2 | 44·5 | 63·5 |
| Sm | 1·2 | 8·4 | 8·8 |
| Eu | 1·0 | 1·1 | 1·5 |
| Gd | 0·8 | 7·3 | 5·4 |
| Tb | 0·1 | 1·1 | 0·6 |
| Dy | 0·8 | 7·1 | 2·5 |
| Ho | 0·1 | 0·8 | 0·3 |
| Er | 0·4 | 2·6 | 0·9 |
| Tm | 0·06 | 0·34 | 0·09 |
| Yb | 0·64 | 3·47 | 0·99 |
| Lu | 0·11 | 0·59 | 0·15 |

(continued)

735°C. The Zr content of the mesosome (KLP2) is higher (120 ppm), but cannot be used to infer a saturation temperature given the migmatitic character of this rock.

## PHASE EQUILIBRIUM MODELLING FROM BULK-ROCK COMPOSITIONS

The bulk-rock compositional data described above and presented in Table 1 have been recast into molar proportions and used to calculate equilibrium phase diagrams

(pseudosections) for the three rocks (KLPl, KLP2, KLP3) over the $P$–$T$ field 4–10 kbar and 750–900°C. The Theriak-Domino software of de Capitani & Petrakakis (2010) (updated domino 03-01-2012 version) was used in concert with THERMOCALC (Holland & Powell, 1998) database tcdb55c2d to calculate phase diagrams in NCKFMASHT at 0·5, 1, 2 and 3 wt % $H_2O$ for each rock and isolines of garnet composition ($X_{Mg}$, $X_{grs}$) and garnet mode in the case of KLP3. KLP3 was also investigated for the first appearance of garnet on cooling when the rock composition is adjusted following the extraction of up to *c.* 5 wt % of potential wall-rock garnet from its overall composition. Activity–composition relations used for the phases were those of White *et al.* (2007) for biotite, garnet and melt, White *et al.* (2002) for orthopyroxene and spinel–magnetite, White *et al.* (2000) for ilmenite, Holland & Powell (2003) for the feldspars, and Holland & Powell (1998) for hydrous cordierite.

*Table 2: Continued*

| Sample: | KLP1 | KLP2 | KLP3 |
|---|---|---|---|
| *Chondrite-normalized REE* | | | |
| La | 46·3 | 273·2 | 391·4 |
| Ce | 34·1 | 201·7 | 292·8 |
| Pr | 23·0 | 139·5 | 201·8 |
| Nd | 15·8 | 98·3 | 140·3 |
| Sm | 8·1 | 57·1 | 59·9 |
| Eu | 18·5 | 19·0 | 26·3 |
| Gd | 3·9 | 36·9 | 27·5 |
| Tb | 3·0 | 30·6 | 15·3 |
| Dy | 3·3 | 29·1 | 10·2 |
| Ho | 1·7 | 13·8 | 4·7 |
| Er | 2·3 | 16·6 | 5·7 |
| Tm | 2·3 | 14·0 | 3·7 |
| Yb | 4·0 | 21·3 | 6·1 |
| Lu | 4·4 | 24·1 | 6·3 |
| U/Yb | 1·7 | 0·8 | 1·6 |

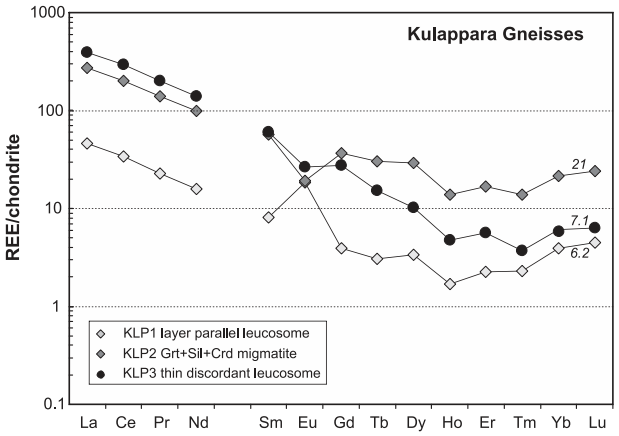


**Fig. 5.** Chondrite-normalized REE diagram depicting the REE patterns of the studied Kulappara leucogranites (KLPl, KLP3) and migmatitic pelite (KLP2). Chondrite values from Anders & Grevesse (1989).

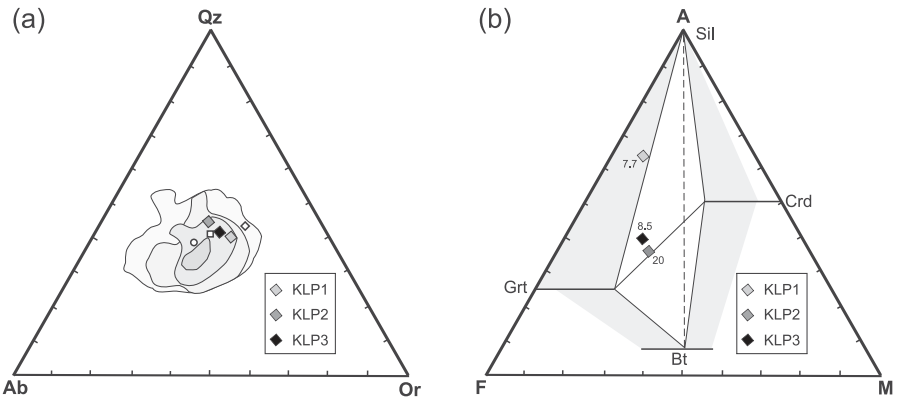


**Fig. 4.** Bulk-rock chemical features of Kulappara gneisses. (a) Normative Qz–Ab–Or diagram showing the composition of KLPl, KLP2 and KLP3 in terms of their felsic components. Fields with increased densities of grey shade express the frequency distribution of 1190 granitic rocks (Winkler & von Platten, 1961). Open diamond, square and circle show experimental minimum melting points in the system Ab–Or–Qz–$H_2O$, at 1 kbar water pressure (James & Hamilton, 1969) modified for 0, 3 and 5 wt % of An in the system, respectively. (b) AFM diagram projected from Qz, Ab, Or and An components, showing the position of the projected bulk-rock compositions for KLPl, KLP2 and KLP3 in terms of potential constituent AFM minerals (Sil, Grt, Crd, Bt), uncorrected for Ti that may be present in ilmenite. Compositional fields for Grt, Bt and Crd are based on the mineral compositions reported in previous studies (Nandakumar & Harley, 2000; Braun & Bröcker, 2004). The three samples (denoted by diamonds) are characterized by their total AFM content (normative proportions) given by the numbers in italics. KLPl has high Sil relative to Grt, though total AFM is low so the overall normative abundance of Sil is a few per cent, consistent with petrographic observation. KLP3 lies on a Grt + Sil tie-line at low Sil content, consistent with petrography. KLP2 has a significantly higher total AFM component content, and is rich in Grt + Crd (and/or Bt) relative to sillimanite.

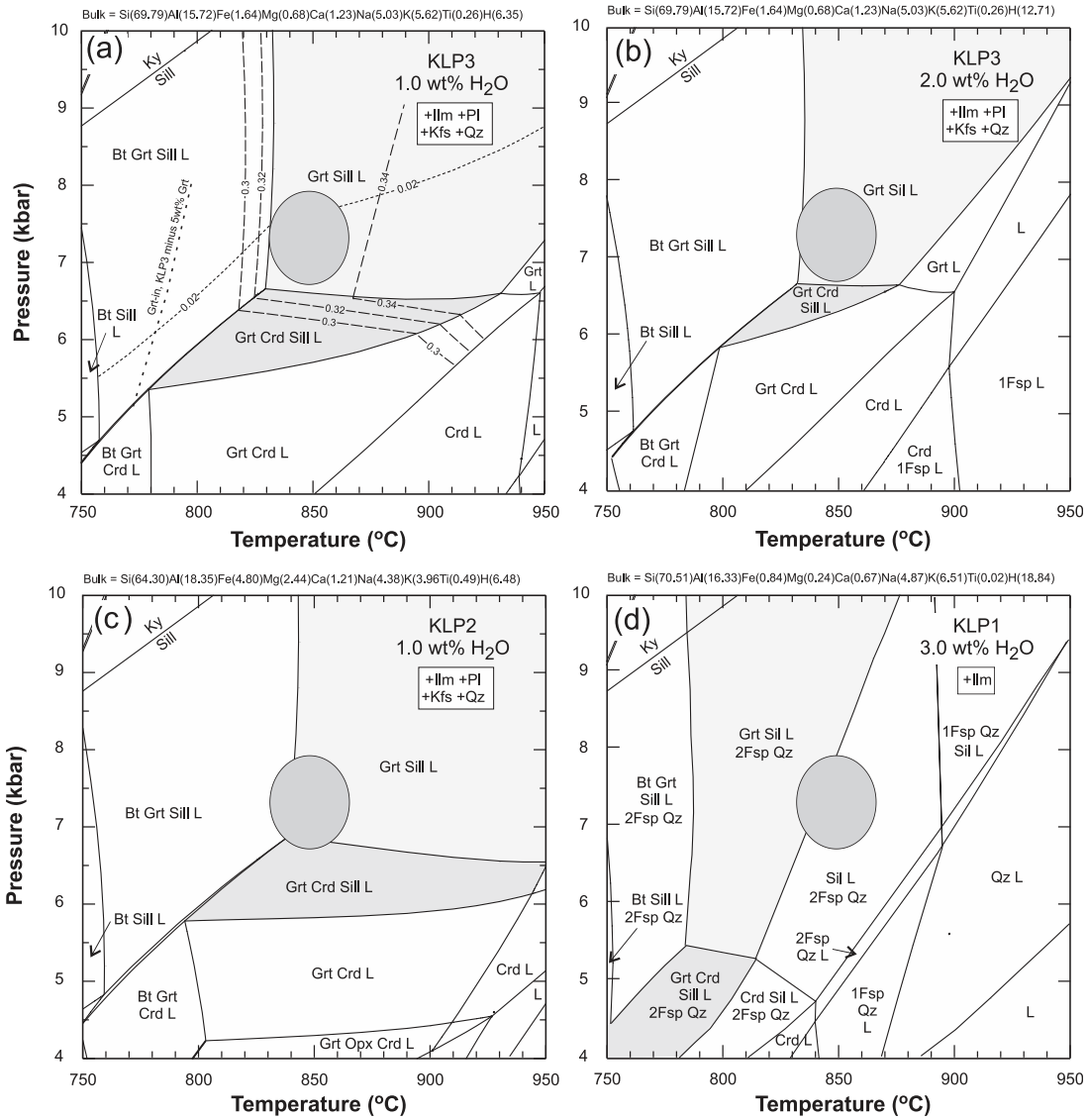


**Fig. 6.** Calculated pressure–temperature phase diagrams (pseudosections) for KLP3, KLP2 and KLP1 at selected $H_2O$ contents in the system NCKFMASHTO, with all Fe assumed to be in the divalent state. Calculated using Theriak-Domino [de Capitani & Petrakakis (2010), updated software version 03-01-2012], applying the THERMOCALC (Holland & Powell, 1998) dataset version tcdb55c2d. Bulk-rock compositions are recast in terms of cations and given at the top of each diagram. (a) and (b) are calculated for leucogranite KLP3 at two $H_2O$ contents, with the 2 mol % $X_{Grs}$ isopleth and $X_{Mg}$ 30–34 isopleths in garnet calculated and superimposed on the Grt + Sil + Qz + 2 Feldspars + Ilm + L and adjacent assemblage fields. The dashed line labelled 'Grt-in, KLP3 minus 5 wt % Grt' in (a) shows the low-$T$ incoming of garnet in a KLP3 composition modified following extraction of 5 wt % of entrained or accumulated garnet ($X_{Grs} = 2$ mol %; $X_{Mg} = 33$). (c) and (d) are for migmatitic pelite KLP2 with 1 wt % $H_2O$ and leucosome KLP1 with 3 wt % $H_2O$ respectively. In all diagrams the elliptical shaded field denotes the minimum $P$–$T$ conditions required by the mineral assemblage and garnet composition preserved in KLP3 modelled as a closed-system composition.

Selected NCKFMASHT phase diagrams, calculated assuming no $Fe^{3+}$, are presented in Fig. 6. In the case of KLP3 varying $H_2O$ content from 0·5 to 2 wt % had only a very minor effect on the positions of the key reactions constraining the stability field of the observed Grt + Ilm + 2 Feldspars + Qz ± Sill ± Bt assemblage. This assemblage is constrained by the absence of cordierite, late appearance of biotite, and low abundance of sillimanite to lie at minimum $P$–$T$ conditions of 6·6 kbar and 835°C. Isopleths of grossular ($X_{grs} < 2$ mol %) and $X_{Mg}$ (garnet) between 32 and 34 further constrain the $P$–$T$ of garnet equilibration to lie in the field defined by the dark shaded ellipse in Fig. 6 ($P = 6{\cdot}6$–$7{\cdot}8$ kbar; $T = 835$–$870$°C). This minimum $P$–$T$ constraint also satisfies the phase assemblage observed in KLP2, Grt + Crd + Sil + Qz + Bt + Ilm + 2 Feldspars, with cordierite occurring principally as a secondary rind on garnet. The pseudosection calculations indicate that it is possible that peak temperatures

were considerably higher, as the Grt + Sil + Qz + Ilm + 2 Feldspars assemblage of KLP2 is stable to beyond 950°C (Fig. 6c). Although minor spinel occurs with ilmenite and sillimanite or rarely as inclusions with feldspar within coarse garnet porphyroblasts in some Kulappara migmatite samples, it is not present in thin sections of KLP2, consistent with the calculated NCKFMASHT system pseudosection for this sample. The simple phase assemblage in KLP1 (Grt + Sil + Ilm + 2 Feldspars + Qz) is compatible with this *P*–*T* estimate and provides no further constraints.

Modal calculations using the preserved KLP3 bulk composition show that the number of moles (and hence modal % and wt %) of garnet increases markedly down temperature in the biotite-absent field. For example, garnet content doubles from 0·3 to 0·6 moles from 930°C to 830°C at 7 kbar, for KLP with 1 wt % $H_2O$. On the incoming of biotite at *c.* 830°C garnet proportion decreases dramatically, halving to 0·3 moles by 780°C and 7 kbar with the formation of biotite. Hence, garnet growth in KLP3 can occur either with melting on a prograde heating path through the Bt + Grt + Sil + L field at $T < 830$°C, or on cooling from $T > 900$°C to 830°C in the Grt + Sil + L field, if $P > 6{\cdot}5$ kbar.

As noted in the mineralogy and petrography section, sample KLP3 includes leucocratic vein material and more mesocratic horizons in which garnet is concentrated. It is possible that this garnet has been entrained into or accumulated in the leucocratic vein, so that the preserved KLP3 bulk composition effectively represents leucogranite + additional garnet. To investigate the phase equilibrium effects of this, 5 wt % of garnet has been extracted from KLP3, equivalent to the amount of garnet concentrated in its mesocratic layers, to produce a residual leucogranitic KLP3 composition. Theriak-Domino modelling of this composition in NCKMASHT at 6·5–7·5 kbar indicates that garnet would coexist with melt at $T < 850$°C for 1 wt % $H_2O$ in the bulk composition, <815°C for 1·5 wt % $H_2O$ in the bulk composition, and <780°C if the bulk composition contained 2 wt % $H_2O$. For comparison, the granitic leucosome KLP1 modelled at 3 wt % $H_2O$ and 7 kbar is calculated to crystallize garnet at $T < 840$°C.

## KLP3 GARNET AND FELDSPAR TRACE ELEMENT CHEMISTRY

Garnet is the principal Fe–Mg silicate phase present adjacent to and within the leucogranite vein KLP3. It may contain included monazite or zircon, or share grain boundaries with zircon (Fig. 3b). Trace element and REE analyses of KLP3 garnets located within the leucogranite vein are presented in Table 3. The garnet is homogeneous in Ca (0·69 wt %), Y (210 ppm), Ti (180 ppm) and Zr (39 ppm). Its REE patterns are characterized by extreme negative Eu anomalies (Eu/Eu* *c.* 0·008), flat HREE ($Yb_n/Gd_n = 1{\cdot}2$) at $Dy_n$ of 165, $Sm_n/Nd_n$ near 11 and strong depletions in LREE (Fig. 7).

Partial REE analyses from La to Gd have also been performed on plagioclase (An21) and perthitic K-feldspar in KLP3 (Table 3). The HREE are represented by Y, which is plotted at the position of Ho on the chrondrite-normalized REE plot of Fig 7. K-feldspar shows typical feldspar REE features (e.g. Watt & Harley, 1993; Bea *et al.*, 1994; Bea, 1996) in its very low middle REE (MREE)–HREE and strong positive Eu anomaly. However, it also exhibits a strong enrichment in LREE, with $La_n/Sm_n$ of *c.* 66 and La at up to 200 times chondrite. Plagioclase preserves a distinctive REE chemistry, with all LREE to Nd being >100 times chondrite, $La_n/Sm_n$ of *c.* 10, and the Eu anomaly being only weakly positive because of the relatively high Sm and Gd contents. Eu abundances are similar in both feldspars, at *c.* 20–40 times chondrite.

## ZIRCON IN LEUCOGRANITE KLP3

### Zircon petrography and microtextural features

Zircon is abundant in KLP3. For example, more than 40 grains with diameters of 50–200 μm have been observed in the 5 mm wide quartz–perthite–plagioclase leucosome layer present in the analysed thin section. These zircons occur in four textural settings, as follows.

(1) As single or clustered multifaceted, sub-elongate to equant grains 50–250 μm in diameter set within the quartz–feldspar matrix, generally at grain boundaries (Fig. 3c).
(2) As euhedral to subhedral equant and elongate grains forming composite clusters with monazite. Curviplanar grain boundaries are typical when in contact with monazite, which appears to partially enclose the zircons in some domains (Fig. 3d).
(3) As grain clusters, both with and without monazite, partially enclosed by or attached to and sharing granoblastic grain boundaries with ilmenite or magnetite within leucosome (Fig. 6d).
(4) As 50–200 μm diameter grains or groups of grains adjacent to, or partially to wholly enclosed within garnet facing into leucosome (Fig. 3b). Only one zircon wholly enclosed within garnet (planar zoned zircon Z4b) has been identified and analysed in this study.

Zircon internal textures were characterized using secondary electron imaging (SEI), backscattered electron (BSE) and cathodoluminescence (CL) imaging. CL imaging (15 kV and 5 nA) reveals pronounced internal zoning textures that can be divided into three types: complex cores, planar-sector to sector-oscillatory zoned euhedral rim

*Table 3: Kulappara feldspar and garnet trace element compositions*

| | Kfs | Plag | grt1 | grt2 | grt3 | grt4 | grt5 | Grt av. |
|---|---|---|---|---|---|---|---|---|
| Ca (ppm) | 2377 | 31319 | 4888 | 4579 | 4622 | 5705 | 4725 | 4904 |
| CaO (wt %) | 0·33 | 4·38 | 0·68 | 0·64 | 0·65 | 0·80 | 0·66 | 0·69 |
| *ppm* | | | | | | | | |
| P | | | 329 | 351 | 362 | 334 | 311 | 337 |
| Y | 0·04 | 0·6 | 201 | 204 | 206 | 214 | 228 | 211 |
| Zr | | | 38 | 40 | 38 | 39 | 39 | 39 |
| Ti | | | 179 | 183 | 141 | 241 | 180 | 185 |
| La | 51 | 137 | 0·005 | 0·003 | 0·003 | 0·007 | 0·003 | 0·004 |
| Ce | 45 | 217 | 0·01 | 0·06 | 0·07 | 0·04 | 0·09 | 0·06 |
| Pr | 2·7 | 20 | 0·05 | 0·09 | 0·08 | 0·10 | 0·07 | 0·08 |
| Nd | 6·1 | 65 | 2·0 | 1·8 | 1·6 | 2·2 | 1·6 | 1·8 |
| Sm | 0·5 | 6·9 | 6·3 | 6·3 | 5·9 | 7·0 | 6·7 | 6·4 |
| Eu | 1·7 | 2·4 | 0·02 | 0·05 | 0·05 | 0·05 | 0·02 | 0·04 |
| Gd | 0·2 | 3·0 | 22 | 23 | 24 | 21 | 23 | 23 |
| Tb | | | 5·0 | 5·4 | 5·1 | 4·9 | 5·1 | 5·1 |
| Dy | | | 39 | 39 | 42 | 39 | 41 | 40 |
| Ho | | | 7·7 | 7·5 | 7·8 | 8·2 | 8·7 | 8·0 |
| Er | | | 23 | 22 | 22 | 21·5 | 26 | 23 |
| Tm | | | 3·1 | 3·0 | 3·3 | 3·1 | 4·2 | 3·3 |
| Yb | | | 24 | 22 | 23 | 18 | 25 | 22 |
| Lu | | | 3·3 | 3·4 | 3·4 | 2·9 | 3·9 | 3·4 |
| *Chondrite-normalized* | | | | | | | | |
| La | 217 | 583 | 0·02 | 0·01 | 0·01 | 0·03 | 0·01 | 0·02 |
| Ce | 75 | 360 | 0·01 | 0·10 | 0·12 | 0·07 | 0·16 | 0·09 |
| Pr | 30 | 219 | 0·6 | 1·0 | 0·9 | 1·2 | 0·8 | 0·9 |
| Nd | 13 | 143 | 4·4 | 3·9 | 3·5 | 4·9 | 3·5 | 4·0 |
| Sm | 3·4 | 47 | 43 | 43 | 40 | 48 | 46 | 44 |
| Eu | 31 | 43 | 0·4 | 0·9 | 0·9 | 0·9 | 0·4 | 0·7 |
| Gd | 0·9 | 15 | 111 | 115 | 123 | 109 | 119 | 115 |
| Tb | | | 137 | 148 | 141 | 136 | 139 | 140 |
| Dy | | | 161 | 159 | 174 | 160 | 168 | 164 |
| Ho (Y) | 0·03 | 0·4 | 138 | 135 | 141 | 147 | 157 | 144 |
| Er | | | 144 | 138 | 136 | 135 | 165 | 144 |
| Tm | | | 127 | 125 | 136 | 129 | 175 | 138 |
| Yb | | | 147 | 134 | 143 | 108 | 151 | 136 |
| Lu | | | 138 | 141 | 141 | 118 | 160 | 140 |
| Sm/Nd | 0·08 | 0·11 | 3·2 | 3·6 | 3·7 | 3·1 | 4·3 | 3·5 |
| Eu/Eu* | 14·5 | 1·4 | 0·005 | 0·011 | 0·011 | 0·011 | 0·004 | 0·01 |
| Yb/Gd | | | 1·3 | 1·2 | 1·2 | 1·0 | 1·3 | 1·2 |

domains ('bright planar' and 'dark planar' in CL), and curviplanar to lobate darker-CL rims or rinds that may have the appearance of invasive or replacive lobes (Z2a, Z5z, Z3), which appear to transgress across planar-sector zones into the complex core domains (Figs 8 and 9).

Complex cores, present in most zircons irrespective of textural setting, are spectacular in their internal CL geometries. Several grains show complete 'cores' that have bright-CL square cross-sections, divided into four or eight sectors by axial zones of medium-CL zircon that form 'spokes' decorated with fine feathers of medium-CL zircon. The geometric centres of these cores are darker in CL and coincide with the intersection of these feathered axial zones (e.g. Z5z). The four bright sectors between the

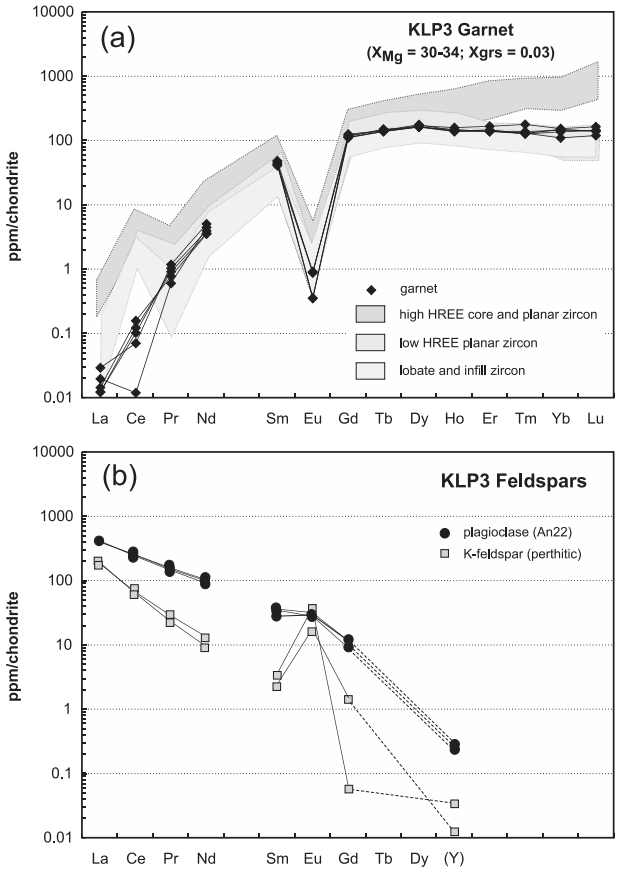


**Fig. 7.** (a) Chondrite-normalized REE patterns of KLP3 garnets. Chondrite values from Anders & Grevesse (1989). Shaded fields behind the garnet data show the range of REE contents in the three zircon types distinguished on textural and Th/U grounds described in the text and presented in Fig. 10. (b) Feldspar REE patterns, including all LREE and MREE from La to Dy. Y is plotted as a proxy for Ho, which has a similar ionic radius and degree of compatibility.

principal tetragonal axes of medium-CL zircon are further typified by containing either an inclusion of finely crystalline quartzofeldspathic material or a circular to elliptical domain of markedly oscillatory-zoned zircon cored by medium- or dark-CL zircon. In some grains the latter domains are continuous with lobes of invasive darker-CL zircon. These features are exemplified by zircon Z2a (Fig. 8a), a composite grain that preserves two complex cores, one of which has later been disrupted and replaced by a truncating domain of structureless dark-CL zircon. This disrupted 'core' still preserves its axial feathered zones and one inclusion, but the other three sectors are strongly modified by darker-CL lobes that also replace or truncate the planar-sector zones otherwise present outside the 'core' region. The other complex core is mostly intact, with one inclusion, two circular oscillatory domains and one invasive lobe or cuspate zone truncation. Zircon Z5 (Fig. 8b) displays very similar complex core internal structures, especially seven (out of eight) axial 'feathered' zones and one quartz–feldspar microcrystalline inclusion with a negative crystal shape, interior to invasive or enveloping lobate rims. Zircon Z10 preserves one feathered core domain with a quartz–feldspar microcrystalline inclusion that has a modified negative crystal shape, interior to moderately oscillatory planar-sector zircon (Fig. 8c).

Planar-sector zoned zircon occurs surrounding or partially surrounding the complex cores (Figs 8 and 9). In detail there are two planar-sector zone types: those that are slightly brighter in CL ('bright planar') and moderately oscillatory (e.g. Z2, Z5, Z6c, Z10), and those that are slightly darker in CL ('medium planar') and weakly oscillatory (Z4a, Z4c, Z5yc: Fig. 9). Quartz and quartzofeldspathic inclusions are absent from the planar-sector zoned zircon. In most zircons texturally constrained timing relationships between complex zircon core domains and the planar-sector zircon domains are ambiguous. However, the two zircon cores in Z2 are both overgrown by a shared sector of bright planar zircon (Fig. 8a), suggesting that the latter zones grew on two earlier cores that had coalesced, prior to the later disruption of one of the cores and the planar zircon by lobate zircon (Fig. 8a).

Both 'core' and 'planar-sector' type zircon domains are variably overprinted, modified or replaced by lobate, curviplanar and cuspate zircon domains ('lobate zircon') that also form partial rims or outermost rinds on most grains (Z2, Z4a, Z5, Z6bc, Z6c, Z10). In some grains (e.g. Z6bc, Z6c; Fig. 9) this modified zircon, which forms swirling or curved CL patterns with a bright-CL inner horizon followed by darker-CL or variable-CL material, is responsible for curviplanar to lobate zircon grain shapes against other phases. These grains may also show severe modification of the remaining interior complex core zones, with former axial 'feathered' domains being curved and distorted (e.g. Z6bc; Fig. 9). Truncation textures observed under CL indicate that lobate zircon, whether on rims or invasive into complex cores and forming elliptical domains at sites where quartzofeldspathic material may otherwise have occurred, was produced in the final phases of zircon formation and modification in KLP3 (e.g. Z5; Fig. 8b).

## Zircon trace element and REE chemistry

REE and additional trace element results for zircon are provided in Table 4 and presented in the form of chondrite-normalized REE plots (Fig. 10) normalized against values of Anders & Grevesse (1989), and complementary discriminant diagrams involving the ratios Th/U, U/Yb and $Yb_n/Gd_n$ (Figs 11 and 12).

Chemical features common to all Kulappara zircons include $HfO_2$ contents in the range 1·35–1·65 wt % and consistent Ti contents of 10·5–15·2 ppm. All zircon textural types (complex core, planar-sector and lobate types) are typified by weak positive Ce anomalies ($Ce/Ce^* = 24–60$) and extreme negative Eu anomalies ($Eu/Eu^* = 0·02$).

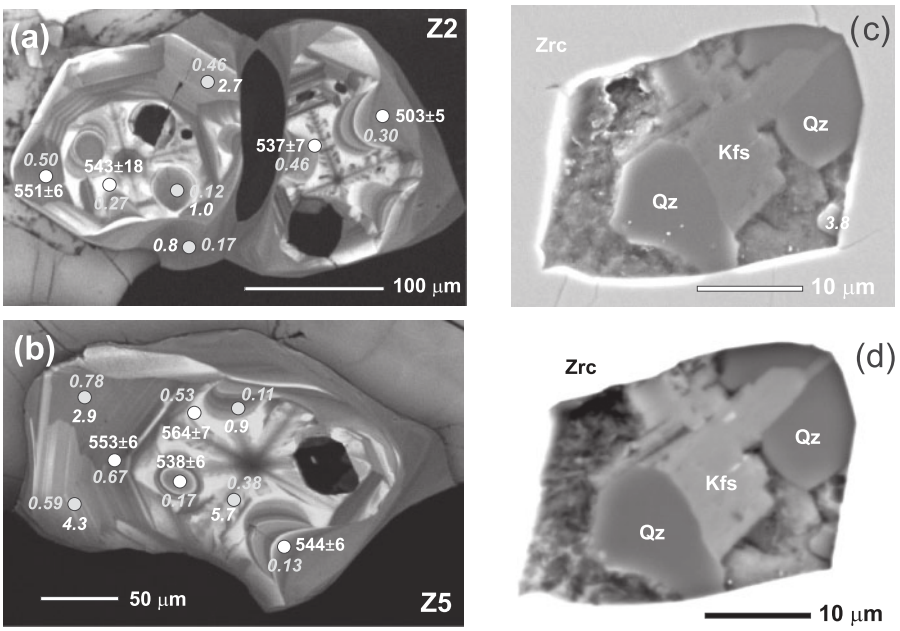


**Fig. 8.** (a, b) CL images of KLP3 zircons Z2 and Z5, referred to in the text and listed in Table 4, with scale given by the horizontal scale bars. Numbers in white with errors indicated are the $^{206}Pb/^{238}U$ ages determined at the white circled points. Grey italic numbers indicate Th/U ratio at each analysis point; white italic numbers, U/Yb ratio. White spots are those analysed for U–Pb geochronology and grey spots those analysed for REE and trace elements. The spectacular feathered cores, and negative crystal crypto- to microcrystalline inclusions preserved in these, should be noted. (c) BSE image of an example of a cryptocrystalline polygrain inclusion in zircon (Z10). (d) Secondary electron image of the same inclusion as shown in (c).

Complex 'feathered' cores (Z2a, Z5, Z10) and most sector-planar zoned zircon are characterized by moderate HREE enrichments ($Yb_n/Gd_n = 5{\cdot}7–2{\cdot}7$) at varied total HREE, with $Dy_n$ varying between 140 and 520 (Fig. 10a). Th/U ratios for these HREE-enriched cores and sector-planar domains range from >0·3 to 0·8 at 180–400 ppm U, and U/Yb is low (<4). The relatively 'high' Th/U ratios coupled with high $Yb_n/Gd_n$ and Y (= 700 ppm) distinguish this zircon chemical group from a small population of planar-zoned zircon (Z4a, Z4c, Z5yc) analyses and from the lobate-invasive and infilling zircon (Fig. 10b and c). This zircon chemical group is referred to as the 'higher Th/U group' in subsequent discussion.

Weakly zoned, medium-CL but undisturbed planar zircon sectors in Z4a, Z4c and Z5yc, elliptical or circular modified core zircon, and most examples of lobate invasive zircon, are characterized by flat HREE ($Yb_n/Gd_n = 0{\cdot}9$) at $Dy_n$ near 130. Th/U is low ($0{\cdot}2 \pm 0{\cdot}1$) in comparison with the brighter-CL sector-planar zoned zircon described above, mainly because of lower Th contents (75 ppm compared with 175 ppm). The flat HREE and low Yb contents result in elevated U/Yb (20–64) and U/Y (1–4·3) ratios that clearly distinguish these zircons domains from the higher Th/U group (Figs 10b, c and 11a). The weakly zoned, medium-CL planar zircon can be chemically distinguished from the lobate and infill zircon based on their slightly higher Th/U (0·22–0·32) and lower U/Y (1·1–1·7) at low $Yb_n/Gd_n$ (Fig. 11b). The two zircon chemical–textural groups are referred to as the 'lower Th/U group' and 'lobes and infills' in subsequent discussion.

## Ti-in-zircon thermometry

The Ti-in-zircon geothermometer (Watson *et al.*, 2006; Ferry & Watson, 2007) has been applied to estimate minimum temperatures of crystallization and modification of the KLP3 zircons. Ti contents are listed in Table 4, reported along with Ti-in-zircon temperatures in Supplementary Data Electronic Appendix 2, and summarized for each textural–chemical zircon group in Fig. 10. All zircon domains preserve Ti contents in the range 10·4–15·2 ppm. High Th/U, high-HREE feathered cores and sector-planar zoned zircon have identical average Ti contents ($12{\cdot}2 \pm 1{\cdot}2$ ppm and $12{\cdot}2 \pm 1{\cdot}6$ ppm respectively), and flat-HREE planar zoned zircon yields $13{\cdot}7 \pm 1{\cdot}3$ ppm, but with only three analyses this can be regarded as indistinguishable from the other domains.

As the coexisting Ti-phase in KLP3 is ilmenite rather than rutile, $a_{TiO2}$ is less than unity and the temperatures calculated are minima. The minimum Ferry & Watson (2007) temperatures are $779 \pm 8°C$ for high Th/U, high-HREE zircon, $792 \pm 10°C$ for the lower Th/U, flat-HREE planar zircon, and $780 \pm 13°C$ for the lower-HREE lobes and invasive domains. Taken as a single group the whole population yields a mean minimum temperature of

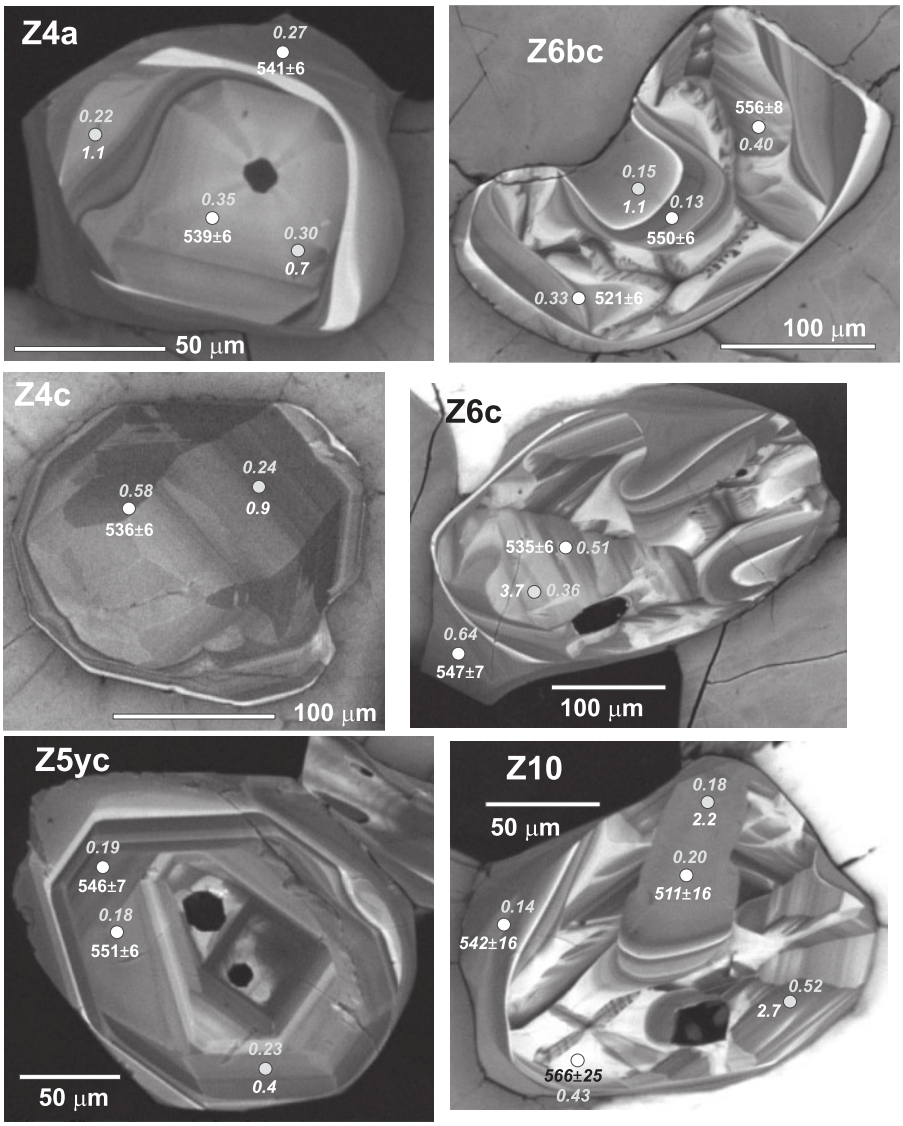


**Fig. 9.** CL images of KLP3 zircons, labelled as referred to in the text and listed in Table 4, with scale given by the horizontal scale bars. Values in white with errors attached are the $^{206}Pb/^{238}U$ ages determined at the white circled points. Grey italic numbers indicate Th/U ratio at each analysis point; white italic numbers, U/Yb ratio. White spots are those analysed for U–Pb geochronology and grey spots those analysed for REE and trace elements. (See text for discussion of textures.)

781 ±11°C for zircon crystallization and modification. Calculations at $a_{TiO2}$ of 0·8 and 0·6 yield temperatures higher by 23°C and 54°C respectively (Supplementary Data Electronic Appendix 2).

These minimum temperatures for zircon crystallization are significantly higher than the zirconium saturation temperature calculated for KLP3 based on its whole-rock Zr content (700°C). They also are lower than the minimum temperatures required for the stability of the Grt + Sil + Ilm + 2 Feldspar + Qz + melt assemblage in KLP3 from phase diagram modelling (>835°C, Fig. 6a and b), and significantly lower than the *c.* 880–930°C peak conditions inferred for the central KKB from previous metamorphic equilibria studies (e.g. Nandakumar & Harley, 2000). This result is consistent, however, with empirical and modelling studies demonstrating zircon crystallization from melts on cooling subsequent to peak metamorphism in granulite terranes (Kelsey *et al.*, 2008; Kelsey & Powell, 2011) and will be returned to in the discussion.

## Zircon U–Pb zircon geochronology

Zircon U–Pb analyses were carried out on spots adjacent to those spots analysed for REE. Correlations between Th/U and, for example, $Yb_n/Gd_n$ observed in the zircon

*Table 4: KLP3 zircon trace element compositions*

| | Trellis cores and high-HREE planar sectors | | | | | | | | | Low-HREE planar zones | | | | Disturbed trellis cores and lobate domains or overgrowths | | | | | | |
|---|---|---|---|---|---|---|---|---|---|---|---|---|---|---|---|---|---|---|---|---|
| | z2c | z4b | z5z1 | z5z2 | z5z4 | z6c | z10b | zm1 | Av. | z4a1 | z4c | z5y | Av. | z2a | z2b | z4a2 | z5z3 | z6b1 | z10a | Av. |
| *ppm* | | | | | | | | | | | | | | | | | | | | |
| Ca | 3·39 | 1·20 | 4·56 | 2·79 | 1·10 | 11·1 | 69·7 | 0·87 | 11·9 | 0·75 | 0·67 | 2·79 | 1·40 | 0·56 | 6·88 | 1·50 | 1·00 | 1·39 | 41·0 | 2·3 |
| P | 882 | 858 | 355 | 598 | 668 | 423 | 560 | 511 | 607 | 260 | 332 | 298 | 297 | 301 | 318 | 297 | 307 | 319 | 310 | 308 |
| Y | 793 | 854 | 327 | 603 | 921 | 373 | 682 | 452 | 626 | 188 | 279 | 227 | 231 | 175 | 166 | 219 | 175 | 158 | 187 | 179 |
| Ti | 13·7 | 13·0 | 11·5 | 13·0 | 12·2 | 10·6 | 11·7 | 10·8 | 12·1 | 13·2 | 12·7 | 15·2 | 13·7 | 13·6 | 12·3 | 10·5 | 10·5 | 12·3 | 14·3 | 11·8 |
| La | 0·12 | 0·12 | 0·10 | 0·08 | 0·11 | 0·08 | 0·08 | 0·06 | 0·09 | 0·03 | 0·03 | 0·01 | 0·02 | 0·02 | 0·00 | 0·04 | 0·01 | 0·03 | 0·02 | 0·0 |
| Ce | 2·57 | 4·11 | 2·56 | 2·85 | 5·00 | 2·21 | 2·83 | 1·59 | 3·0 | 1·34 | 1·51 | 0·98 | 1·28 | 1·31 | 0·67 | 0·79 | 1·03 | 1·10 | 1·05 | 1·0 |
| Pr | 0·28 | 0·41 | 0·06 | 0·20 | 0·44 | 0·21 | 0·24 | 0·07 | 0·24 | 0·06 | 0·06 | 0·15 | 0·09 | 0·06 | 0·05 | 0·03 | 0·07 | 0·01 | 0·04 | 0·0 |
| Nd | 4·17 | 6·69 | 1·05 | 2·83 | 10·5 | 2·32 | 5·13 | 2·35 | 4·4 | 1·65 | 2·53 | 2·55 | 2·25 | 1·78 | 0·97 | 2·52 | 0·88 | 0·81 | 1·31 | 1·4 |
| Sm | 9·06 | 11·9 | 3·19 | 6·09 | 15·9 | 3·23 | 10·5 | 4·10 | 8·0 | 2·14 | 5·62 | 3·78 | 3·85 | 4·15 | 3·39 | 3·87 | 2·98 | 2·52 | 4·39 | 3·4 |
| Eu | 0·16 | 0·13 | 0·03 | 0·04 | 0·32 | 0·19 | 0·12 | 0·03 | 0·13 | 0·06 | 0·07 | 0·05 | 0·06 | 0·11 | 0·04 | 0·06 | 0·05 | 0·06 | 0·03 | 0·1 |
| Gd | 42·6 | 39·9 | 12·2 | 28·0 | 57·6 | 20·3 | 42·4 | 18·6 | 32·7 | 12·4 | 25·2 | 20·7 | 19·4 | 17·3 | 14·6 | 13·6 | 14·6 | 13·7 | 14·9 | 14·7 |
| Tb | 11·4 | 10·8 | 4·0 | 7·8 | 14·3 | 4·8 | 10·7 | 5·4 | 8·6 | 3·52 | 6·29 | 4·87 | 4·89 | 3·49 | 3·51 | 4·06 | 3·55 | 3·16 | 4·23 | 3·6 |
| Dy | 99·9 | 102·8 | 33·7 | 75·7 | 125·3 | 39·9 | 91·3 | 52·4 | 77·6 | 29·6 | 46·9 | 39·9 | 38·8 | 22·8 | 27·3 | 32·9 | 25·9 | 25·5 | 29·4 | 26·9 |
| Ho | 28·6 | 28·2 | 11·1 | 20·8 | 33·2 | 11·5 | 22·5 | 15·2 | 21·4 | 5·7 | 9·7 | 7·8 | 7·73 | 5·95 | 5·25 | 6·74 | 5·34 | 5·01 | 5·87 | 5·7 |
| Er | 109·2 | 106·2 | 42·4 | 80·1 | 123·4 | 47·7 | 84·2 | 56·4 | 81·2 | 13·7 | 21·4 | 18·1 | 17·7 | 16·3 | 13·9 | 21·2 | 13·4 | 15·3 | 19·5 | 16·0 |
| Tm | 19·2 | 21·0 | 8·6 | 16·0 | 21·2 | 8·5 | 14·9 | 10·2 | 15·0 | 1·94 | 3·10 | 3·04 | 2·69 | 2·49 | 2·03 | 2·64 | 2·04 | 1·83 | 3·93 | 2·2 |
| Yb | 126·4 | 141·2 | 57·3 | 99·6 | 137·7 | 61·3 | 94·8 | 71·8 | 98·8 | 7·2 | 18·5 | 7·4 | 11·1 | 11·6 | 12·6 | 12·3 | 10·5 | 12·2 | 26·7 | 11·9 |
| Lu | 30·0 | 33·6 | 11·9 | 23·4 | 30·7 | 13·8 | 20·3 | 18·0 | 22·7 | 1·17 | 3·02 | 1·91 | 2·03 | 1·87 | 1·69 | 2·14 | 1·91 | 1·79 | 6·79 | 1·9 |
| Hf | 12570 | 11347 | 13959 | 12085 | 12390 | 12464 | 12697 | 12456 | 12496 | 13219 | 14025 | 16262 | 14502 | 12819 | 12311 | 13930 | 14023 | 11356 | 13089 | 12888 |
| Th | 159 | 191 | 66 | 149 | 272 | 66 | 190 | 84 | 147 | 66 | 98 | 87 | 84 | 129 | 63 | 55 | 58 | 53 | 84 | 72 |
| U | 347 | 396 | 172 | 252 | 350 | 184 | 362 | 200 | 283 | 220 | 402 | 371 | 331 | 746 | 520 | 251 | 518 | 356 | 463 | 478 |
| Sm/Nd | 2·2 | 1·8 | 3·0 | 2·2 | 1·5 | 1·4 | 2·0 | 1·7 | 2·0 | 1·3 | 2·2 | 1·5 | 1·7 | 2·3 | 3·5 | 1·5 | 3·4 | 3·1 | 3·3 | 2·8 |
| $HfO_2$ | 1·48 | 1·34 | 1·65 | 1·43 | 1·46 | 1·47 | 1·50 | 1·47 | 1·47 | 1·56 | 1·65 | 1·92 | 1·71 | 1·51 | 1·45 | 1·64 | 1·65 | 1·34 | 1·54 | 1·52 |
| Th/U | 0·46 | 0·48 | 0·38 | 0·59 | 0·78 | 0·36 | 0·52 | 0·42 | 0·50 | 0·30 | 0·24 | 0·23 | 0·26 | 0·17 | 0·12 | 0·22 | 0·11 | 0·15 | 0·18 | 0·2 |
| U/Yb | 2·7 | 2·8 | 3·0 | 2·5 | 2·5 | 3·0 | 3·8 | 2·8 | 2·9 | 30·5 | 21·7 | 50·1 | 34·1 | 64·1 | 41·4 | 20·3 | 49·1 | 29·2 | 17·4 | 40·8 |
| U/Y | 0·4 | 0·5 | 0·5 | 0·4 | 0·4 | 0·5 | 0·5 | 0·4 | 0·5 | 1·2 | 1·4 | 1·6 | 1·4 | 4·3 | 3·1 | 1·1 | 3·0 | 2·2 | 2·5 | 2·8 |

(continued)

*Table 4: Continued*

| | Trellis cores and high-HREE planar sectors | | | | | | | | | Low-HREE planar zones | | | | Disturbed trellis cores and lobate domains or overgrowths | | | | | | |
|---|---|---|---|---|---|---|---|---|---|---|---|---|---|---|---|---|---|---|---|---|
| | z2c | z4b | z5z1 | z5z2 | z5z4 | z6c | z10b | zm1 | Av. | z4a1 | z4c | z5y | Av. | z2a | z2b | z4a2 | z5z3 | z6b1 | z10a | Av. |
| *Chondrite-normalized REE* | | | | | | | | | | | | | | | | | | | | |
| La | 0·51 | 0·53 | 0·43 | 0·35 | 0·45 | 0·33 | 0·36 | 0·25 | 0·40 | 0·12 | 0·12 | 0·04 | 0·10 | 0·07 | 0·01 | 0·15 | 0·03 | 0·14 | 0·10 | 0·08 |
| Ce | 4·3 | 6·8 | 4·2 | 4·7 | 8·3 | 3·7 | 4·7 | 2·6 | 4·9 | 2·2 | 2·5 | 1·6 | 2·1 | 2·2 | 1·1 | 1·3 | 1·7 | 1·8 | 1·7 | 1·6 |
| Pr | 3·1 | 4·6 | 0·7 | 2·3 | 4·9 | 2·3 | 2·7 | 0·8 | 2·7 | 0·7 | 0·7 | 1·7 | 1·0 | 0·6 | 0·5 | 0·4 | 0·8 | 0·1 | 0·5 | 0·5 |
| Nd | 9·2 | 14·8 | 2·3 | 6·3 | 23·2 | 5·1 | 11·3 | 5·2 | 9·7 | 3·6 | 5·6 | 5·6 | 5·0 | 3·9 | 2·1 | 5·6 | 1·9 | 1·8 | 2·9 | 3·1 |
| Sm | 61·6 | 81·0 | 21·7 | 41·4 | 107·8 | 22·0 | 71·3 | 27·6 | 54·3 | 14·6 | 38·2 | 25·7 | 26·2 | 28·2 | 23·1 | 26·3 | 20·3 | 17·1 | 29·8 | 23·0 |
| Eu | 2·82 | 2·37 | 0·60 | 0·76 | 5·72 | 3·33 | 2·08 | 0·60 | 2·28 | 1·07 | 1·17 | 0·89 | 1·05 | 2·02 | 0·79 | 1·07 | 0·97 | 0·98 | 0·54 | 1·17 |
| Gd | 216·9 | 203·1 | 61·9 | 142·5 | 293·2 | 103·4 | 215·5 | 94·6 | 166·4 | 63·1 | 128·3 | 105·0 | 98·8 | 87·9 | 74·0 | 69·1 | 74·2 | 69·6 | 75·8 | 75·0 |
| Tb | 313·9 | 298·2 | 110·5 | 214·4 | 392·9 | 131·2 | 295·3 | 148·7 | 238·1 | 96·9 | 173·3 | 134·1 | 134·7 | 96·1 | 96·7 | 111·9 | 97·8 | 87·0 | 116·5 | 97·9 |
| Dy | 411·5 | 423·7 | 139·0 | 312·0 | 516·2 | 164·3 | 376·1 | 215·7 | 319·8 | 121·8 | 193·2 | 164·5 | 159·8 | 94·1 | 112·3 | 135·4 | 106·8 | 105·2 | 121·0 | 110·8 |
| Ho | 514·3 | 506·7 | 198·8 | 373·3 | 597·3 | 206·0 | 404·5 | 273·0 | 384·2 | 102·1 | 174·7 | 140·1 | 139·0 | 107·0 | 94·5 | 121·2 | 96·1 | 90·1 | 105·6 | 101·8 |
| Er | 687·1 | 668·3 | 267·0 | 504·2 | 776·3 | 300·1 | 529·9 | 355·0 | 511·0 | 86·1 | 134·4 | 113·6 | 111·4 | 102·3 | 87·1 | 133·2 | 84·5 | 96·0 | 122·7 | 100·6 |
| Tm | 794·1 | 868·6 | 354·9 | 662·9 | 876·9 | 349·7 | 613·9 | 423·3 | 618·0 | 80·1 | 128·2 | 125·6 | 111·3 | 103·1 | 83·9 | 109·2 | 84·3 | 75·6 | 162·2 | 91·2 |
| Yb | 777·5 | 868·7 | 352·8 | 612·7 | 847·8 | 377·0 | 583·5 | 441·5 | 607·7 | 44·4 | 114·0 | 45·6 | 68·0 | 71·6 | 77·3 | 75·9 | 64·9 | 75·0 | 164·1 | 72·9 |
| Lu | 1233·3 | 1380·7 | 490·5 | 961·1 | 1265·1 | 567·5 | 836·7 | 739·0 | 934·2 | 48·3 | 124·2 | 78·5 | 83·7 | 77·0 | 69·6 | 88·0 | 78·8 | 73·8 | 279·3 | 77·4 |
| Eu/Eu* | 0·020 | 0·017 | 0·014 | 0·008 | 0·029 | 0·053 | 0·014 | 0·010 | 0·02 | 0·028 | 0·014 | 0·014 | 0·02 | 0·035 | 0·016 | 0·022 | 0·021 | 0·023 | 0·010 | 0·02 |
| Ce/Ce* | 2·3 | 2·7 | 7·4 | 3·6 | 3·1 | 2·8 | 3·1 | 4·9 | 3·7 | 5·3 | 6·1 | 1·9 | 4·4 | 6·1 | 4·0 | 5·1 | 3·9 | 14·6 | 6·3 | 6·7 |
| $Er_n/Sm_n$ | 11·2 | 8·3 | 12·3 | 12·2 | 7·2 | 13·7 | 7·4 | 12·9 | 10·6 | 5·9 | 3·5 | 4·4 | 4·6 | 3·6 | 3·8 | 5·1 | 4·2 | 5·6 | 4·1 | 4·4 |
| $Yb_n/Gd_n$ | 3·6 | 4·3 | 5·7 | 4·3 | 2·9 | 3·6 | 2·7 | 4·7 | 4·0 | 0·7 | 0·9 | 0·4 | 0·7 | 0·8 | 1·0 | 1·1 | 0·9 | 1·1 | 2·2 | 1·2 |

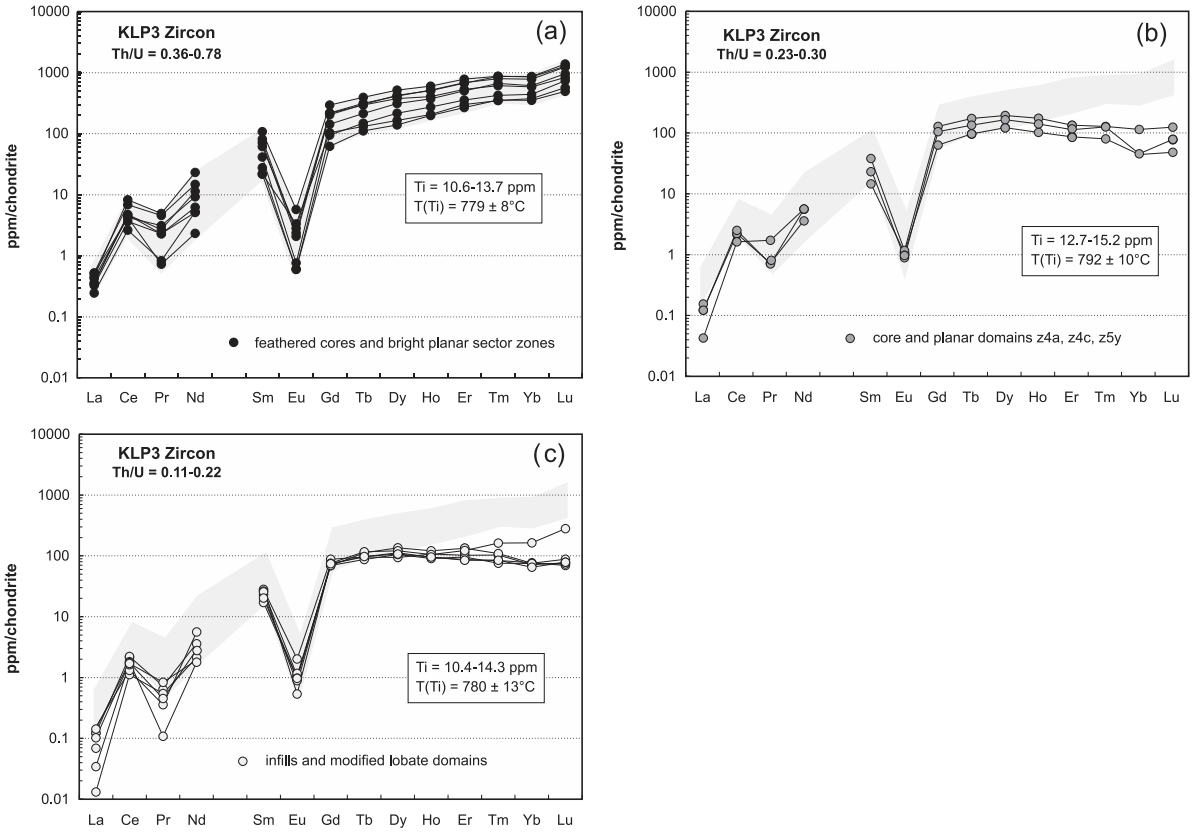


**Fig. 10.** Chondrite-normalized REE patterns for KLP3 zircons. The strong depletion in Eu (Eu/Eu* ≪ 1) in all cases should be noted. (a) Higher Th/U feathered cores and bright planar zoned zircon. (b) Core and planar domains with lower Th/U. (c) Infills and lobate zircon domains. Grey shaded field on each diagram is the range of REE compositions for the high Th/U group shown in (a). Zircon Ti contents for each group are also shown, with temperatures estimated from Ferry & Watson (2007). Chondrite values for normalization are from Anders & Grevesse (1989).

trace element dataset allows the ages of single textural domains determined in the geochronology dataset to be assigned to HREE chemistry groups. Figure 12 illustrates Th/U ratios plotted against U content for all zircon analyses, including those with corresponding $Yb_n/Gd_n$ data (the trace element zircon dataset) and those obtained for U–Pb geochronology. Collectively the data define two clear trends, and the U–Pb geochronology points lie on the trends defined by the full REE dataset. Feathered zircon cores and high-HREE planar zircons lie on a trend to higher Th/U with increasing U content, and flat-HREE zircons lie at low Th/U (<0·3) for all U contents greater than 350 ppm.

The U–Pb isotopic results are presented in Table 5 and using the Tera–Wasserburg inverse concordia diagrams of Fig. 13, and plotted in terms of $^{206}Pb/^{238}U$ ages for the three chemical–textural groups in Fig. 14. A weighted mean $^{206}Pb/^{238}U$ age of 545 ± 4·6 Ma (MSWD = 2·3) is obtained for all analyses excluding three that were deliberately collected from invasive lobes and fracture seals. The corresponding weighted mean $^{207}Pb/^{235}U$ age for these 20 analyses is 543·1 ± 4·8 Ma (MSWD = 2·5). The high MSWD values associated with these ages indicate excess scatter in the data that may reflect Pb loss along concordia as a result of an overprinting geological event; for example, at or near 515 Ma.

The U–Pb analyses have been divided into groups based on their textural type (undisturbed feathered cores, sector-planar and planar zoned zircon, lobes and infills) and Th/U ratios (Figs 13 and 14). Planar zoned zircon with high Th/U is chemically indistinct from texturally undisturbed feathered cores and so both are included in a 'higher Th/U group' that is typified by elevated $Yb_n/Gd_n$. The weighted mean $^{206}Pb/^{238}U$ age for this group is 544·2 ± 8·8 Ma (MSWD = 3·4; $n = 9$). The excess scatter indicated by the high MSWD suggests smearing of the age data along concordia owing to minor Pb loss caused by a slightly younger geological event.

Medium-CL, weakly planar zoned zircon with lower Th/U (<0·3) and low $Yb_n/Gd_n$ yields a weighted $^{206}Pb/^{238}U$ age of 550 ± 13 (MSWD = 2·5, $n = 5$), indistinguishable from the age deduced for the higher Th/U group with which the domains are texturally associated. Collectively the 14 analyses obtained on feathered cores

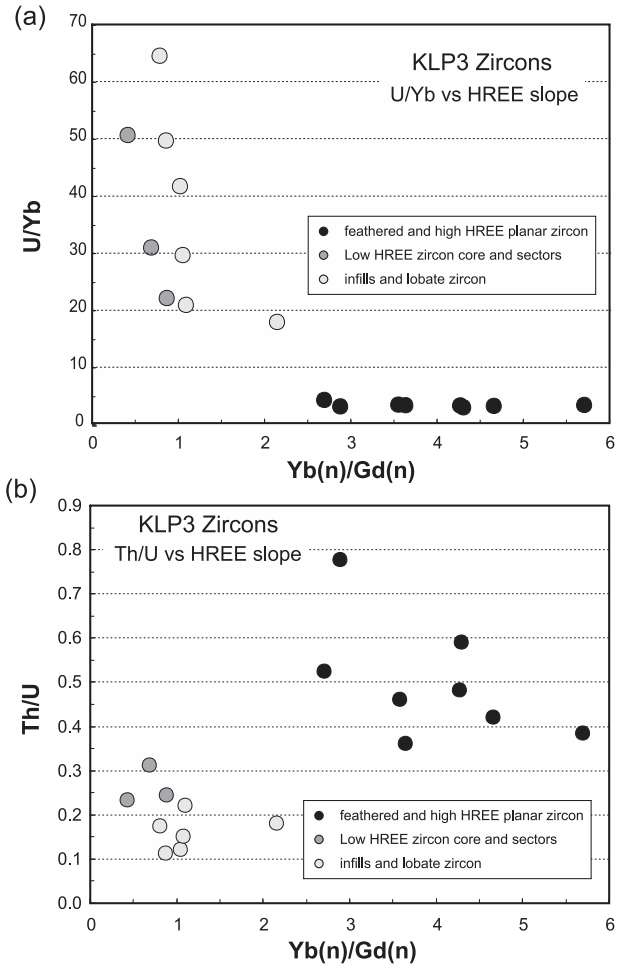


**Fig. 11.** Th–U–Yb variations in KLP3 zircons plotted against $Yb_n/Gd_n$, a measure of HREE fractionation: (a) shows the distinction between low U/Yb, high $Yb_n/Gd_n$, zircons and the low $Yb_n/Gd_n$ zircons that have variable but high U/Yb; (b) shows that this distinction is also seen in Th/U, which is lower for the low $Yb_n/Gd_n$ groups.

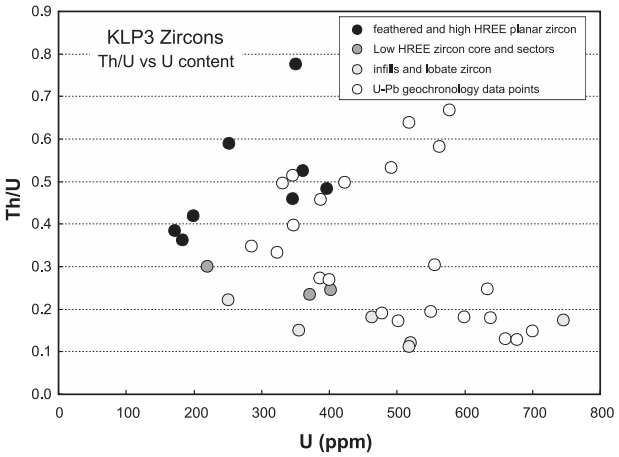


**Fig. 12.** Variation of Th/U vs U (ppm) for KLP3 zircons based on both trace element analyses (Table 4) and U–Pb geochronological analyses (Table 5). The two distinct trends in Th/U that can be correlated with zircon microtexture should be noted.

and planar zoned zircon of both high Th/U and lower Th/U types yield a weighted average $^{206}Pb/^{238}U$ age of 546·1 ±6·4 Ma (MSWD = 3, $n$ = 14). Again, the excess scatter indicated by the slightly high MSWD suggests smearing of the age data along concordia owing to minor Pb loss caused by a slightly younger geological event.

Lobate domains and rims, and disturbed cores with elliptical infills, which also have low Th/U and $Yb_n/Gd_n$, are distinguished as a separate group on the basis of their textural differences from the weakly zoned planar zircon domains. Six analyses of lobate domains and infills form a tight analytical cluster on concordia and have a weighted average $^{206}Pb/^{238}U$ age of 541·9 ± 5·5 Ma (MSWD = 0·56). This age for the initial modification of zircon to produce invasive lobes, elliptical infills and disturbed cores with lowered Th/U (and low $Yb_n/Gd_n$) overlaps with the 546·1 ±6·4 Ma age deduced above for the feathered cores and planar zoned zircon of both high Th/U and lower Th/U types.

Two zircon lobe (Z15a, Z2a4) and one highly disturbed feathered–infill zircon (Z6b3) yield significantly younger $^{206}Pb/^{238}U$ ages that range from *c.* 520 to 503 Ma. These ages overlap with those of the high-Th monazite rims described in a subsequent section (514·2 ± 6·8 Ma).

Single zircon grains analysed at several sites provide more detail on the $^{206}Pb/^{238}U$ ages in relation to zircon texture. Examples of this are illustrated in Figs 8 and 9, where $^{206}Pb/^{238}U$ ages are noted along with Th/U ratios for the analysis sites and the textural types (feathered cores, planar-zoned, elliptical infills, cuspate–invasive lobes) can be clearly distinguished. Collectively these data suggest that most zircon growth, including the high Th/U (high-HREE) and lower Th/U (flat-HREE) cores and planar zones, occurred at 546·1 ±6·4 Ma. Infills and lobate zircon replacement domains developed from 542 ± 6 Ma, prior to later (520–505 Ma) zircon modification leading to the youngest invasive lobate zircon domains.

## MONAZITE IN LEUCOGRANITE KLP3

### Monazite petrography and microtextures

Monazites occur in two principal textural associations: (1) as subhedral and weakly planar-sector zoned grains included in garnet; (2) as irregular, rounded and elongate coarse grains (200–400 μm diameter) in close association with ilmenite and clusters of zircon, set in leucosomal layers dominated by plagioclase, perthitic K-feldspar and quartz. In the latter association monazite may be present as single grains, grains that share granoblastic boundaries

*Table 5: Zircon isotopic data: Kulappara sample KLP3, Kerala Khondalite Belt*

| Grain, spot | Type | Concentration | | | | | | | Isotopic ratio | | | | | | | Apparent age (Ma) | | | | | |
|---|---|---|---|---|---|---|---|---|---|---|---|---|---|---|---|---|---|---|---|---|---|
| | | U (ppm) | Th (ppm) | Th/U | Pb (ppm) | $^{204}$Pb (ppb) | $^{206}$Pb/$^{204}$Pb | *f*206 (%) | $^{207}$Pb/$^{235}$U | ± | $^{206}$Pb/$^{238}$U | ± | $^{207}$Pb/$^{206}$Pb | ± | % conc. | $^{206}$Pb/$^{238}$U | ± | $^{207}$Pb/$^{235}$U | ± | $^{207}$Pb/$^{206}$Pb | ± |
| z1 | outer planar | 330·9 | 164·0 | 0·496 | 29·8 | 1·48 | 16602 | 0·11 | 0·6814 | 0·0103 | 0·0857 | 0·0009 | 0·0577 | 0·0006 | 2·5 | 530·0 | 5·2 | 527·6 | 6·2 | 517·0 | 24 |
| z2a1 | planar | 423·3 | 210·8 | 0·498 | 39·8 | 1·38 | 23676 | 0·08 | 0·7092 | 0·0100 | 0·0893 | 0·0010 | 0·0576 | 0·0005 | 7·0 | 551·2 | 6·2 | 544·2 | 5·9 | 515·0 | 17 |
| z2a2 | trellis, dist. | 386·8 | 105·2 | 0·272 | 33·6 | 2·99 | 9836 | 0·19 | 0·7009 | 0·0260 | 0·0878 | 0·0030 | 0·0579 | 0·0008 | 3·4 | 542·7 | 17·9 | 539·4 | 15·4 | 525·0 | 29 |
| z2a3 | trellis, dist. | 388·0 | 177·7 | 0·458 | 35·1 | 1·19 | 24427 | 0·08 | 0·6945 | 0·0108 | 0·0868 | 0·0011 | 0·0580 | 0·0005 | 1·3 | 536·6 | 6·6 | 535·5 | 6·5 | 530·0 | 20 |
| z2a4 | lobe | 556·4 | 168·9 | 0·304 | 45·1 | 1·38 | 28341 | 0·07 | 0·6481 | 0·0075 | 0·0812 | 0·0008 | 0·0579 | 0·0003 | –4·1 | 503·3 | 5·0 | 507·3 | 4·6 | 525·0 | 12 |
| z4ac1a | trellis | 285·7 | 99·3 | 0·348 | 25·2 | 2·01 | 10696 | 0·17 | 0·6889 | 0·0121 | 0·0871 | 0·0011 | 0·0573 | 0·0007 | 6·9 | 538·6 | 6·3 | 532·2 | 7·3 | 504·0 | 28 |
| z4ac2 | outer og | 399·6 | 107·7 | 0·270 | 34·6 | 1·77 | 17071 | 0·11 | 0·6955 | 0·0102 | 0·0876 | 0·0011 | 0·0576 | 0·0005 | 5·3 | 541·1 | 6·3 | 536·1 | 6·1 | 514·0 | 19 |
| z4c1 | planar | 562·3 | 326·6 | 0·581 | 52·5 | 0·50 | 85008 | 0·02 | 0·6939 | 0·0099 | 0·0868 | 0·0010 | 0·0580 | 0·0005 | 1·4 | 536·4 | 5·9 | 535·2 | 5·9 | 529·0 | 19 |
| z5x1 | planar core | 633·7 | 156·8 | 0·247 | 54·4 | 1·58 | 30323 | 0·06 | 0·7002 | 0·0097 | 0·0872 | 0·0010 | 0·0582 | 0·0005 | 0·2 | 538·9 | 5·8 | 538·9 | 5·8 | 538·0 | 18 |
| z5y1 | planar | 599·7 | 108·3 | 0·181 | 51·7 | 5·51 | 8402 | 0·22 | 0·7219 | 0·0116 | 0·0892 | 0·0010 | 0·0587 | 0·0007 | –0·7 | 550·9 | 6·1 | 551·8 | 6·8 | 555·0 | 24 |
| z5y2 | planar | 478·4 | 90·6 | 0·189 | 41·0 | 2·64 | 13849 | 0·13 | 0·7248 | 0·0119 | 0·0884 | 0·0013 | 0·0595 | 0·0005 | –6·3 | 546·1 | 7·4 | 553·5 | 7·0 | 583·0 | 18 |
| z5z1a | infill | 502·3 | 86·6 | 0·172 | 42·1 | 0·66 | 57129 | 0·03 | 0·7054 | 0·0095 | 0·0870 | 0·0010 | 0·0588 | 0·0004 | –4·0 | 537·5 | 6·1 | 542·0 | 5·6 | 560·0 | 14 |
| z5z2a | planar | 577·6 | 386·1 | 0·668 | 56·9 | 2·71 | 16524 | 0·11 | 0·7101 | 0·0097 | 0·0896 | 0·0010 | 0·0575 | 0·0005 | 8·2 | 552·9 | 5·9 | 544·8 | 5·7 | 511·0 | 17 |
| z5z3a | trellis | 492·2 | 262·3 | 0·533 | 47·9 | 1·82 | 21365 | 0·09 | 0·7592 | 0·0130 | 0·0915 | 0·0012 | 0·0602 | 0·0007 | –7·5 | 564·3 | 6·8 | 573·6 | 7·5 | 610·0 | 25 |
| z5z5 | lobe | 677·4 | 87·3 | 0·129 | 56·7 | 1·35 | 38092 | 0·05 | 0·7145 | 0·0100 | 0·0880 | 0·0011 | 0·0589 | 0·0004 | –3·4 | 543·7 | 6·3 | 547·4 | 5·9 | 563·0 | 15 |
| z6b1 | lobe | 660·6 | 85·6 | 0·130 | 55·9 | 1·82 | 28032 | 0·07 | 0·7072 | 0·0101 | 0·0890 | 0·0011 | 0·0576 | 0·0004 | 7·0 | 549·9 | 6·4 | 543·1 | 6·0 | 514·0 | 16 |
| z6b2 | planar | 347·7 | 138·3 | 0·398 | 32·1 | 2·73 | 9914 | 0·19 | 0·7046 | 0·0126 | 0·0900 | 0·0014 | 0·0568 | 0·0005 | 15·3 | 555·6 | 8·4 | 541·5 | 7·5 | 482·0 | 18 |
| z6b3 | trellis, dist. | 322·8 | 107·2 | 0·332 | 27·3 | 1·29 | 18172 | 0·10 | 0·6649 | 0·0127 | 0·0841 | 0·0010 | 0·0573 | 0·0009 | 3·3 | 520·6 | 6·1 | 517·6 | 7·7 | 504·0 | 32 |
| z6c | planar | 345·9 | 177·9 | 0·514 | 31·6 | 1·55 | 16653 | 0·11 | 0·6878 | 0·0110 | 0·0865 | 0·0011 | 0·0577 | 0·0006 | 3·4 | 534·6 | 6·3 | 531·5 | 6·6 | 517·0 | 22 |
| zm6a2 | outer og | 518·3 | 330·8 | 0·638 | 50·1 | 1·57 | 25299 | 0·07 | 0·7094 | 0·0103 | 0·0886 | 0·0012 | 0·0581 | 0·0003 | 3·1 | 547·3 | 6·9 | 544·4 | 6·1 | 531·0 | 14 |
| z15a | lobe | 700·6 | 103·4 | 0·148 | 55·3 | 2·61 | 19220 | 0·10 | 0·6481 | 0·0086 | 0·0826 | 0·0009 | 0·0569 | 0·0005 | 5·1 | 511·8 | 5·1 | 507·3 | 5·3 | 487·0 | 17 |
| z15b | planar | 549·8 | 106·1 | 0·193 | 49·2 | 0·73 | 60158 | 0·03 | 0·7469 | 0·0132 | 0·0923 | 0·0014 | 0·0587 | 0·0005 | 2·3 | 568·9 | 8·5 | 566·4 | 7·6 | 556·0 | 18 |
| z15c | planar | 638·1 | 113·9 | 0·179 | 55·4 | 1·35 | 36736 | 0·05 | 0·7131 | 0·0114 | 0·0901 | 0·0011 | 0·0574 | 0·0006 | 9·9 | 556·2 | 6·6 | 546·6 | 6·8 | 506·0 | 23 |

*f*206, %$^{206}$Pb associated with common Pb; dist., disturbed zoning; og, overgrowth.

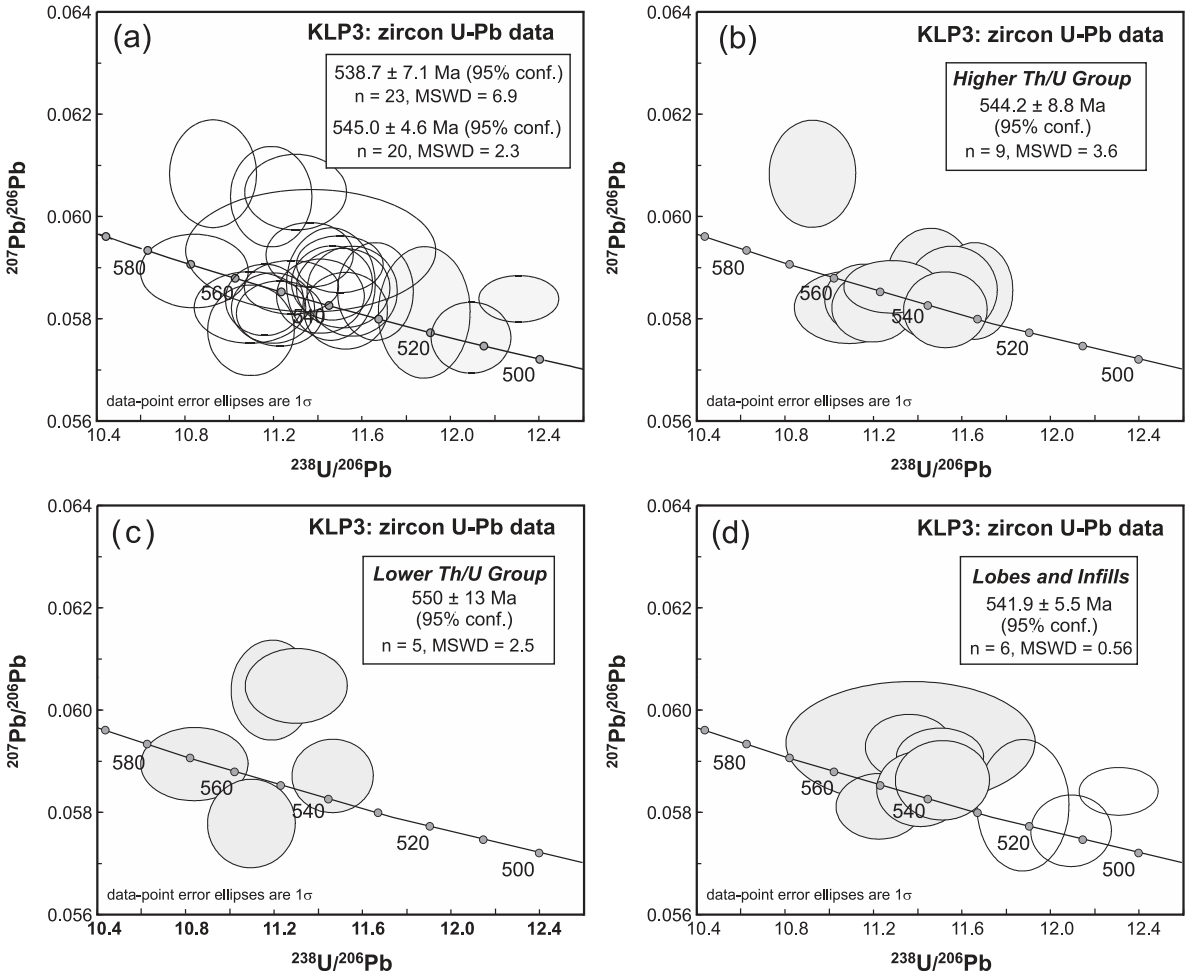


**Fig. 13.** U–Pb geochronological data for KLP3 zircons, presented as $^{204}$Pb-corrected Tera–Wasserburg concordia diagrams ($^{207}$Pb/$^{206}$Pb vs $^{238}$U/$^{206}$Pb), with data ellipses corresponding to 1σ analytical uncertainties. (a) All zircons, with weighted mean $^{206}$Pb/$^{238}$U age based on all 23 analyses and on 20 analyses that exclude the youngest, invasive lobate domains. (b–d) Analyses for the three zircon groups defined from texture and Th/U: (b) high Th/U, complex cores and planar zircon; (c) lower Th/U, planar zircon; (d) lobate and infill zircon.

with zircon or ilmenite, or grains partially included within ilmenite that also includes or partially encloses zircon. Monazite–zircon textures include those in which monazite appears to overgrow or enclose zircon, zircon overgrows monazite, and in which zircon and monazite share planar to curviplanar boundaries. These features suggest contemporaneous formation or recrystallization of at least the outer (rimward) parts of zircon and monazite.

BSE imaging shows that monazites of textural association (2) exhibit variety in their 'core' internal chemical zoning features, including planar-sector zoning (Mnz5, Mnz10) and irregular cuspate–lobate zoning with darker and lighter BSE domains showing mutual apparent replacement–truncation relationships (Mnz1, Mnz6, Mnz6a). Both styles of internal zoning are truncated by bright curviplanar rim domains that parallel grain boundaries and appear to replace the 'core' chemical zones (Fig. 15).

## Monazite chemistry

Monazite microanalysis was preceded by detailed SEM imaging using secondary and back-scattered electrons (BSE: 20 kV and 5 nA). Selected examples of monazite textural relationships and internal structures that reflect chemical variations are provided in Fig. 15. Monazite mineral chemistry (Table 6; Supplementary Data Electronic Appendix 3) is described below within the context provided by the imaging, followed by presentation of the electron microprobe chemical age data.

Monazites are highly variable in their Th + U + Si and REE chemistry, describing a wide range on the monazite–brabantite–huttonite diagram (Fig. 16a: Th + U + Si 0·4–0·9). $ThO_2$ varies between 7·8 and 16 wt %, broadly correlating with $UO_2$, which ranges from 0·05 to 0·33 wt %. As a result, Th/U is relatively low (35–145) in comparison with many published monazites. REE patterns are characterized by very strong but variable HREE

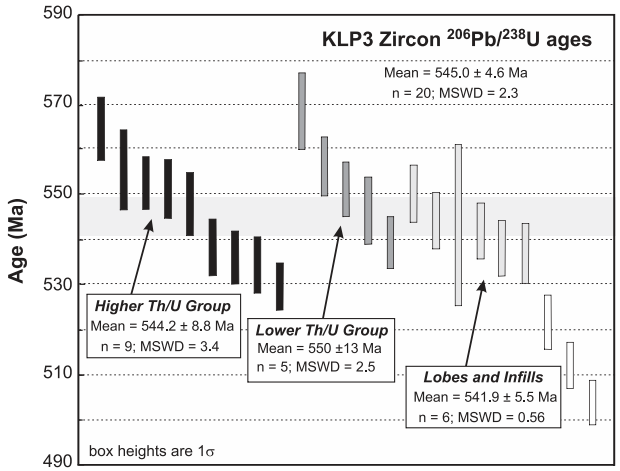


**Fig. 14.** Weighted $^{206}Pb/^{238}U$ age data for the three zircon types distinguished on textural and Th/U grounds. Lobate and infill zircon weighted mean age is based on six of the nine analyses on these domains, and excludes the three youngest ages that are from invasive lobes.

depletions compared with LREE ($Dy_n = 5500–800$; $Ce_n/Y_n = 300–550$; Fig. 16b). $Y_2O_3$ is correspondingly low (0·14–0·26 wt %) and inversely correlated with $ThO_2$ (Table 6; Supplementary Data Electronic Appendix 3).

The systematic variations in Th + U (and Ca + Si) versus total REE define two distinct analytical populations in terms of major element chemistry, corresponding to the observed monazite microtextures, as follows.

(1) The sector-planar zoned monazites (Mnz2, Mnz5) and cuspate–irregular zoned grains (Mnzl, Mnz-6, Mnz-6 x) have $ThO_2$ in the range 8–12 wt %, $UO_2$ 0·04–0·25 wt %, the full range in Th/U, and $Ce_n/Y_n$ mostly in the range 320–450 (Fig. 17a). $La_n/Sm_n$ is highly variable, from more than 11 to less than five (Fig. 17b). This group forms a coherent trend in terms of Th + U vs REE + Y (Fig. 8a), with a huttonite:brabantite ratio near 0·33.

(2) Bright BSE rim domains have high $ThO_2$ (12–16 wt %), $Ce_n/Y_n$ greater than 400 (Fig. 17a) and $Y_2O_3$ less than 0·19 wt %. $UO_2$ clusters in the range 0·2–0·33 wt %, leading to Th/U of less than 100. These high-Th rims are relatively depleted in Y and HREE compared with the lower $ThO_2$ group (1). $La_n/Sm_n$ is consistently low (five or less: Fig. 17b), and the huttonite:brabantite ratio is near 0·5 (Fig. 16a).

To summarize, the key chemical differences between the main phase monazite and high-Th rinds or rims are that the latter have higher U contents, higher Si/Ca, and greater fractionation of LREE relative to HREE and Y, but lower La/Sm and more restricted and low Th/U.

## Monazite geochronology

### *Monazite chemical ages*

Monazite chemical age data are presented in Table 6. The group of 56 analyses taken as a whole produce a skewed age distribution with a peak at 530 Ma and 95% confidence limit age spread of ±16 Ma. Treatment of the data in the light of the textural and chemical information outlined above yields the two weighted mean age distributions shown in Fig. 18. Thirty-five analyses of the planar and irregularly zoned monazite group yield a weighted mean age of 536 ± 6 Ma (MSWD = 0·22; Fig. 18a), whereas 21 analyses of high-$ThO_2$ rims yield 514 ± 7 Ma (MSWD = 0·27; Fig. 18b). This distinction is supported by age plots of the two monazite textural–chemical groups against chemical variables such as $ThO_2$, $UO_2$, $Y_2O_3$ and $Ce_n/Y_n$ (Fig. 19a–d). Four analyses of the only monazite that occurs enclosed in garnet, Mnz2, yielded a weighted mean age of 529 ± 19 Ma (MSWD = 0·28) for the undisturbed planar-zoned domains in this monazite.

### *Monazite Th–Pb and U–Pb isotopic ages*

U–Pb and Th–Pb isotopic data on KLP3 monazites are reported in Table 7 and presented in Fig. 20. Twenty-three analyses were obtained on four grains, three of which were previously analysed by EMPA (Mnzl, Mnz6, Mnz6a). Variably structured monazite cores (group 1) range up to 11·5 wt % $ThO_2$ and bright BSE rims generally have >10·4 wt % $ThO_2$ based on an averaged Moacyr $ThO_2$ content of 6·9 wt %. Sixteen concordant core analyses yielded a weighted mean $^{206}Pb/^{238}U$ age of 535 ± 2·7 Ma (MSWD = 0·85) and a corresponding $^{208}Pb/^{232}Th$ age of 532 ± 5·4 Ma (MSWD = 0·45). Seven analyses of high-$ThO_2$ rims and irregular outer margins yielded a weighted mean $^{206}Pb/^{238}U$ age of 513·1 ± 3·9 Ma (MSWD = 0·44) and a corresponding $^{208}Pb/^{232}Th$ age of 511·4 ± 8·1 Ma (MSWD = 0·45). Taking the inherent uncertainty of 1% in the precision of the age for the Moacyr standard into account, the uncertainties on the weighted mean $^{206}Pb/^{238}U$ ages for the two chemically distinct monazite populations are expanded to ±6 Ma for further comparisons of the ages of monazite crystallization and modification with those of zircon.

The close correspondence between the weighted mean ages obtained for the two chemically distinct monazite groups using EMPA chemical dating and SIMS isotopic dating confirms the utility and robustness of the EMPA dating method in this instance. The principal population of chemically heterogeneous and variably zoned monazite crystallized or was modified in the leucosome layers of KLP3 at 535 ± 6 Ma. Substantial chemical modification of monazite, including the production of high-Th and lower-Y rims and rinds adjacent to zircon and opaque minerals, proceeded at 514 ± 6 Ma.

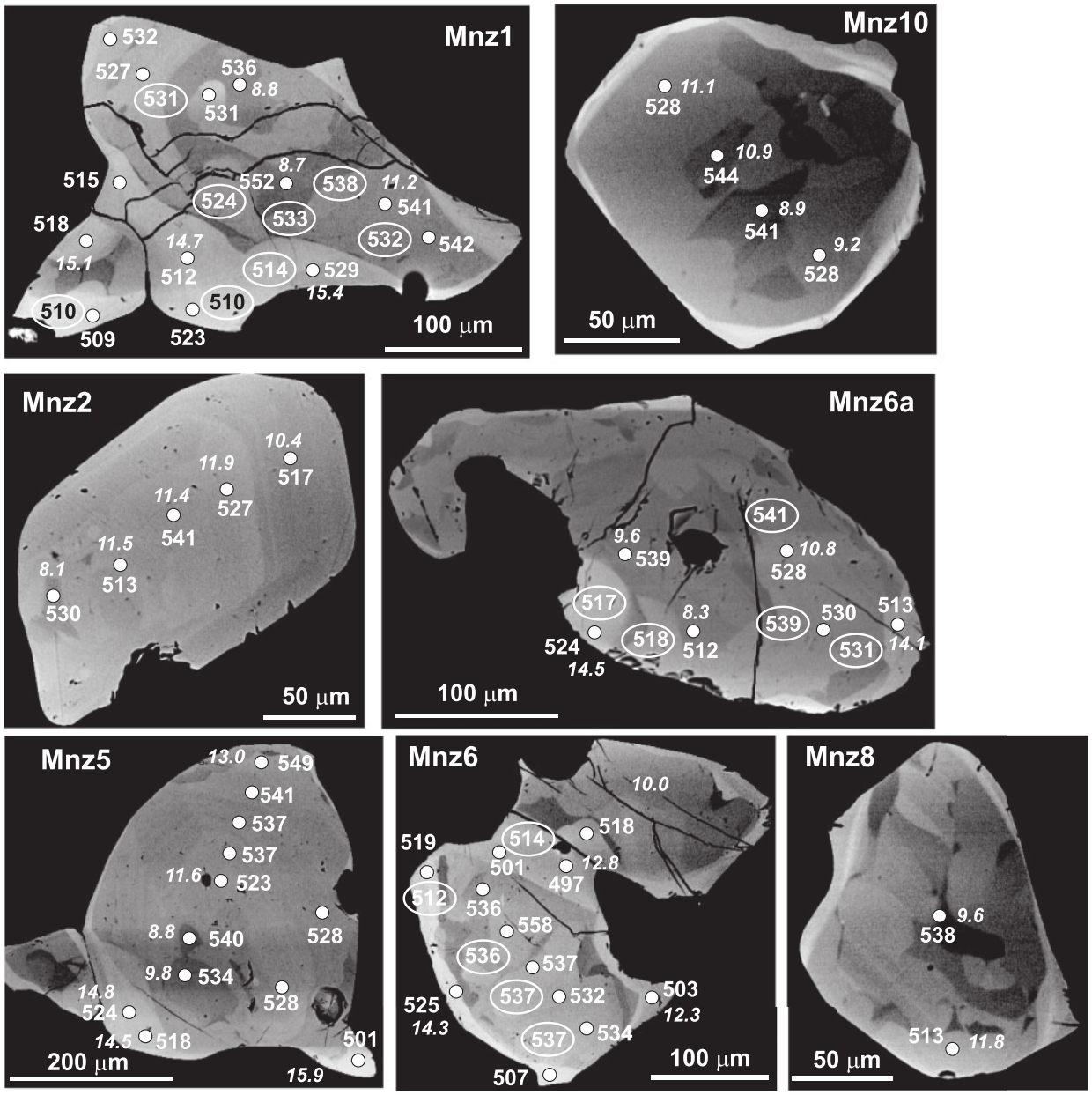


**Fig. 15.** Back-scattered electron (BSE) images of monazites in KLP3. Scales shown by horizontal bars (in microns). Monazite labels are as used in the text; analyses for each are provided in Table 6 and Supplementary Data Electronic Appendix 3. Three-digit labels (e.g. 539) are the Th–U–Pb chemical age for each analysis point (typical errors ± 13–18 Ma); the label with decimal point (e.g. 11·6) is the measured $ThO_2$ content at that point.

## GEOCHEMICAL RELATIONSHIPS AND MELT-RELATED PROCESSES AT KULAPPARA

### Zircon–garnet REE distributions and relative timing of zircon crystallization

Apparent (measured) distribution of MREE–HREE between zircon and garnet, $D_{REE}$(Zrc/Grt), is plotted for KLP3 in Fig. 21. These $D_{REE}$(Zrc/Grt) values are listed in Supplementary Data Electronic Appendix 4. Zircons have been divided according to the three groups defined above, and the $D_{REE}$(Zrc/Grt) for each group calculated by dividing the average content of each REE by that of the same REE in the KLP3 garnet. Alternative estimates of equilibrium $D_{REE}$(Zrc/Grt) based on experimental (Rubatto & Hermann, 2007) and combined experimental–empirical (Harley *et al.*, 2007) data, applicable at 800–1000°C, are shown as shaded fields for comparison with the KLP3 results.

*Table 6: KLP3 monazite chemistry and ages*

| Spot | Location | Oxide | | | | | | | | | | | | | | Age (Ma) | Error |
|---|---|---|---|---|---|---|---|---|---|---|---|---|---|---|---|---|---|
| | | $P_2O_5$ | $SiO_2$ | $La_2O_3$ | $Ce_2O_3$ | $Pr_2O_3$ | $Nd_2O_3$ | $Sm_2O_3$ | $Gd_2O_3$ | $Dy_2O_3$ | $Y_2O_3$ | $UO_2$ | $ThO_2$ | PbO | CaO | Total | | |
| KUL3__M1__1 | core | 30·26 | 0·87 | 15·20 | 29·30 | 3·20 | 10·69 | 1·09 | n.a. | 0·12 | 0·22 | 0·071 | 8·72 | 0·213 | 1·02 | 101·0 | 552 | 22 |
| KUL3__M1__2 | core | 29·49 | 1·08 | 12·40 | 27·53 | 3·25 | 12·12 | 1·41 | n.a. | 0·09 | 0·19 | 0·191 | 11·23 | 0·275 | 1·31 | 100·6 | 541 | 18 |
| KUL3__M1__3 | core | 29·25 | 1·13 | 12·19 | 27·22 | 3·22 | 11·72 | 1·51 | n.a. | 0·10 | 0·19 | 0·227 | 11·53 | 0·286 | 1·37 | 99·9 | 542 | 18 |
| KUL3__M1__4 | near rim | 27·54 | 2·03 | 11·14 | 25·81 | 3·12 | 11·84 | 1·42 | n.a. | 0·11 | 0·16 | 0·217 | 15·41 | 0·365 | 1·26 | 100·4 | 529 | 15 |
| KUL3__M1__5 | rim | 27·87 | 1·88 | 11·27 | 26·31 | 3·19 | 12·25 | 1·40 | n.a. | 0·08 | 0·16 | 0·256 | 14·22 | 0·337 | 1·18 | 100·4 | 523 | 15 |
| KUL3__M1__6 | near rim | 27·70 | 1·91 | 11·31 | 26·43 | 3·16 | 12·30 | 1·52 | n.a. | 0·04 | 0·14 | 0·243 | 14·72 | 0·340 | 1·17 | 101·0 | 512 | 15 |
| KUL3__M1__7 | core | 27·71 | 1·94 | 11·30 | 26·28 | 3·15 | 11·77 | 1·52 | n.a. | 0·07 | 0·15 | 0·205 | 14·79 | 0·352 | 1·23 | 100·5 | 531 | 15 |
| KUL3__M1__8 | core | 29·68 | 0·87 | 15·70 | 29·74 | 3·07 | 10·15 | 1·01 | n.a. | 0·12 | 0·23 | 0·063 | 8·79 | 0·208 | 0·98 | 100·6 | 536 | 22 |
| KUL3__M1__9 | core towards rim | 29·04 | 1·33 | 12·34 | 28·09 | 3·25 | 12·00 | 1·42 | n.a. | 0·12 | 0·17 | 0·149 | 11·73 | 0·276 | 1·18 | 101·1 | 527 | 18 |
| KUL3__M1__10 | near rim | 29·23 | 1·05 | 12·22 | 27·46 | 3·16 | 12·18 | 1·55 | n.a. | 0·09 | 0·18 | 0·267 | 11·34 | 0·279 | 1·42 | 100·4 | 532 | 18 |
| KUL3__M1__11 | core next grain | 29·48 | 1·08 | 12·68 | 28·20 | 3·17 | 11·30 | 1·46 | n.a. | 0·09 | 0·18 | 0·203 | 10·93 | 0·270 | 1·31 | 100·3 | 543 | 18 |
| KUL3__M1__12 | core next grain | 29·89 | 0·85 | 15·31 | 29·55 | 3·03 | 10·73 | 1·04 | n.a. | 0·10 | 0·24 | 0·066 | 8·90 | 0·221 | 1·06 | 101·0 | 563 | 22 |
| kul3__m1__13 | rim | 28·12 | 1·71 | 11·40 | 26·35 | 3·10 | 11·83 | 1·50 | n.a. | 0·07 | 0·15 | 0·205 | 14·58 | 0·330 | 1·22 | 100·6 | 509 | 15 |
| kul3__m1__14 | rim | 27·79 | 1·86 | 11·20 | 25·79 | 3·16 | 12·38 | 1·52 | n.a. | 0·12 | 0·16 | 0·235 | 15·08 | 0·349 | 1·21 | 100·9 | 518 | 15 |
| kul3__m1__15 | rim | 28·20 | 1·76 | 11·30 | 26·23 | 3·22 | 12·26 | 1·56 | n.a. | 0·03 | 0·16 | 0·308 | 14·23 | 0·334 | 1·17 | 100·8 | 515 | 15 |
| KUL3__M2__1 | core | 29·29 | 1·16 | 12·68 | 28·00 | 3·13 | 11·33 | 1·34 | n.a. | 0·06 | 0·17 | 0·202 | 11·41 | 0·280 | 1·35 | 100·4 | 541 | 18 |
| KUL3__M2__2 | core | 29·28 | 1·18 | 12·43 | 27·57 | 3·22 | 11·29 | 1·42 | n.a. | 0·10 | 0·18 | 0·254 | 11·92 | 0·288 | 1·41 | 100·5 | 527 | 17 |
| KUL3__M2__3 | nearer rim | 29·50 | 1·04 | 12·64 | 28·53 | 3·21 | 12·15 | 1·49 | n.a. | 0·09 | 0·21 | 0·133 | 10·36 | 0·240 | 1·18 | 100·8 | 517 | 19 |
| KUL3__M2__4 | disturbed near rim | 29·41 | 1·13 | 12·48 | 28·04 | 3·21 | 11·48 | 1·43 | n.a. | 0·11 | 0·17 | 0·228 | 11·48 | 0·269 | 1·34 | 100·8 | 513 | 18 |
| KUL3__M2__5 | rim | 29·91 | 0·82 | 16·81 | 30·24 | 2·76 | 9·54 | 0·93 | n.a. | 0·10 | 0·24 | 0·069 | 8·05 | 0·189 | 0·92 | 100·6 | 530 | 23 |
| KUL3__M5__1 | near rim | 28·68 | 1·54 | 11·75 | 26·26 | 3·19 | 11·93 | 1·52 | n.a. | 0·06 | 0·16 | 0·213 | 13·00 | 0·322 | 1·33 | 100·0 | 549 | 16 |
| KUL3__M5__2 | core | 28·97 | 1·24 | 11·96 | 27·14 | 3·15 | 11·90 | 1·50 | n.a. | 0·06 | 0·18 | 0·282 | 12·21 | 0·305 | 1·42 | 100·3 | 541 | 17 |
| KUL3__M5__3 | core | 29·19 | 1·21 | 12·32 | 27·55 | 3·13 | 11·74 | 1·42 | n.a. | 0·11 | 0·18 | 0·195 | 11·64 | 0·283 | 1·26 | 100·2 | 537 | 17 |
| KUL3__M5__4 | core | 29·51 | 1·08 | 12·49 | 27·13 | 3·07 | 11·77 | 1·54 | n.a. | 0·07 | 0·21 | 0·334 | 11·76 | 0·296 | 1·50 | 100·7 | 537 | 17 |
| KUL3__M5__5 | core, near inclusion | 28·71 | 1·32 | 12·36 | 27·72 | 3·29 | 12·01 | 1·54 | n.a. | 0·11 | 0·15 | 0·144 | 11·58 | 0·270 | 1·18 | 100·4 | 523 | 18 |
| KUL3__M5__6 | core | 29·75 | 0·86 | 16·27 | 29·63 | 2·97 | 9·91 | 0·96 | n.a. | 0·06 | 0·23 | 0·048 | 8·81 | 0·209 | 1·01 | 100·7 | 540 | 22 |
| KUL3__M5__7 | core | 29·86 | 0·82 | 13·11 | 28·54 | 3·33 | 12·08 | 1·40 | n.a. | 0·04 | 0·15 | 0·111 | 9·77 | 0·233 | 1·24 | 100·7 | 534 | 20 |
| KUL3__M5__8 | bright near-rim | 27·95 | 1·86 | 11·30 | 26·24 | 3·15 | 12·22 | 1·51 | n.a. | 0·07 | 0·16 | 0·225 | 14·75 | 0·348 | 1·24 | 101·0 | 524 | 15 |
| KUL3__M5__9 | bright rim | 27·84 | 1·81 | 11·24 | 26·27 | 3·24 | 12·34 | 1·42 | n.a. | 0·06 | 0·17 | 0·244 | 14·54 | 0·340 | 1·26 | 100·8 | 518 | 15 |
| KUL3__M5__10 | core outer | 28·74 | 1·45 | 12·24 | 27·98 | 3·18 | 11·55 | 1·25 | n.a. | 0·08 | 0·15 | 0·120 | 12·27 | 0·287 | 1·11 | 100·4 | 528 | 17 |

(continued)

*Table 6: Continued*

| Spot | Location | Oxide | | | | | | | | | | | | | | Age (Ma) | Error |
|---|---|---|---|---|---|---|---|---|---|---|---|---|---|---|---|---|---|
| | | $P_2O_5$ | $SiO_2$ | $La_2O_3$ | $Ce_2O_3$ | $Pr_2O_3$ | $Nd_2O_3$ | $Sm_2O_3$ | $Gd_2O_3$ | $Dy_2O_3$ | $Y_2O_3$ | $UO_2$ | $ThO_2$ | PbO | CaO | Total | | |
| KUL3__M5__11 | right on bright rim | 27·68 | 2·06 | 11·09 | 25·43 | 3·10 | 11·83 | 1·52 | n.a. | 0·11 | 0·15 | 0·198 | 15·92 | 0·355 | 1·25 | 100·7 | 501 | 14 |
| KUL3__M5__12 | core | 29·41 | 1·08 | 12·38 | 26·90 | 3·04 | 11·47 | 1·48 | n.a. | 0·09 | 0·20 | 0·304 | 12·09 | 0·297 | 1·46 | 100·2 | 528 | 17 |
| kul3__m6__1 | core | 29·89 | 0·83 | 14·90 | 29·22 | 3·15 | 10·40 | 1·15 | n.a. | 0·09 | 0·26 | 0·087 | 9·60 | 0·227 | 1·13 | 100·9 | 539 | 20 |
| kul3__m6__2 | brighter cuspate near rim | 27·99 | 1·72 | 11·54 | 26·37 | 3·11 | 11·58 | 1·54 | n.a. | 0·02 | 0·15 | 0·202 | 14·46 | 0·337 | 1·23 | 100·3 | 524 | 15 |
| kul3__m6__3 | darker core | 29·80 | 0·71 | 15·22 | 29·87 | 3·14 | 10·68 | 1·16 | n.a. | 0·10 | 0·23 | 0·084 | 8·26 | 0·186 | 0·97 | 100·4 | 512 | 23 |
| kul3__m6__4 | core | 29·57 | 0·96 | 12·49 | 27·53 | 3·19 | 11·67 | 1·46 | n.a. | 0·14 | 0·19 | 0·261 | 11·64 | 0·282 | 1·42 | 100·8 | 530 | 17 |
| kul3__m6__5 | brighter rim | 27·92 | 1·68 | 11·26 | 26·24 | 3·21 | 12·48 | 1·60 | n.a. | 0·09 | 0·17 | 0·333 | 14·05 | 0·330 | 1·19 | 100·5 | 513 | 15 |
| kul3__m6__6 | core | 29·65 | 0·78 | 12·49 | 27·63 | 3·11 | 11·18 | 1·58 | n.a. | 0·08 | 0·19 | 0·323 | 10·81 | 0·267 | 1·49 | 99·6 | 528 | 18 |
| kul3__m6x__1 | edge near rim | 28·50 | 1·45 | 11·93 | 27·29 | 3·23 | 12·41 | 1·54 | n.a. | 0·09 | 0·18 | 0·319 | 12·35 | 0·286 | 1·09 | 100·7 | 503 | 16 |
| kul3__m6x__2 | core | 29·24 | 0·96 | 12·15 | 27·15 | 3·29 | 12·23 | 1·60 | n.a. | 0·09 | 0·18 | 0·200 | 11·49 | 0·277 | 1·41 | 100·3 | 536 | 18 |
| kul3__m6x__3 | core | 29·54 | 0·91 | 14·49 | 28·76 | 3·21 | 10·90 | 1·33 | n.a. | 0·13 | 0·22 | 0·126 | 10·00 | 0·247 | 1·16 | 101·0 | 558 | 20 |
| kul3__m6x__4 | core | 29·50 | 0·91 | 12·32 | 27·52 | 3·16 | 11·93 | 1·51 | n.a. | 0·10 | 0·19 | 0·231 | 11·43 | 0·279 | 1·40 | 100·5 | 537 | 17 |
| kul3__m6x__5 | core | 29·07 | 1·19 | 12·18 | 28·03 | 3·34 | 11·59 | 1·42 | n.a. | 0·03 | 0·15 | 0·115 | 11·80 | 0·275 | 1·14 | 100·3 | 532 | 18 |
| kul3__m6x__6 | core | 29·23 | 1·06 | 11·94 | 27·02 | 3·21 | 11·96 | 1·56 | n.a. | 0·15 | 0·18 | 0·249 | 12·37 | 0·300 | 1·45 | 100·7 | 534 | 17 |
| kul3__m6x__7 | bright rim | 28·33 | 1·40 | 11·98 | 27·34 | 3·33 | 12·21 | 1·61 | n.a. | 0·08 | 0·19 | 0·300 | 12·29 | 0·286 | 1·08 | 100·4 | 507 | 16 |
| kul3__m6x__8 | bright rim | 28·61 | 1·33 | 12·17 | 27·29 | 3·19 | 12·02 | 1·48 | n.a. | 0·01 | 0·18 | 0·263 | 12·09 | 0·277 | 1·05 | 100·0 | 503 | 17 |
| kul3__m6x__9 | bright rim | 28·10 | 1·62 | 11·37 | 26·49 | 3·35 | 12·33 | 1·56 | n.a. | 0·09 | 0·15 | 0·319 | 13·77 | 0·327 | 1·18 | 100·7 | 519 | 15 |
| kul3__m6x__10 | bright rim | 28·04 | 1·64 | 11·22 | 26·39 | 3·25 | 12·24 | 1·45 | n.a. | 0·06 | 0·15 | 0·270 | 14·29 | 0·339 | 1·23 | 100·6 | 525 | 15 |
| kul3__m6x__11 | mid-bright near fracture | 28·38 | 1·46 | 11·88 | 26·97 | 3·24 | 11·97 | 1·53 | n.a. | 0·03 | 0·18 | 0·287 | 12·77 | 0·302 | 1·10 | 100·1 | 518 | 16 |
| kul3__m6x__12 | mid-bright near fracture | 28·48 | 1·42 | 11·75 | 27·09 | 3·24 | 12·20 | 1·42 | n.a. | 0·09 | 0·17 | 0·294 | 12·79 | 0·291 | 1·09 | 100·3 | 497 | 16 |
| KUL3__M8a__1 | core | 29·23 | 1·08 | 12·25 | 27·71 | 3·22 | 11·46 | 1·59 | n.a. | 0·10 | 0·17 | 0·264 | 11·78 | 0·290 | 1·37 | 100·5 | 535 | 17 |
| KUL3__M8a__2 | rim | 29·85 | 0·79 | 13·46 | 28·87 | 3·22 | 11·53 | 1·35 | n.a. | 0·04 | 0·16 | 0·114 | 9·56 | 0·219 | 1·16 | 100·3 | 513 | 20 |
| kul3__m10a__1 | core | 29·88 | 0·70 | 15·28 | 29·36 | 3·07 | 10·28 | 1·09 | n.a. | 0·10 | 0·23 | 0·094 | 9·17 | 0·213 | 1·12 | 100·6 | 528 | 21 |
| kul3__m10a__2 | core | 29·62 | 0·75 | 13·57 | 29·23 | 3·34 | 11·79 | 1·38 | n.a. | 0·07 | 0·20 | 0·107 | 8·94 | 0·214 | 1·02 | 100·2 | 541 | 21 |
| kul3__m10a__3 | core next to zircon | 29·40 | 0·93 | 12·89 | 28·16 | 3·15 | 11·74 | 1·35 | n.a. | 0·06 | 0·18 | 0·178 | 10·85 | 0·265 | 1·23 | 100·4 | 544 | 18 |
| kul3__m10a__4 | core next to zircon | 29·44 | 0·86 | 12·33 | 27·50 | 3·15 | 12·20 | 1·71 | n.a. | 0·09 | 0·19 | 0·173 | 11·14 | 0·263 | 1·36 | 100·4 | 528 | 18 |

n.a., not analysed.

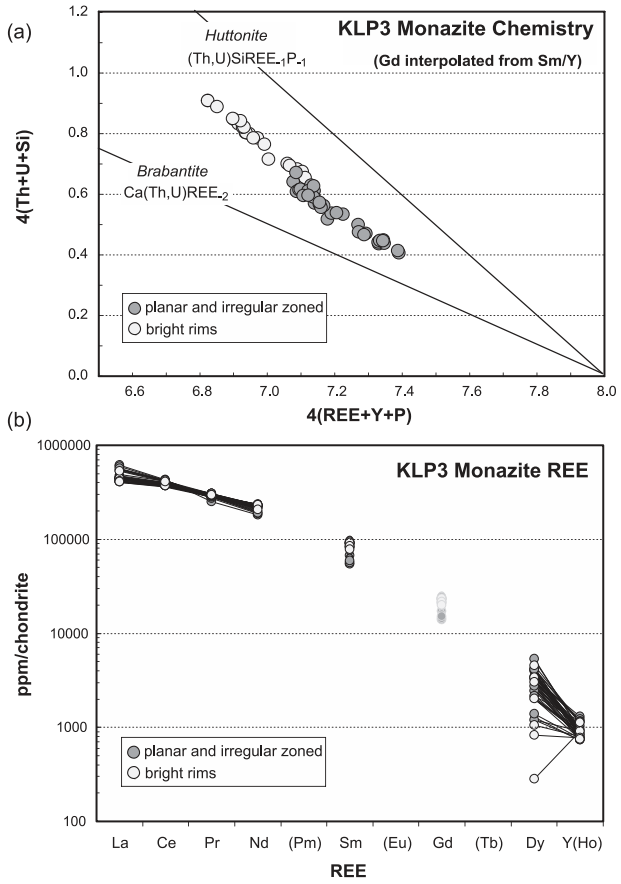


**Fig. 16.** Chemical systematics of KLP3 monazites. (a) Th + U + Si vs REE + Y + P compositional diagram illustrating the extents of covariation in monazite chemistry in terms of Th + U compared with REE + Y, and how these relate to the principal brabantite [Ca(Th,U)$REE_{-2}$] and huttonite [(Th,U)$SiREE_{-1}P_{-1}$] substitutions. Th-rich rims (bright rims, open circles) plot at higher huttonite:brabantite ratios than the main phase lower Th planar and irregularly zoned monazite. This reflects a change in crystallization environment to higher Si compared with Ca. (b) Chondrite-normalized REE diagram showing the compositions of KLP3 monazites, with two groups distinguished (bright rims; planar and irregularly zoned cores) as in the text. It should be noted that analyses were not obtained for Eu, Tb and Ho. Gd (symbols with grey outlines) was estimated by interpolation between Sm and Dy and Y. Y was placed on the diagram as a proxy for Ho. Chondrite values from Anders & Grevesse (1989).

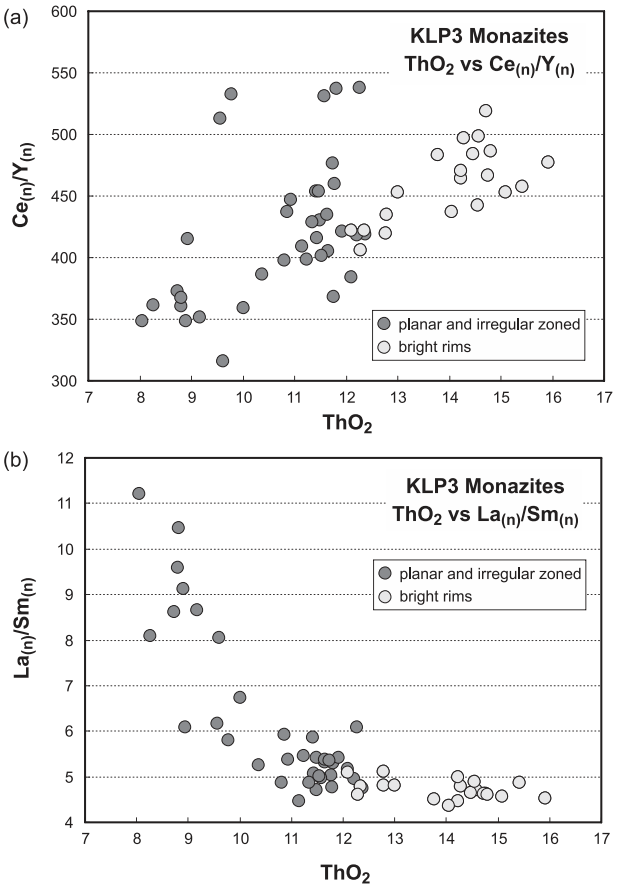


**Fig. 17.** KLP3 monazite chemical diagnostics in relation to $ThO_2$ contents. (a) Plot of monazite $Ce_n/Y_n$, a measure of HREE depletion, vs $ThO_2$ for the two textural–compositional varieties of monazite. Most analyses conform to a trend to higher $Ce_n/Y_n$ with increasing $ThO_2$, but five analyses (all from one grain) lie at higher $Ce_n/Y_n$ reflecting unusually large HREE depletions. (b) Plot of monazite $La_n/Sm_n$, a measure of LREE fractionation, vs $ThO_2$ for the two textural–compositional varieties of monazite. Bright rims have a flat LREE pattern irrespective of $ThO_2$, whereas irregular cores with the lowest $ThO_2$ are enriched in La relative to Sm. This may reflect their earlier crystallization from LREE-enriched melt.

High-HREE feathered-complex zircon cores and high Th/U planar-sector zircon yield $D_{REE}$(Zrc/Grt) values that increase across the HREE, from 1·4 at Gd to 6·7 at Lu. These $D_{HREE}$ values are higher than those expected for zircon–garnet equilibrium at 850–1000°C when compared with the $D_{REE}$(Zrc/Grt) values proposed by Harley *et al.* (2007) on the basis of empirical measurements (Whitehouse & Platt, 2003; Kelly & Harley, 2005; Harley & Kelly, 2007) and experimental results at 900–1000°C (Taylor, 2009). They are also significantly higher than equilibrium $D_{REE}$(Zrc/Grt) values deduced from the 900–1000°C experiments conducted by Rubatto & Hermann (2007). On the other hand, the measured $D_{HREE}$ values are comparable in relative fractionation (i.e. $D_{Yb}/D_{Gd}$) with those obtained in the 800–850°C experiments of Rubatto & Hermann (2007), and hence could imply equilibrium at 800–850°C if those experimental data are applicable. However, this is not considered to be the case here as the lower Th/U dark planar zircon and modified-lobate and elliptical infill zircon groups in KLP3 crystallized after the high-HREE cores and hence at similar or lower temperatures (and with similar Ti contents in zircon) on the KKB *P–T* path, not at higher temperatures. These groups have flat HREE patterns that are similar to those of host and adjacent garnet. The resultant $D_{HREE}$ values are in the range 1·0–0·55 from Gd to Lu, overlapping with the preferred 850–1000°C $D_{HREE}$(Zrc/

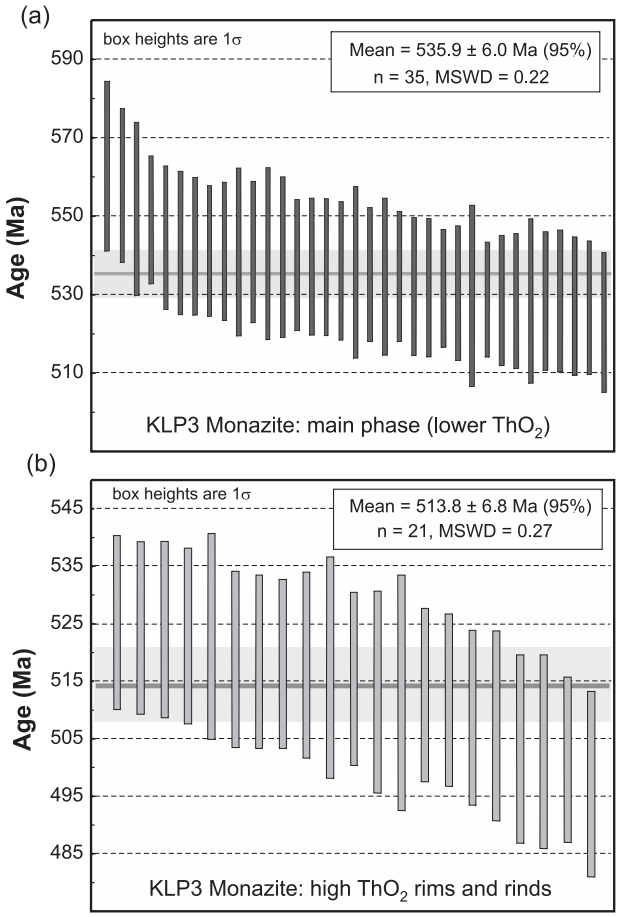


**Fig. 18.** Weighted average age plots for the main phase, lower $ThO_2$ planar and irregularly zoned monazite (a), and bright BSE higher $ThO_2$ monazite rims (b) in KLP3. Shaded fields in each case represent the best-fit weighted age and its associated error (95% confidence). Age errors on the analyses are shown by the vertical bars. Age calculated using Ludwig (2003).

Grt) values summarized by Harley *et al.* (2007). The lower Th/U sector-planar zircon group (three analyses) lead to $D_{HREE}$(Zrc/Grt) values that are near unity for Gd to Ho, close to the equilibrium $D_{HREE}$(Zrc/Grt) values reported for the higher $T$ (950–1000°C) subset of the experiments of Rubatto & Hermann (2007). $D_{HREE}$(Zrc/Grt) values calculated for zircon lobes and infills are lower (0·6–0·7 for Gd to Tm), compatible with zircon–garnet equilibrium if the Harley *et al.* (2007) values are appropriate.

In summary, zircon–garnet equilibrium can be inferred for only the lower Th/U, low-HREE zircon groups, which include both dark planar-zoned zircon and highly modified lobate–elliptical domains, inferred from the U–Pb geochronology to have formed at *c.* 545 ± 6 Ma. As explained in the section on zircon textures, some of this modification is interpreted to have occurred in the presence of melt because of the clear spatial relationship between the presence of preserved and closed-off cryptogranite inclusions and the modified zircon domains.

## Garnet–zircon–whole-rock REE relationships

The nature of the melts, and potentially the relative timing of crystallization of phases in the melts, can in principle be assessed using the measured zircon and whole-rock REE and comparing those with experimental or empirical zircon–melt REE partitioning relationships (e.g. Hinton & Upton, 1991; Sano *et al.*, 2002; Rubatto & Hermann, 2007). However, as discussed in depth by Hanchar & van Westrenen (2007), empirical and experimental zircon–melt $D_{REE}$ values vary considerably, and so lead to very different modelled whole-rock patterns using the same zircons. In the light of these discrepancies, and also given the improbability of zircon crystallization from pristine unfractionated melt at near-peak conditions (e.g. Kelsey *et al.*, 2008), the character of the melt during formation of the low-HREE zircon and garnet is addressed below using garnet–melt REE relationships.

Whole-rock MREE–HREE values calculated based on the average KLP3 garnet MREE–HREE composition are compared with the measured values in Fig. 22. Two sets of $D_{MREE-HREE}$(Grt/rock) values have been used to calculate the whole-rock patterns. The modelled patterns labelled '40' and '55' have been obtained using site-strain modelling (van Westrenen *et al.*, 2001) fits to experiments on low-grossular, $X_{Mg}30$ garnet coexisting with leucogranitic melt, conducted at 7 kbar and 900° and 950°C by Taylor (2009). In these fits the van Westrenen *et al.* (2001) 'ideal ion' parameter is 40, elastic response parameter 40 and site size 0·98 nm for model '40'. These values are 55, 70 and 0·983 respectively in the case of model '55'. The resultant calculated whole-rock REE patterns overlap with that of granitic leucosome KLP1.

The most significant differences between the calculated and modelled MREE–HREE whole-rock REE patterns are the extremely low predicted Eu contents. This reflects the very strongly negative europium anomaly (Eu/Eu*) measured in the garnets, a feature typical of many garnets in granulite-facies migmatites and leucogranites (Watt & Harley, 1993; Harris *et al.*, 1994; Bea, 1996). This is attributable to either the presence of peritectic K-feldspar or variable extents of feldspar crystallization from melt prior to garnet growth (Watt & Harley, 1993; Carrington & Watt, 1996). The distinctive feldspar REE compositions measured in KLP3 are similar to those of K-feldspars and plagioclases in granulite migmatites from the Aravalli–Delhi orogenic belt, described by Buick *et al.* (2010) and interpreted by those researchers as reflecting the prograde peritectic growth of K-feldspar and later growth of plagioclase on melt crystallization. In the present case, however, the similarities in Eu abundances in both feldspars are consistent with their contemporaneous crystallization

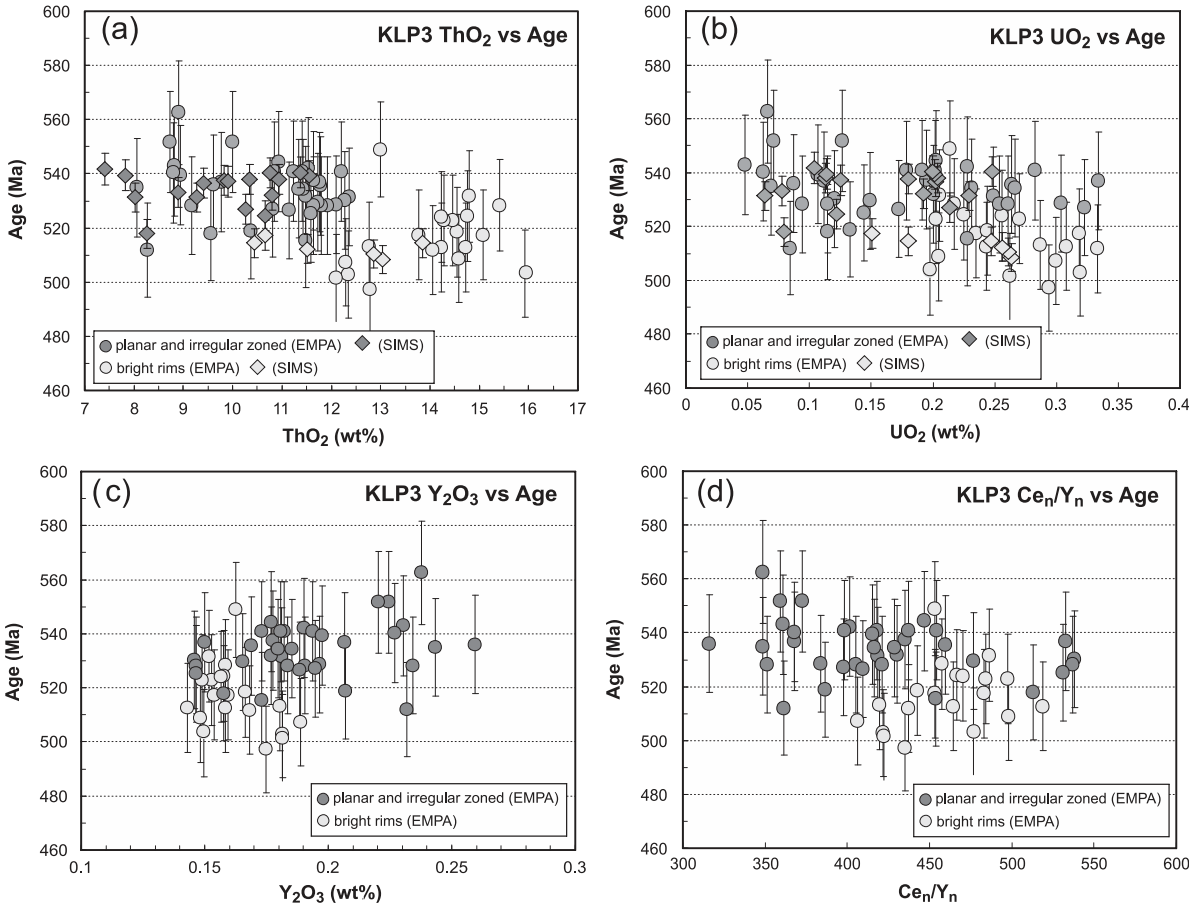


**Fig. 19.** Chemistry–age relationships in KLP3 monazites: (a) $ThO_2$ content vs chemical (circles) and SIMS isotopic (diamonds) age; (b) $UO_2$ content vs chemical (circles) and SIMS isotopic (diamonds) age; (c) $Y_2O_3$ content vs chemical age; (d) $Ce_n/Y_n$, or REE fractionation, vs chemical age. In each diagram the two monazite textural types (planar and irregularly zoned vs bright rims) are distinguished. Error on each age determination is shown by vertical bars extending up and down from each symbol. Bright rims tend to yield younger ages that correlate with all chemical diagnostics.

from melt on cooling, and the phase diagram modelling of KLP3 (see Supplementary Data Electronic Appendix 5) shows that two feldspars coexist with melt over a considerable temperature interval and form during cooling at temperatures above the incoming of biotite (e.g. >830°C for KLP3 with 1 wt % $H_2O$ at 7 kbar). Calculations using the analysed feldspar REE compositions in KLP3 (Table 3) and bulk-rock REE data indicate that the crystallization of 20–30 wt % feldspar prior to garnet crystallization or garnet–melt REE equilibration can account for the discrepancies between the measured whole-rock (KLPl and KLP3) Eu contents and those modelled from the KLP3 garnet MREE–HREE pattern.

The melt with which the KLP3 garnet composition is calculated to be in trace element equilibrium is depleted in MREE and HREE relative to the KLP3 bulk-rock composition. The calculations instead imply a melt similar to KLPl in terms of its Sm and HREE contents. KLP3 itself is relatively enriched in Sm and the HREE relative to model melt, a feature that could be produced through entrainment and dissolution–reprecipitation of peritectic garnet and/or wall-rock garnet (e.g. Taylor & Stevens, 2010), or reaction with and assimilation of wall-rock leading to the crystallization and accumulation of magmatic garnet. The extreme depletion in Eu in the analysed leucosome-hosted KLP3 garnets, which as noted above suggests considerable prior feldspar crystallization, is most consistent with the latter scenario.

The $D_{MREE-HREE}$(Grt/rock) calculations confirm that the bulk-rock composition of KLP3 does not correspond to a melt in equilibrium with the garnet hosted within the rock. Based on the results from the previous section on zircon–garnet relationships this also implies that the low-HREE zircon (planar and lobate types) did not crystallize from a melt with the composition of KLP3 itself. Instead, KLP3 at the time of garnet crystallization or equilibration was likely to have been a crystal mush. The crystallization of considerable feldspar preceded garnet accumulation

*Table 7: Monazite isotopic data: Kulappara sample KLP3, Kerala Khondalite Belt*

| Grain, spot | Type | Concentration | | | | | | | Isotopic ratio | | | | | | | | Concordance | | Apparent age (Ma) | | | | | | | |
|---|---|---|---|---|---|---|---|---|---|---|---|---|---|---|---|---|---|---|---|---|---|---|---|---|---|---|
| | | U (ppm) | Th (ppm) | Th/U | Pb (ppm) | $^{204}$Pb (ppb) | $^{206}$Pb/$^{204}$Pb | *f*206 (%) | $^{208}$Pb/$^{232}$Th | ± | $^{207}$Pb/$^{235}$U | ± | $^{206}$Pb/$^{238}$U | ± | $^{207}$Pb/$^{206}$Pb | ± | %con (7/6) | %con (8/6) | $^{208}$Pb/$^{232}$Th | ± | $^{206}$Pb/$^{238}$U | ± | $^{207}$Pb/$^{235}$U | ± | $^{207}$Pb/$^{206}$Pb | ± |
| mnz-1-1 | core | 674 | 78071 | 118·9 | 1893 | 0·05 | 999981 | 0·002 | 0·0862 | 0·0009 | 37·3764 | 0·1079 | 0·7294 | 0·0122 | 0·06139 | 0·00044 | 95·6 | 101·1 | 527 | 11 | 532·8 | 5·5 | 556·2 | 7·1 | 653 | 15 |
| mnz-1-2 | core | 1676 | 94612 | 57·9 | 2364 | 0·12 | 999981 | 0·002 | 0·0860 | 0·0009 | 18·4064 | 0·0352 | 0·7087 | 0·0109 | 0·05978 | 0·00019 | 97·7 | 100·7 | 528 | 11 | 531·8 | 5·5 | 544·0 | 6·5 | 595 | 7 |
| mnz-1-3 | rim | 2298 | 114135 | 51·0 | 2747 | 8·04 | 20268 | 0·092 | 0·0820 | 0·0009 | 16·4394 | 0·0464 | 0·6574 | 0·0105 | 0·05817 | 0·00033 | 99·0 | 100·1 | 507 | 11 | 507·8 | 5·2 | 513·0 | 6·4 | 536 | 12 |
| mnz-1-4 | core | 1064 | 93500 | 90·2 | 2263 | 20·58 | 3789 | 0·491 | 0·0847 | 0·0009 | 28·7952 | 0·0802 | 0·6773 | 0·0114 | 0·05798 | 0·00043 | 99·8 | 99·6 | 526 | 11 | 524·2 | 5·4 | 525·1 | 6·9 | 529 | 16 |
| mnz-1-5 | rim | 2280 | 112562 | 50·6 | 2717 | 0·16 | 999981 | 0·002 | 0·0823 | 0·0009 | 15·9613 | 0·1082 | 0·6723 | 0·0106 | 0·05922 | 0·00031 | 97·6 | 102·0 | 500 | 11 | 510·1 | 5·2 | 522·1 | 6·4 | 575 | 11 |
| mnz-1-6 | core | 1860 | 89984 | 49·6 | 2252 | 10·17 | 13469 | 0·139 | 0·0851 | 0·0009 | 15·8767 | 0·0544 | 0·6850 | 0·0111 | 0·05837 | 0·00037 | 99·4 | 100·2 | 526 | 11 | 526·6 | 5·4 | 529·8 | 6·7 | 543 | 14 |
| mnz-1-7 | core | 981 | 90652 | 94·8 | 2244 | 3·80 | 19423 | 0·096 | 0·0870 | 0·0009 | 29·8352 | 0·0707 | 0·7100 | 0·0113 | 0·05921 | 0·00031 | 98·7 | 101·1 | 532 | 11 | 537·6 | 5·5 | 544·8 | 6·7 | 574 | 12 |
| mnz-1-8 | rim | 1569 | 121193 | 79·3 | 2887 | 12·77 | 8824 | 0·211 | 0·0830 | 0·0009 | 25·1779 | 0·0515 | 0·6682 | 0·0109 | 0·05838 | 0·00036 | 98·9 | 99·8 | 515 | 11 | 514·1 | 5·3 | 519·6 | 6·6 | 544 | 13 |
| mnz-1-9 | core | 552 | 70532 | 131·2 | 1701 | 3·80 | 10792 | 0·173 | 0·0858 | 0·0009 | 41·3546 | 0·1083 | 0·7187 | 0·0146 | 0·06072 | 0·00084 | 96·4 | 99·7 | 533 | 11 | 530·9 | 5·5 | 549·9 | 8·6 | 629 | 29 |
| mnz-6-1 | core | 1567 | 86119 | 56·4 | 2178 | 1·69 | 69609 | 0·027 | 0·0869 | 0·0009 | 17·9251 | 0·0274 | 0·7174 | 0·0118 | 0·05986 | 0·00041 | 97·8 | 101·8 | 528 | 11 | 537·3 | 5·5 | 549·1 | 6·9 | 598 | 15 |
| mnz-6-2 | core | 1092 | 86843 | 81·6 | 2164 | 11·22 | 7317 | 0·255 | 0·0868 | 0·0010 | 25·7221 | 0·0874 | 0·6930 | 0·0118 | 0·05787 | 0·00044 | 100·4 | 100·5 | 534 | 11 | 536·9 | 5·7 | 534·6 | 7·1 | 525 | 16 |
| mnz-6-3 | rim | 2154 | 91538 | 43·6 | 2257 | 12·10 | 12792 | 0·146 | 0·0830 | 0·0009 | 13·8364 | 0·0175 | 0·6608 | 0·0101 | 0·05774 | 0·00018 | 99·8 | 98·9 | 520 | 11 | 514·1 | 5·3 | 515·1 | 6·2 | 519 | 7 |
| mnz-6-4 | core | 1765 | 82558 | 48·0 | 2109 | 9·76 | 13571 | 0·138 | 0·0867 | 0·0009 | 15·2581 | 0·0334 | 0·7008 | 0·0112 | 0·05859 | 0·00031 | 99·4 | 100·0 | 536 | 11 | 536·2 | 5·6 | 539·3 | 6·7 | 552 | 11 |
| mnz-6-5 | rim | 2238 | 100796 | 46·2 | 2461 | 3·55 | 45123 | 0·041 | 0·0826 | 0·0009 | 14·6542 | 0·0242 | 0·6648 | 0·0105 | 0·05834 | 0·00029 | 98·9 | 99·3 | 516 | 11 | 511·9 | 5·2 | 517·5 | 6·4 | 542 | 11 |
| mnz-6a-1 | core | 906 | 65158 | 73·7 | 1640 | 4·08 | 16839 | 0·111 | 0·0876 | 0·0010 | 23·3381 | 0·0650 | 0·7199 | 0·0122 | 0·05959 | 0·00044 | 98·3 | 100·1 | 541 | 11 | 541·4 | 5·8 | 550·6 | 7·2 | 588 | 16 |
| mnz-6a-2 | rim | 1310 | 93484 | 73·2 | 2245 | 35·25 | 2685 | 0·692 | 0·0835 | 0·0009 | 23·6430 | 0·0679 | 0·6788 | 0·0108 | 0·05897 | 0·00029 | 98·2 | 99·7 | 518 | 11 | 516·9 | 5·4 | 526·0 | 6·5 | 565 | 11 |
| mnz-6a-3 | core | 986 | 68812 | 71·6 | 1725 | 0·07 | 999981 | 0·002 | 0·0872 | 0·0010 | 22·7395 | 0·1024 | 0·7202 | 0·0121 | 0·0599 | 0·00043 | 97·8 | 103·1 | 522 | 11 | 539·0 | 5·7 | 550·8 | 7·1 | 599 | 16 |
| mnz-6a-4 | rim | 691 | 72639 | 107·8 | 1716 | 5·16 | 9694 | 0·193 | 0·0836 | 0·0009 | 34·5858 | 0·1199 | 0·6995 | 0·0120 | 0·0607 | 0·00051 | 95·9 | 102·3 | 505 | 11 | 517·5 | 5·3 | 538·5 | 7·2 | 628 | 18 |
| mnz-6a-5 | core | 1999 | 81408 | 41·8 | 2077 | 4·29 | 34652 | 0·054 | 0·0858 | 0·0009 | 13·3234 | 0·0419 | 0·7003 | 0·0109 | 0·05917 | 0·00026 | 98·5 | 102·0 | 520 | 11 | 530·9 | 5·5 | 539·0 | 6·5 | 573 | 9 |
| mnz-x-1 | core | 1777 | 95854 | 55·3 | 2432 | 1·94 | 69012 | 0·027 | 0·0870 | 0·0009 | 17·3471 | 0·0761 | 0·7092 | 0·0119 | 0·05914 | 0·00043 | 98·8 | 99·3 | 542 | 11 | 537·6 | 5·6 | 544·3 | 7·0 | 572 | 16 |
| mnz-x-2 | core | 2162 | 94315 | 44·8 | 2440 | 9·83 | 16639 | 0·112 | 0·0874 | 0·0009 | 14·0326 | 0·0412 | 0·7027 | 0·0115 | 0·05833 | 0·00039 | 99·9 | 99·3 | 544 | 11 | 539·9 | 5·5 | 540·4 | 6·9 | 542 | 14 |
| mnz-x-3 | rim | 1757 | 101254 | 59·1 | 2562 | 0·60 | 221277 | 0·008 | 0·0872 | 0·0009 | 18·5921 | 0·0174 | 0·7191 | 0·0110 | 0·05982 | 0·00023 | 97·9 | 100·4 | 537 | 11 | 538·9 | 5·4 | 550·2 | 6·5 | 597 | 8 |
| mnz-x-4 | core | 1745 | 99586 | 58·5 | 2530 | 10·13 | 13026 | 0·143 | 0·0874 | 0·0009 | 18·4706 | 0·0255 | 0·7152 | 0·0115 | 0·05935 | 0·00034 | 98·6 | 99·5 | 543 | 11 | 540·1 | 5·6 | 547·8 | 6·8 | 579 | 13 |

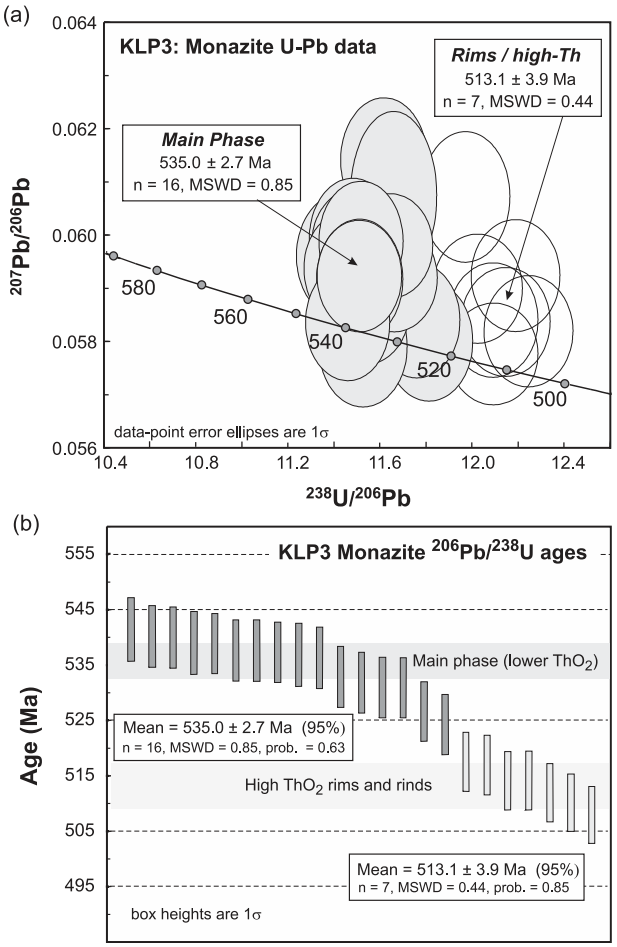


**Fig. 20.** (a) U–Pb geochronological data for KLP3 monazites, presented as a $^{204}$Pb-corrected Tera–Wasserburg concordia diagram. The two chemically and texturally defined monazite types are treated separately, and weighted mean $^{206}$Pb/$^{238}$U ages are reported for each population at the 95% confidence level. (b) Weighted $^{206}$Pb/$^{238}$U age data for the two monazite types distinguished on textural and $ThO_2$ grounds.

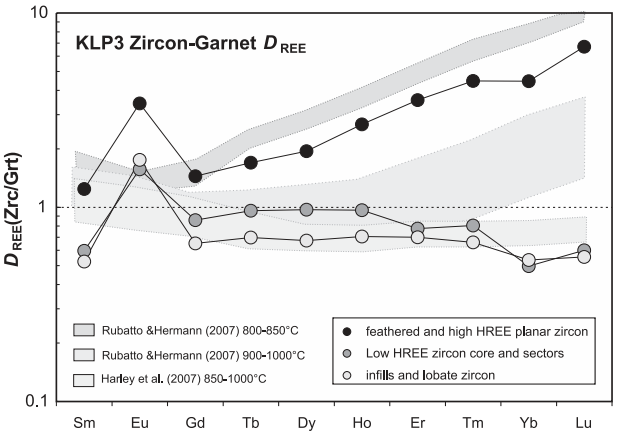


**Fig. 21.** Zircon–garnet REE distribution patterns, $D_{REE}$(Zrc/Grt), from Sm to Lu. $D_{REE}$(Zrc/Grt) patterns represented by circles are calculated for the three zircon types coupled with average garnet REE contents. The shaded fields depict the ranges of experimental $D_{REE}$(Zrc/Grt) from Rubatto & Hermann (2007), and the empirical or experimental $D_{REE}$(Zrc/Grt) from Harley *et al.* (2007).

in KLP3, causing the extreme Eu depletion in later-crystallizing garnet (and zircon) relative to the host-rock. This is consistent with the calculated phase diagrams presented previously (Fig. 6a and b), in which feldspar and melt coexist to temperatures of at least 950°C in the KLP3 composition, and also in the KLP3 minus 5 wt % garnet composition, at >6·5 kbar.

## Garnet–feldspar–monazite REE mass balance and Th–U modelling

An alternative approach to evaluating the mineral–melt relationships associated with migmatization is to apply trace element mass-balance calculations to the leucogranite vein (KLP3), leucosome (KLP1) and mesosome (KLP2). The measured monazite, garnet and feldspar REE compositions in KLP3 can be used to estimate the amount of each mineral needed to account for the whole-rock REE composition of KLP3, and this approach can be extended to KLP1 and KLP2 assuming the garnet, feldspars and monazite in those rocks are similar in composition. The results of these REE mass-balance calculations are depicted in Fig. 23, assuming a monazite with Eu at 1000 times chondrite.

The REE profile of KLP3 can be matched by a combination of 5 wt % garnet (3·4 vol. %) plus 0·041 wt % monazite (0·022 vol. %), 35 wt % plagioclase and 30 wt % K-feldpsar. The lower MREE–HREE contents of leucosome KLP1 can be matched by a combination of 0·004 wt % monazite, 2 wt % garnet and 60% K-feldspar. The migmatitic pelite KLP2 gives a modelled REE fit at 16 wt % garnet, 22 wt % plagioclase, 20 wt % K-feldspar and 0·03 wt % monazite. The modal proportions of garnet calculated for KLP3 and KLP1 are in good agreement with those estimated from petrographic analysis.

The calculations demonstrate that rather small variations in the modal abundances of potentially heterogeneously distributed, low-abundance, phases—in this case monazite and garnet—will have a major impact on the whole rock REE patterns and hence on modelling calculations such as those involving garnet–melt $D_{MREE–HREE}$. This is particularly severe if there is heterogeneity in or localization of monazite occurrence, which not only can cause order of magnitude variations in the LREE but also, as shown by comparison of KLP3 with KLP1, significant (factor of two) variations in Gd, Tb and Dy, depending on the monazite REE composition.

The mass-balance calculations for monazite can be tested using the measured whole-rock U and Th contents, assuming the average KLP3 monazite composition applies to each rock. The average U content of KLP3 monazite

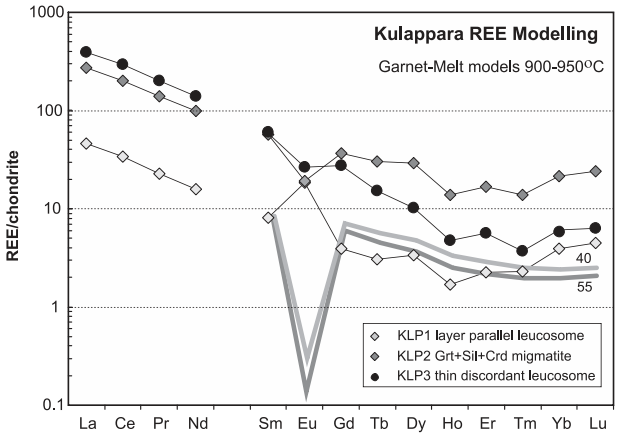


**Fig. 22.** Comparison of measured REE patterns for KLPl, KLP2 and KLP3 with those calculated from modelled experimental garnet–melt $D_{MREE–HREE}$ values for low-Grs garnets obtained at 7 kbar (Taylor, 2009) (curves labelled '40' and '55'). These model garnet–melt $D_{MREE–HREE}$ values are based on the single site elastic strain model of van Westrenen *et al.* (2001). Model '40': 'ideal ion' parameter 40, elastic response parameter 40 and site size 0·98 nm. Model '55': 'ideal ion' parameter 55, elastic response parameter 70 and site size 0·983 nm.

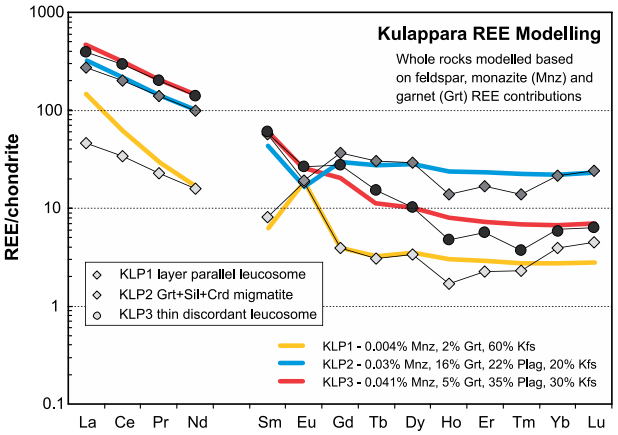


**Fig. 23.** Measured Kulappara whole-rock REE patterns compared with patterns calculated using combinations of monazite, garnet and feldspar, based on mineral REE compositions measured in KLP3. (See text for discussion.)

(1800 ppm) leads to estimates of 0·09 wt % monazite in KLP3, 0·06 wt % in KLPl and 0·15 wt % in KLP2. Whereas the estimate for KLP3 is consistent with that determined using the LREE, in the cases of KLPl and KLP2 the amounts of monazite required to produce the measured whole-rock U contents are far greater than indicated by the LREE. They are also significantly higher than those estimated by mass balance using the whole-rock Th contents coupled with the average monazite Th content in KLP3. For KLPl 0·006 wt % of monazite is required for Th mass balance, a similar value to that deduced from the LREE (0·004 wt %). In KLP3 less monazite is required to achieve Th mass balance (0·033 wt %) than LREE mass balance (0·041 wt %). Similarly, in KLP2, only 0·01 wt % monazite is estimated from the Th content whereas 0·03 wt % is required for LREE mass balance. These discrepancies suggest that a Th-poor LREE phase such as apatite may be present in both KLP2 and KLP3.

Assuming the whole-rock U analyses are correct, there also must be another significant contributor to the U budgets of the leucosome KLPl and migmatitic pelite KLP2. This phase cannot be zircon, as the measured Zr contents of each rock lead to maximum zircon contents of 0·009–0·024 wt % and hence a trivial contribution of <0·06 ppm to the U budget of each rock. We conclude that a U-rich phase must be present in very small amounts in each of these rocks.

## Zircon HREE and Th–U–Yb chemistry: melt entrapment and wall-rock interaction

The common observation of inclusions with negative crystal shapes or curved boundaries in the core sectors of KLP3 zircons suggests that the zircons may have initially grown as 'hopper' crystals in which the planar-sector euhedral rims grew faster than core domains. The quartzofeldspathic inclusions in zircons are similar in mineralogy and microtexture to coarsened 'nanogranite' inclusions (Cesare *et al.*, 2009), consistent with initial crystallization of the Kulappara zircons in the presence of granitic melt. These zircons are inferred to have crystallized from a melt during cooling from peak-$T$ conditions.

A sequence of events leading to the formation of the texturally and compositionally complex zircons is schematically illustrated in Fig. 24, and discussed in detail. Based on their internal textures the zircon cores are envisaged as having contained tubes of melt (or melt + fine crystals) situated between zircon axial 'feathered' planes. These tubes would have in many cases been sealed off by further planar-sector zircon growth across and over the ends of the tubes, thus being preserved as quartz–feldspar inclusions once the melt crystallized (Fig. 24a). Based on the elevated $D_{HREE}$(zircon/garnet) this zircon crystallization to form the high-HREE and higher Th/U complex feathered cores and planar-sector zoned zircon occurred prior to garnet growth or interaction.

In those instances in which the tubes were not fully sealed off by high-HREE planar zircon, subsequent zircon dissolution–precipitation or new lower HREE planar-sector zircon growth in the presence of melt could result in infilling or sealing-off of tubes (Fig. 24b). One textural manifestation of this process would be the elliptical to circular domains of strongly zoned zircon now preserved in many zircon cores (e.g. Z2, Z5; Fig. 8). Consistent $D_{HREE}$(zircon/garnet) values indicate that garnet–melt interaction accompanied the continued precipitation of lower Th/U, lower HREE planar zircon to enclose and isolate any remaining melt tubes within hollow zircon cores.

Modification of these planar zones by lobate invasive domains, and infilling of exposed tubes by elliptically zoned zircon, may have initially proceeded as the melt crystallized and later continued through further *in situ* dissolution–reprecipitation of zircon subsequent to melt crystallization, all in the presence of garnet (Fig. 24c).

As indicated above, the change from higher Th/U, higher HREE zircon to lower Th/U, lower HREE zircon occurs during the growth of the sector-planar zoned zircon in the presence of melt (Corfu *et al.*, 2003). Grimes *et al.* (2007) have demonstrated that the U/Yb ratio of igneous or anatectic zircon reflects that of the melt from which it crystallized because of the similarity in zircon/melt partition coefficients for U and Yb (Bea *et al.*, 1994: 254 and 278 respectively). The U/Yb ratios of the KLP3 zircons change dramatically (Fig. 11; Table 4), from 2·9 to 34·1 in the case of planar zircon, and to >40 for lobate domains and infills. This requires that the melt U/Yb must have increased dramatically during zircon crystallization, accompanied by only minor increases in U. Th/Yb in zircon also increases, but only moderately because zircon Th contents decrease from the higher HREE to lower HREE groups.

We propose that the reason for the increases in U/Yb and Th/Yb, and decreases in Y, in the zircons is modification of the coexisting melt composition through interaction with its host- or wall-rock. This interaction is proposed to have stimulated the precipitation of garnet, as indicated by the preserved mineral assemblages and by the switch in zircon chemistry to lower HREE compositions. Hence, the change in planar-zoned zircon chemistry reflects a transition from open-system crystallization (e.g. of feldspars and quartz plus limited zircon) and melt transfer, to closed-system or localized melt crystallization principally controlled by garnet–melt equilibrium. This transition occurred following cooling from the metamorphic peak $T$ and after significant feldspar crystallization, and most probably corresponds to the time interval over which the

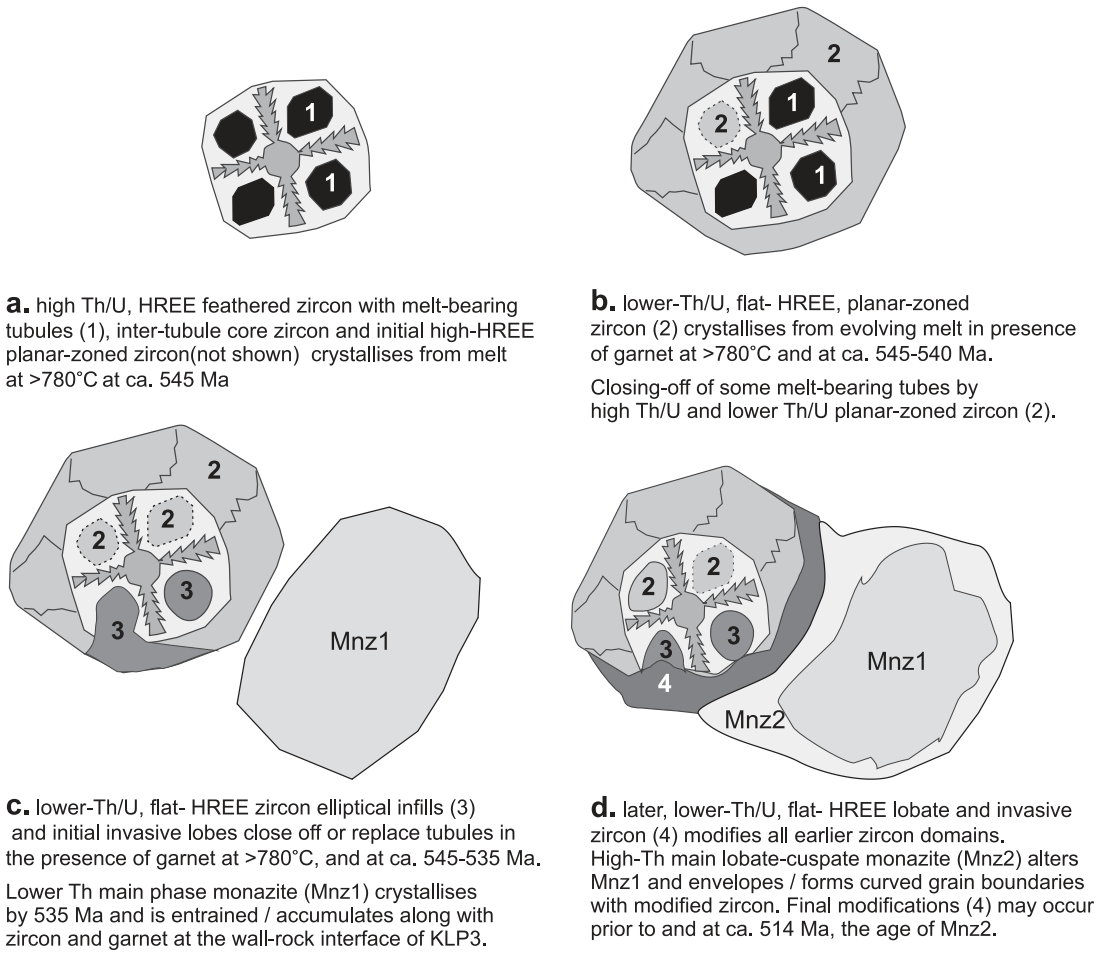


**a.** high Th/U, HREE feathered zircon with melt-bearing tubules (1), inter-tubule core zircon and initial high-HREE planar-zoned zircon(not shown) crystallises from melt at >780°C at ca. 545 Ma

**b.** lower-Th/U, flat- HREE, planar-zoned zircon (2) crystallises from evolving melt in presence of garnet at >780°C and at ca. 545-540 Ma.

Closing-off of some melt-bearing tubes by high Th/U and lower Th/U planar-zoned zircon (2).

**c.** lower-Th/U, flat- HREE zircon elliptical infills (3) and initial invasive lobes close off or replace tubules in the presence of garnet at >780°C, and at ca. 545-535 Ma.

Lower Th main phase monazite (Mnz1) crystallises by 535 Ma and is entrained / accumulates along with zircon and garnet at the wall-rock interface of KLP3.

**d.** later, lower-Th/U, flat- HREE lobate and invasive zircon (4) modifies all earlier zircon domains. High-Th main lobate-cuspate monazite (Mnz2) alters Mnz1 and envelopes / forms curved grain boundaries with modified zircon. Final modifications (4) may occur prior to and at ca. 514 Ma, the age of Mnz2.

**Fig. 24.** Schematic representation of the stages of zircon growth and modification preserved in the internal textures and mineral geochemistry of KLP2 zircons, linked to monazite and garnet crystallization or interaction from *c.* 545 to 535 Ma and further modification by 514 Ma. Stages (a)–(d) are described further in the text.

transgressive leucogranite vein (KLP3) ceased to act as a melt conduit and its remaining melt stagnated. This trapped residual melt may then have mingled or mixed with melts present in the local wall-rock migmatite, or may have undergone assimilation–fractional crystallization, or both. Zircon is sensitive to this change in melt environment because of its low modal abundance compared with garnet, which dominates the HREE budget of both the leucogranite and migmatite. The U/Yb of the leucogranitic vein KLP3 is 1·6, similar to that of the subconcordant leucosome KLP1 (1·7) despite very different garnet contents, and is consistent with both equilibrating with garnet during their final crystallization.

The close inverse relationship between the Th/U and U/Yb ratios of the zircons in KLP3 allows decreases in the former ratio to be used as a signature of the onset of closed-system melt crystallization and an approach to garnet–zircon–melt equilibration in this instance. The minimum age for this is that obtained for the main, lower $ThO_2$, monazite population in KLP3: 535·9 ± 6·1 Ma based on the EMPA monazite dating, or 535·0 ± 2·8 Ma based on SIMS $^{206}Pb/^{238}U$ data. $D_Y$(Mnz–Zrc) values obtained by pairing this monazite population with the lower HREE zircon and garnet in KLP3 are 6·5–7·5, slightly lower than the values preferred by Rubatto *et al.* (2006) for monazite–zircon–garnet equilibrium at low *P* but consistent with zircon growth prior to and overlapping in time with that of monazite. $^{206}U/^{238}Pb$ ages of 550 ± 13 Ma for the low Th/U, low-HREE planar zircon and 541·9 ± 5·5 Ma for the lobate and elliptical infills directly confirm this inference. The high-HREE zircon, with a $^{206}U/^{238}Pb$ age of 544·2 ± 8·8 Ma, crystallized in open-system conditions prior to melt entrapment and garnet–melt interaction.

## ZIRCON AND MONAZITE GROWTH AND MODIFICATION IN KKB MIGMATITES

### High-*T* post-peak zircon crystallization during melt entrapment and stagnation

Cesare *et al.* (2009) have clearly demonstrated the preservation of melt droplets, <25 μm in size, in refractory minerals in migmatites. In particular, they have described nanogranite inclusions in garnets from the Trivandrum Block, either crystallized as Qtz–Ab–Kfs–Bt cryptocrystalline aggregates or present as glass if the inclusions are <15 μm in diameter. Their results provide direct evidence for the growth of garnet in KKB migmatites in the presence of melt, and the timing of at least some of this garnet formation can now be constrained from our zircon age and chemistry data. This can be combined with the age and chemistry evidence from monazite to deduce the overall time scale of melt availability, crystallization and entrapment at Kulappara and hence in at least part of the Trivandrum Block.

In this study we have identified former melt inclusions, preserved as cryptocrystalline granitic inverse crystals (compare nanogranite) within 'hopper' zircon in KLP3. High-HREE, higher Th/U zircon crystallized in melt in open-system conditions at a best-fit $^{206}U/^{238}Pb$ age of 544·2 ± 8·8 Ma (i.e. 545 ± 9 Ma). Crystallization was initially rapid, resulting in feathered hollow or hopper zircon prismatic cores, each featuring four tubular and melt-filled hollow volumes between the (100) and (010) zone axes of the prismatic zircon crystals. Continued crystallization was concentrated on rims, producing weakly planar and planar-sector zoned outer domains, still in the presence of melt and under initially open-system conditions in which this melt had a low U/Yb ratio (Fig. 24a).

Further crystallization of zircon in the presence of melt occurred in the time interval from 542 ± 6 Ma to 535 ± 6 Ma, the latter age being the mean age of 'main phase' monazite crystallization. At this time (*c.* 542–536 Ma) the leucosome in which the zircon (and monazite) crystallized became trapped and underwent interaction with its host-rock migmatite. This resulted in the crystallization of planar zircon with lowered Th/U and HREE (Fig. 24b), reflecting an approach to REE equilibrium with garnet now crystallizing from the melt which was modified by wall-rock assimilation and closed-system fractionation. This later planar-zoned zircon, which evolved to high U/Yb as a consequence of garnet growth, infilled or closed off remaining melt tubes in zircon cores, trapping cryptogranite. Finally, infilled or complete zircon underwent *in situ* dissolution–precipitation (Putnis, 2002; Giesler *et al.*, 2007) in the presence of garnet, leading to the production of invasive and transgressive lobate zircon domains (Fig. 24c and d). This potentially occurred from at least 542 to 535 Ma based on the zircon $^{206}U/^{238}Pb$ age spread, but more probably occurred at or continued to *c.* 514 Ma, the statistically significant age obtained for the distinctive high-Th cuspate–lobate rims on monazite [514 ± 7 Ma (EMPA); 513 ± 6 Ma (SIMS)], supported by evidence for similar ages from moderate Th/U zircon lobate rinds.

### Implications for monazite ages at Kulappara and Trivandrum Block

The monazite textures supported by trace element and REE signatures, Th–U–Pb chemical dating and SIMS isotopic age dating clearly demonstrate two stages of monazite growth or modification in the leucogranite vein and its margin, one at *c.* 536 ± 6 Ma (EMPA) or 535 ± 6 Ma (SIMS) and the other at 514 ± 7 Ma (EMPA) or 513 ± 6 Ma (SIMS). The older age defines the timing of crystallization of monazite from the leucogranite in the presence of garnet and earlier-crystallized or accumulated feldspars, on cooling through *c.* 800–780°C from peak metamorphic

conditions. The younger age is ascribed to dissolution–precipitation and associated zircon–monazite grain boundary migration post-dating melt crystallization.

Santosh *et al.* (2006a) also found two textural types and chemical EMPA age populations of monazite at Kulappara. High-Th rims gave a population age of $503 \pm 9$ Ma, whereas generally lower Th monazite core domains produced an older and skewed age population with a major peak at $564 \pm 13$ Ma and a smaller broad peak at *c.* 600 Ma. In the present study only three of the 33 monazite core domain analyses yield mean EMPA ages that are older than 550 Ma, and no SIMS monazite $^{206}U/^{238}Pb$ ages were older than $541{\cdot}4 \pm 5{\cdot}8$ Ma. There is no evidence in our KLP3 data for inherited or early metamorphic monazite corresponding to the 600 Ma group of Santosh *et al.* (2006a), nor for a major monazite population >560 Ma.

These differences in monazite age populations may reflect the choice of sample. In this study we have focused on a cross-cutting leucosome sheet and its margin with adjacent migmatite that contains layer-parallel leucosomes, and so have maximized the potential to analyse *in situ* melt-hosted or melt-crystallized monazite. Santosh *et al.* (2006a) analysed monazite grains separated from the dominant Grt–Sil–Crd migmatitic pelite (analogous to KLP2) and so may have sampled monazites associated with sillimanite-rich foliae. However, despite the differences in sampling strategy both studies clearly distinguish the younger high-Th monazite group, with ages of less than *c.* 520 Ma, and identify older core domains with lower $ThO_2$ and variably mottled or planar-sector zoning. We interpret these common monazite cores, formed at *c.* 535 Ma in our analysed sample, as directly crystallized from a melt, a conclusion supported by the whole-rock REE mass-balance calculations performed above. The interpretation in other studies of similarly textured monazites as being of detrital origin (e.g. Santosh *et al.*, 2005a, 2006a) must be treated with considerable caution.

## CONCLUSIONS

The monazite, zircon and garnet trace element and chemical and isotopic age data described in this study point to the post-peak crystallization of accessory minerals in leucogranite from the Trivandrum Block from *c.* 545 to 535 Ma. Melt-precipitated zircon formed throughout this time span, whereas most monazite crystallized from melt by 535 Ma.

Marked changes to lower Th/U and $Yb_n/Gd_n$ ratios in zircons occurred during their growth, correlated with a dramatic change in microtexture from initial 'hopper'-like feathered-core and outer planar sector domains to darker planar zones and elliptical to lobate infilling and replacement zircon. The initial zircon crystallized rapidly from melt from *c.* 545 Ma under open-system conditions in which the host-rock mineralogy had no chemical impact. A consistent relation between zircon REE chemistry and its host-rock, indicated by close correspondence between measured and modelled whole-rock REE abundances, indicates that this zircon precipitated prior to crystallization of monazite and garnet, trapping melt as inclusions that later crystallized to cryptogranite. Further zircon crystallization ensued under localized closed-system conditions correlated with melt entrapment, leading to the establishment of zircon–garnet REE equilibrium at least on local (i.e. millimetre to centimetre) scales, at temperatures greater than *c.* 780°C, from *c.* 542 to 535 Ma.

The change in zircon chemistry, coupled with the *in situ* microtextural information, demonstrates that zircon can be a sensitive indicator of changing conditions and scales of melt transfer and interaction in HT migmatites, recording in this instance a transition from melt-dominated open-system behaviour to closed-system crystallization and mineral–melt interaction in the deep crust.

The combination of *in situ* zircon and monazite chemistry and age data obtained for Kulappara in this study also demonstrates that further zircon and monazite chemical modification occurred at 514 Ma, still at minimum zircon Ti temperatures of 780°C. This provides strong evidence from a single locality for a long-lived (at least 30 Myr) metamorphic evolution under granulite-facies conditions in the Trivandrum Block, as suggested by Braun and coworkers (Braun *et al.*, 1998; Braun & Bröcker, 2004; Cenki *et al.*, 2004; Braun, 2006) and supported by Collins *et al.* (2014). The $513 \pm 6$ Ma ages obtained by Collins *et al.* (2007) and other workers for the Southern Granulite Block of India do not define the peak HT metamorphic episode in the Trivandrum Block. The Trivandrum Block peak HT metamorphism occurred at or prior to *c.* 545 Ma, at least at the Kulappara locality studied in detail here.

## ACKNOWLEDGEMENTS

We are grateful to Richard Hinton, John Craven and Nicola Cayzer of the Edinburgh Ion Microprobe Facility (EIMF) for their assistance with ion microprobe analysis and SEM characterization, and to Chris Hayward and David Steele for their assistance and advice on monazite chemical dating on the electron microprobe. Most of the analyses were carried out at the EMMAC by S.L.H. and V.N. during an exchange visit of the latter to the University of Edinburgh. V.N. acknowledges the advice and support of the former Director of CESS, Dr M. Baba, and the present Director of CESS, Dr N. P. Kurian. Ian Buick, Chris Clark and two anonymous reviewers are thanked for their detailed and constructive reviews.

## FUNDING

This work was supported by INSA (Indian National Science Association) research grant 'Fluids, melts and

chemical redistribution during high-grade metamorphism of the continental crust of southern India' to V.N. and a Royal Society of Edinburgh International Exchange Programme Bilateral award to S.L.H. The study was undertaken as part of the PLAN funded project in the Centre for Earth Science Studies, Trivandrum. The visit of V.N. to the University of Edinburgh was funded by the Royal Society of Edinburgh and the Indian National Science Academy.

## SUPPLEMENTARY DATA

Supplementary data for this paper are available at *Journal of Petrology* online.

## REFERENCES

Anders, E. & Grevesse, N. (1989). Abundance of the elements: Meteoritic and solar. *Geochimica et Cosmochimica Acta* **53**, 197–214.

Bartlett, J. M., Dougherty-Page, J. S., Harris, N. B. W., Hawkesworth, C. J. & Santosh, M. (1998). The application of single zircon evaporation and model Nd ages to the interpretation of polymetamorphic terrains: an example from the Proterozoic mobile belt of south India. *Contributions to Mineralogy and Petrology* **131**, 181–195.

Bea, F. (1996). Residence of REE, Y, Th and U in granites and crustal protoliths; Implications for the chemistry of crustal melts. *Journal of Petrology* **37**, 521–552.

Bea, F., Pereira, M. D. & Stroh, A. (1994). Mineral/leucosome trace-element partitioning in a peraluminous migmatite (a laser ablation-ICP-MS study). *Chemical Geology* **117**, 291–312.

Beaumont, C., Jamieson, R. A., Nguyen, M. H. & Lee, B. (2001). Himalayan tectonics explained by extrusion of a low-viscosity channel coupled to focused surface denudation. *Nature* **414**, 738–742.

Beaumont, C., Nguyen, M. H., Jamieson, R. A. & Ellis, S. (2006). Crustal flow modes in large hot orogens. In: Law, R. D., Searle, M. P. & Godin, L. (eds) *Channel Flow, Ductile Extrusion and Exhumation in Continental Collision Zones. Geological Society, London, Special Publications* **268**, 91–145.

Berry, R. F., Steele, D. A. & Meffre, S. (2008). Proterozoic metamorphism in Tasmania: Implications for tectonic reconstructions. *Precambrian Research* **166**, 387–396.

Braun, I. (2006). Pan-African granitic magmatism in the Kerala Khondalite Belt, southern India. *Journal of Asian Earth Sciences* **28**, 38–45.

Braun, I. & Appel, P. (2006). U–Th–total Pb dating of monazite from orthogneisses and their ultra-high temperature metapelitic enclaves: implications for multistage tectonic evolution of the Madurai Block, southern India. *European Journal of Mineralogy* **18**, 415–427.

Braun, I. & Bröcker, M. (2004). Geochronology of granitic gneisses and leucogranites from the Kerala Khondalite Belt, southern India: implications for late Proterozoic crustal evolution in east Gondwana. *International Journal of Earth Sciences* **93**, 13–22.

Braun, I. & Kriegsman, L. M. (2003). Proterozoic crustal evolution of southernmost India and Sri Lanka. In: Yoshida, M., Windley, B. F. & Dasgupta, S. (eds) *Proterozoic East Gondwana: Supercontinent Assembly and Breakup. Geological Society, London, Special Publications* **206**, 169–202.

Braun, I., Montel, J. M. & Nicollet, C. (1998). Electron microprobe dating monazites from high-grade gneisses and pegmatites of the Kerala Khondalite Belt, southern India. *Chemical Geology* **146**, 65–85.

Brown, M. (2004). The mechanism of melt extraction from lower continental crust of orogens. *Transactions of the Royal Society of Edinburgh* **95**, 35–48.

Buick, I. S. C., Clark, C., Rubatto, D., Hermann, J., Pandit, M. & Hand, M. (2010). Constraints on the Proterozoic evolution of the Aravalli–Delhi Orogenic belt (NW India) from monazite geochronology and mineral trace element geochemistry. *Lithos* **120**, 511–528.

Carrington, D. P. & Watt, G. R. (1995). A geochemical and experimental study of the role of K-feldspar during water-undersaturated melting of metapelites. *Chemical Geology* **122**, 59–76.

Cenki, B. & Kriegsman, L. M. (2005). Tectonics of the Neoproterozoic Southern Granulite Terrain, South India. *Precambrian Research* **138**, 37–56.

Cenki, B., Kriegsman, L. M. & Braun, I. (2002). Melt producing and melt consuming reactions in the Achankovil cordierite gneisses, southern India. *Journal of Metamorphic Geology* **20**, 543–561.

Cenki, B., Braun, I. & Bröcker, M. (2004). Evolution of the continental crust in the Pan-African mobile belt of southernmost India: evidence from Nd isotope mapping combined with U–Pb and Rb–Sr geochronology. *Precambrian Research* **134**, 275–292.

Cesare, B., Ferrero, S., Salvioli-Mariani, E., Pedron, D. & Cavallo, A. (2009). 'Nanogranite' and glassy inclusions: the anatectic melt in migmatites and granulites. *Geology* **37**, 627–630.

Choudhary, A. K., Harris, N. B. W., van Calsteren, P. & Hawkesworth, C. J. (1992). Pan-African charnockite formation in Kerala, South India. *Geological Magazine* **129**, 257–264.

Clark, C., Fitzsimons, I. C. W., Healy, D. & Harley, S. L. (2011). How does the continental crust get really hot? *Elements* **7**, 235–240.

Clemens, J. & Vielzeuf, D. (1987). Constraints on melting and magma production in the crust. *Earth and Planetary Science Letters* **86**, 207–306.

Collins, A. S., Santosh, M., Braun, I. & Clark, C. (2007). Age and sedimentary provenance of the Southern Granulites, South India: U–Th–Pb SHRIMP secondary ion mass spectrometry. *Precambrian Research* **155**, 125–138.

Collins, A. S., Clark, C. & Plavsa, D. (2014). Peninsular India in Gondwana: The tectonothermal evolution of the Southern Granulite Terrain and its Gondwanan counterparts. *Gondwana Research* **25**, 190–203.

Corfu, F., Hanchar, J. M., Hoskin, P. W. O. & Kinny, P. (2003). Atlas of zircon textures. In: Hanchar, J. M. & Hoskin, P. W. O. (eds) *Zircons. Mineralogical Society of America and Geochemical Society, Reviews in Mineralogy and Geochemistry* **53**, 469–495.

de Capitani, C. & Petrakakis, K. (2010). The computation of equilibrium assemblage diagrams with Theriak/Domino software. *American Mineralogist* **95**, 1006–1016.

Ferry, J. & Watson, E. B. (2007). New thermodynamic models and revised calibrations for the Ti-in-zircon and Zr-in-rutile thermometers. *Contributions to Mineralogy and Petrology* **154**, 429–437.

Fitzsimons, I. C. W. (1996). Metapelitic migmatites from Brattstrand Bluffs, East Antarctica—metamorphism, melting and exhumation of the mid crust. *Journal of Petrology* **37**, 395–414.

Gasquet, D., Bertrand, J.-M., Paquette, J.-L., Lehmann, J., Ratzov, G., de Ascenção Guedes, R., Tiepolo, M., Boullier, A.-M., Scaillet, S. & Nomade, S. (2010). Miocene to Messinian deformation and hydrothermal activity of the French western Alps: new U–Th–Pb and argon ages from the Lauzière Massif. *Bulletin de la Société Géologique de France* **181**, 227–241.

Ghosh, J. G., de Wit, M. J. & Zartman, R. E. (2004). Age and tectonic evolution of Neoproterozoic ductile shear zones in the Southern Granulite Terrain of India, with implications for Gondwana studies. *Tectonics* **23**, TC3006, http://dx.doi.org/10.1029/2002TC001444.

Giesler, T., Schaltegger, U. & Tomaschek, F. (2007). Re-equilibration of zircon in aqueous fluids and melts. *Elements* **3**, 45–51.

Grimes, C. B., John, B. E., Keleman, P. B., Mazdab, F. K., Wooden, J. L., Cheadle, M. J., Hanghøj, K. & Schwartz, J. J. (2007). Trace element chemistry of zircons from oceanic crust: A method for distinguishing detrital zircon provenance. *Geology* **35**, 643–646.

Hanchar, J. M. & van Westrenen, W. (2007). Rare earth element behavior in zircon–melt systems. *Elements* **3**, 37–42.

Harley, S. L. & Kelly, N. M. (2007). The impact of zircon–garnet REE distribution data on the interpretation of zircon U–Pb ages in complex high-grade terrains: An example from the Rauer Islands, East Antarctica. *Chemical Geology* **241**, 62–87.

Harley, S. L., Kelly, N. M. & Möller, A. (2007). Zircon and the thermal histories of hot mountain belts. *Elements* **3**, 25–30.

Harris, N. B. W., Santosh, M. & Taylor, P. N. (1994). Crustal evolution in South India: constraints from Nd isotopes. *Journal of Geology* **102**, 139–150.

Hinton, R. W. & Upton, B. G. J. (1991). The chemistry of zircon: variations within and between large crystals from syenite and alkali basalt xenoliths. *Geochimica et Cosmochimica Acta* **55**, 3287–3302.

Holland, T. J. B. & Powell, R. (1998). An internally consistent thermodynamic dataset for phases of petrological interest. *Journal of Metamorphic Geology* **16**, 309–343.

Holland, T. J. B. & Powell, R. (2003). Activity–composition relations for phases in petrological calculations: an asymmetric multicomponent formulation. *Contributions to Mineralogy and Petrology* **145**, 492–501.

James, R. S. & Hamilton, D. L. (1969). Phase relationships in the system $NaAlSi_3O_8$–$KAlSi_3O_8$–$CaAl_2Si_2O_8$–$SiO_2$ at 1 kilobar water vapour pressure. *Contributions to Mineralogy and Petrology* **21**, 111–141.

Jamieson, R. A. & Beaumont, C. (2011). Coeval thrusting and extension during lower crustal ductile flow—implications for exhumation of high-grade metamorphic rocks. *Journal of Metamorphic Geology* **29**, 33–51.

Jamieson, R. A., Beaumont, C., Medvedev, S. & Nguyen, M. H. (2004). Crustal channel flows: 2. Numerical models with implications for metamorphism in the Himalayan–Tibetan orogen. *Journal of Geophysical Research* **109**, B06407, doi:10.1029/2003JB002811.

Jamieson, R. A., Beaumont, C., Warren, C. J. & Nguyen, M. H. (2010). The Grenville Orogen explained? Applications and limitations of integrating numerical models with geological and geophysical data. *Canadian Journal of Earth Sciences* **47**, 517–539.

Johannes, W. & Holtz, F. (1996). *Petrogenesis and Experimental Petrology of Granitic Rocks*. Springer.

Kelly, N. M. & Harley, S. L. (2005). An integrated microtextural and chemical approach to zircon geochronology: refining the Archaean history of the Napier Complex, east Antarctica. *Contributions to Mineralogy and Petrology* **149**, 57–84.

Kelly, N. M., Hinton, R. W., Harley, S. L. & Appleby, S. (2008). New SIMS U–Pb zircon ages from the Langavat Belt, South Harris, NW Scotland: implications for the Lewisian terrane model. *Journal of the Geological Society, London* **165**, 967–981.

Kelsey, D. E. & Powell, R. (2011). Progress in linking accessory mineral growth and breakdown to major mineral evolution in metamorphic rocks: a thermodynamic approach in the $Na_2O$–$CaO$–$K_2O$–$FeO$–$MgO$–$Al_2O_3$–$SiO_2$–$H_2O$–$TiO_2$–$ZrO_2$ system. *Journal of Metamorphic Geology* **29**, 151–166.

Kelsey, D. E., Powell, R., Wilson, C. J. L. & Steele, D. A. (2003). (Th + U)–Pb monazite ages from Al–Mg-rich metapelites, Rauer Group, east Antarctica. *Contributions to Mineralogy and Petrology* **146**, 326–340.

Kelsey, D. E., Clark, C. F. P. & Hand, M. P. (2008). Thermobarometric modelling of zircon and monazite growth in melt-bearing systems: examples using model metapelitic and metapsammitic granulites. *Journal of Metamorphic Geology* **26**, 199–212.

Kriegsman, L. M. (2001). Partial melting, partial melt extraction and partial back reaction in anatectic migmatites. *Lithos* **56**, 75–96.

Kröner, A., Santosh, M. & Wong, J. (2012). Zircon ages and Hf isotopic systematics reveal vestiges of Mesoproterozoic to Archaean crust within the late Neoproterozoic–Cambrian high-grade terrain of southernmost India. *Gondwana Research* **21**, 876–886.

Ludwig, K. R. (2003). *User's Manual for Isoplot 3.00—A Geochronological Toolkit for Microsoft Excel. Berkeley Geochronology Centre Special Publications* **4**.

Morimoto, T., Santosh, M., Tsunogae, T. & Yoshimura, Y. (2004). Spinel + quartz association from the Kerala Khondalites, southern India: evidence for ultrahigh-temperature metamorphism. *Journal of Mineralogical and Petrological Sciences* **99**, 257–278.

Nandakumar, V. & Harley, S. L. (2000). A reappraisal of the pressure–temperature path of granulites from the Kerala Khondalite Belt, southern India. *Journal of Geology* **108**, 687–703.

Patiño-Douce, A. E. & Beard, J. S. (1995). Dehydration-melting of biotite gneiss and quartz amphibolite from 3 to 15 kbar. *Journal of Petrology* **36**, 707–738.

Plasva, D., Collins, A. S., Foden, J. F., Kropinski, L., Santosh, M., Chetty, T. R. K. & Clark, C. (2012). Delineating crustal domains in Peninsular India: age and chemistry of orthopyroxene-bearing felsic gneisses in the Madurai Block. *Precambrian Research* **198–199**, 77–93.

Putnis, A. (2002). Mineral replacement reactions: from macroscopic observations to microscopic mechanisms. *Mineralogical Magazine* **66**, 689–708.

Rajesh, H. M., Santosh, M. & Yoshikura, S. (2011). The Nagercoil Charnockite: a magnesian, calcic to calc-alkaline granitoid dehydrated during a granulite-facies metamorphic event. *Journal of Petrology* **52**, 375–400.

Rubatto, D. & Hermann, J. (2007). Experimental zircon/melt and zircon/garnet trace element partitioning and implications for the geochronology of crustal rocks. *Chemical Geology* **241**, 38–61.

Rubatto, D., Hermann, J. & Buick, I. S. (2006). Temperature and bulk composition control on the growth of monazite and zircon during low-pressure anatexis (Mount Stafford, Central Australia). *Journal of Petrology* **47**, 1973–1996.

Sano, Y., Terada, K. & Fukuoka, T. (2002). High mass resolution ion microprobe analysis of rare earth elements in silicate glass, apatite and zircon: lack of matrix dependency. *Chemical Geology* **184**, 217–230.

Santosh, M. (1996). The Trivandrum and Nagercoil Granulite Blocks. *Gondwana Research Group Memoir* **3**, 243–277.

Santosh, M., Yokoyama, K., Biju-Sekhar, S. & Rogers, J. J. W. (2003). Multiple tectonothermal events in the granulite blocks of southern India revealed from EPMA dating: implications on the history of supercontinents. *Gondwana Research* **6**, 29–63.

Santosh, M., Collins, A. S., Morimoto, T. & Yokoyama, K. (2005*a*). Depositional constraints and age of metamorphism in southern India: U–Pb chemical (EMPA) and isotopic (SIMS) ages from the Trivandrum Block. *Geological Magazine* **142**, 255–268.

Santosh, M., Tanaka, K., Yokoyama, K. & Collins, A. S. (2005*b*). Late Neoproterozoic–Cambrian felsic magmatism along transcurrent shear zones in Southern India: U–Pb electron microprobe ages and implications for the amalgamation of the Gondwana supercontinent. *Gondwana Research* **8**, 31–42.

Santosh, M., Morimoto, T. & Tsutsumi, Y. (2006*a*). Geochronology of the khondalite belt of the Trivandrum Block, Southern India: electron probe ages and implications for Gondwana tectonics. *Gondwana Research* **9**, 261–278.

Santosh, M., Tagawa, M., Yokoyama, K. & Collins, A. S. (2006*b*). U–Pb electron probe geochronology of the Nagercoil granulites, Southern India: Implications for Gondwana amalgamation. *Journal of Asian Earth Sciences* **28**, 63–80.

Santosh, M., Maruyama, S. & Sato, K. (2009). Anatomy of a Cambrian suture in Gondwana: implications for the timing of Gondwana assembly. *Gondwana Research* **16**, 321–341.

Sato, K., Santosh, M., Tsunogae, T., Chetty, T. R. K. & Hirata, T. (2011). Subduction–accretion–collision history along the Gondwana suture in southern India: a laser ablation ICP-MS study of zircon chronology. *Journal of Asian Earth Sciences* **40**, 162–171.

Sawyer, E. W. (1994). Melt segregation in the continental crust. *Geology* **22**, 1019–1022.

Sawyer, E. W. (1999). Criteria for the recognition of partial melt. *Physics and Chemistry of the Earth* **24**, 269–279.

Sawyer, E. W. (2001). Melt segregation in the continental crust: Distribution and movement of melt in anatectic rocks. *Journal of Metamorphic Geology* **18**, 291–309.

Schärer, U. (1984). The effect of initial $^{230}$Th disequilibrium on young U–Pb ages: the Makalu case, Himalaya. *Earth and Planetary Science Letters* **67**, 191–204.

Schuhmacher, M., de Chambost, E., McKeegan, K. D., Harrison, T. M. & Midgeon, H. (1994). *In-situ* dating of zircon with the CAMECA ims-1270. In: Benninghoven, A., Nihei, Y., Shimizu, R. & Werner, H. W. (eds) *Secondary Ion Mass Spectrometry, SIMS IX*. John Wiley, pp. 919–922.

Shabeer, K. P., Satish-Kumar, M., Armstrong, R. & Buick, I. S. (2005). Constraints on the timing of Pan-African granulite-facies metamorphism in the Kerala Khondalite Belt of Southern India: SHRIMP mineral ages and Nd isotope systematics. *Journal of Geology* **113**, 95–106.

Sláma, J., Košler, J., Condon, D., Crowley, J. L., Gerdes, A., Hanchar, J. M., Horstwood, M. S. A., Morris, G. A., Nasdala, L., Norberg, N., Schaltegger, U., Schoene, B., Tubrett, M. N. & Whitehouse, M. J. (2008). Plešovice zircon—a new natural reference material for U–Pb and Hf isotopic microanalysis. *Chemical Geology* **249**, 1–35.

Stevens, G. & Clemens, J. D. (1993). Fluid-absent melting and the roles of fluids in the lithosphere: a slanted summary? *Chemical Geology* **108**, 1–17.

Tadokoro, H., Tsunogae, T. & Santosh, M. (2008). Metamorphic *P–T* path of the eastern Trivandrum Granulite Block, southern India: implications for regional correlation of lower crustal fragments. *Journal of Mineralogical and Petrological Sciences* **103**, 279–284.

Taylor, J. & Stevens, G. (2010). Selective entrainment of peritectic garnet in S-type granitic magmas: evidence from Archaean mid-crustal anatectites. *Lithos* **120**, 277–292.

Taylor, R. J. M. (2009). Distribution of trace elements between zircon, garnet and melt: a key to understanding crustal events and processes. PhD thesis, University of Edinburgh, 220 pp.

Teale, W., Collins, A. S., Foden, J. F., Payne, J. L., Plasva, D., Chetty, T. R. K., Santosh, M. & Fanning, M. (2011). Cryogenian (830 Ma) mafic magmatism and metamorphism in the northern Madurai Block, southern India: a magmatic link between Sri Lanka and Madagascar? *Journal of Asian Earth Sciences* **42**, 223–233.

Thompson, A. B. (1982). Dehydration melting of pelitic rocks and the generation of $H_2O$-undersaturated granitic liquids. *American Journal of Science* **282**, 1567–1595.

Tomson, J. K., Bhaskar Rao, Y. J., Vijaya Kumar, T. & Mallikharjuna Rao, J. (2006). Charnockite genesis across the Archaean–Proterozoic terrane boundary in the South Indian Granulite Terrain: constraints from major–trace element geochemistry and Sr–Nd isoropic systematics. *Gondwana Research* **10**, 115–127.

Tomson, J. K., Bhaskar Rao, Y. J., Vijaya Kumar, T. & Choudhary, A. K. (2013). Geochemistry and neodymium model ages of Precambrian charnockites, Southern Granulite Terrain, India: constraints on terrain assembly. *Precambrian Research* **227**, 295–315.

Vanderhaeghe, O. (2009). Migmatites, granites and orogeny: Flow modes of partially-molten rocks and magmas associated with melt/solid segregation in orogenic belts. *Tectonophysics* **477**, 119–134.

van Westrenen, W., Wood, B.J. & Blundy, J.D. (2001). A predictive thermodynamic model of garnet–melt trace element partitioning. *Contributions to Mineralogy and Petrology* **142(2)**, 219–234.

Waters, D. J. (1988). Partial melting and the formation of granulite facies assemblages in Namaqualand, South Africa. *Journal of Metamorphic Geology* **6**, 387–404.

Watson, E. B. & Harrison, T. M. (1983). Zircon saturation revisited; temperature and composition effects in a variety of crustal magma types. *Earth and Planetary Science Letters* **64**, 295–304.

Watson, E. B., Wark, D. A. & Thomas, J. B. (2006). Crystallization thermometers for zircon and rutile. *Contributions to Mineralogy and Petrology* **151**, 413–433.

Watt, G. R. & Harley, S. L. (1993). Accessory phase controls on the geochemistry of crustal melts and restites produced during water-undersaturated partial melting. *Contributions to Mineralogy and Petrology* **114**, 550–566.

White, R. W. & Powell, R. (2002). Melt loss and the preservation of granulite facies mineral assemblages. *Journal of Metamorphic Geology* **20**, 621–632.

White, R. W., Powell, R., Holland, T. J. B. & Worley, B. A. (2000). The effect of $TiO_2$ and $Fe_2O_3$ on metapelitic assemblages at greenschist and amphibolite facies conditions: mineral equilibria calculations in the system $K_2O$–FeO–MgO–$Al_2O_3$–$SiO_2$–$H_2O$–$TiO_2$–$Fe_2O_3$. *Journal of Metamorphic Geology* **18**, 497–511.

White, R. W., Powell, R. & Holland, T. J. B. (2001). Calculation of partial melting equilibria in the system $Na_2O$–CaO–$K_2O$–FeO–MgO–$Al_2O_3$–$SiO_2$–$H_2O$ (NCKFMASH). *Journal of Metamorphic Geology* **19**, 139–153.

White, R. W., Powell, R. & Clarke, G. L. (2002). The interpretation of reaction textures in Fe-rich metapelitic granulites of the Musgrave Block, central Australia: constraints from mineral equilibria calculations in the system $K_2O$–FeO–MgO–$Al_2O_3$–$SiO_2$–$H_2O$–$TiO_2$–$Fe_2O_3$. *Journal of Metamorphic Geology* **20**, 41–55.

White, R. W., Powell, R. & Holland, T. J. B. (2007). Progress relating to calculation of partial melting equilibria for metapelites. *Journal of Metamorphic Geology* **25**, 511–527.

Whitehouse, M. J. & Platt, J. P. (2003). Dating high-grade metamorphism—constraints from rare-earth elements in zircon and garnet. *Contributions to Mineralogy and Petrology* **145**, 61–74.

Whitehouse, M. J., Claesson, S., Sunde, T. & Vestin, J. (1997). Ion microprobe U–Pb geochronology and correlation of Archaean gneisses from the Lewisian Complex of Gruinard Bay, northwestern Scotland. *Geochimica et Cosmochimica Acta* **61**, 4429–4438.

Wiedenbeck, M., Hanchar, J. M., Peck, W. H., Sylvester, P., Valley, J., Whitehouse, M. J., Kronz, A., Morishita, Y. & Nasdala, L. (2004). Further characterization of the 91500 zircon crystal. *Geostandards and Geoanalytical Research* **28**, 9–39.

Winkler, H. G. F. & von Platen, H. (1961). Experimentelle gesteinsmetamorphose. 5. Experimentelle anatektische schmelzen und ihre petrogenetische bedeutung. *Geochimica et Cosmochimica Acta* **24**, 250–259.